UNIVERSITY OF MISKOLC

MIKOVINY SAMUEL DOCTORAL SCHOOL OF EARTH SCIENCES

Head of the doctoral school: Prof. Dr. Péter Szűcs

Applicability of CT (computed tomography) for pore network extraction and characterization

Thesis of the doctoral dissertation (PhD)

Author:

HASAN AL ATRASH

Scientific supervisor:

FELICITÁSZ VELLEDITS

UNIVERSITY of MISKOLC

FACULTY OF EARTH AND ENVIRONMENTAL SCIENCES AND ENGINEERING

INSTITUTE of EXPLORATION GEOSCIENCES

2023 Miskolc, Hungary

Recommendation of the supervisor

Carbonate reservoir rocks have a complicated pore system as a result of sedimentological and diagenetic processes. Contrary to siliciclastic reservoirs, where the main component is the chemically resistant quartz, carbonate minerals (aragonite, high-Mg calcite) are very susceptible to extensive diagenetic change, dissolution, cementation, recrystallization and replacement at environmental conditions in a variety of diagenetic environments or during a succession of diagenetic episodes.

Dissolution of carbonate minerals plays a determining role in the development of the pore system. This results a lack of interrelationships between porosity and permeability, making it difficult to characterize fluid flow through carbonates.

To understand the hydrocarbon reservoirs, it is crucial to investigate not only the 3D pore network, but also the sedimentological and diagenetic processes that have shaped them. Depicting the pore network in 3D on a micron scale not provide a complete understanding of the geological processes involved in formation of hydrocarbon reservoirs.

In the recent past many articles described several methods of enabling the depiction of pore network in micron scale using micro-XCT measurement for instance. By contrast only a few publications explain the origin of the various pore types while also depicting the pore network.

Therefore, in his study the candidate employed a combination of micro-CT analyses, lab measurements of helium porosity and nitrogen permeability and microfacies analyses. Only the combination of the above-mentioned methods can explain why one part of the reservoir became productive and the other dry.

To achieve accurate X-ray image segmentation, he investigated and compared several segmentation techniques, including entropy and clustering. Then employed the Naïve Bayes classifier and 10-fold cross-validation to assess the accuracy of our results. His study achieved high accuracy with the type-2 fuzzy entropy technique on various metrics, including precision and recall. The comparison between the measured helium porosity and image-derived porosity showed a close match.

The candidate has summarised his research in 11 theses. The structure of the PhD thesis is clear and easy to follow. His statements are made even clearer by means of diagrams, figures, and tables. His research results are well applicable in hydrocarbon research.

His active participation during the PhD training, both in research and in education, his creative work and his results demonstrate the high level of knowledge and his ability to work and think independently.

Based on the above, it can be concluded that the PhD thesis contains new scientific results based on credible data. The thesis meets the requirements of the Mikoviny Samuel Doctoral School of Earth Sciences in all respects. I recommend the submitted thesis for public discussion and the candidate be awarded the degree of Doctor of Science (PhD).

Miskolc, 02.11.2023

Dr. habil Felicitász Velledits PhD, DSc

scientific supervisor

Contents

1. List of symbols

Symbol	Description	unit
µ-CT	A unit of measurement commonly used in micro-CT to express spatial resolution or voxel size	Meter
R	The achievable resolution in the object of a CT-system	
S	The spot size of the X-ray source	p.p.s. mm^{-2}
d	The resolution of the detector	Kev
M	The magnification of a CT system	-
$\mathbf{d_c}$	The x-ray source and object distance	m
$\mathbf{d_d}$	The object-detector distance of a CT-system	m
x	The lenses radius	m
I	The intensity of light or radiation after it has passed through a material	R (roentgen)
$\mathbf{I_0}$	The initial or incident intensity of light or radiation before it interacts with the material.	R (roentgen)
e	The base of natural algorithm	-
µ	The linear attenuation coefficient of the material	HU
x	The length of the X-ray path through the material	m
S	The entropy of the system	Joule/Kelvin
Pj	Is the probability that the system is at state *j*	-

K	Is the Boltzmann constant	-
W	The number of states in the system	-
A	A type-1 fuzzy set A in a finite set x	-
$\boldsymbol{\mu_A(x)}$	The membership function	-
$\boldsymbol{\mu_A^{High}}$	Upper membership function	-
$\boldsymbol{\mu_A^{Low}}$	Lower membership function	-
$\mathbf{h_i}$	Image histogram and i level of intensity	-
NP	Total number of pixels contained in the image	-
$\mathbf{P_k}$	The ultra-fuzziness of level of intensity	-
$\mathbf{Fe_k}$	Type 2 fuzzy entropy of k^{th} threshold	-
$\mathbf{T_{fe}}$	Total entropy	-
$\mathbf{P(c_k|x)}$	posterior probability of an event x belongs to a class k	-
$\mathbf{P\ (c_k)}$	The Probability of c_k occurring	-
P(x)	The probability of x occurring	-
x	is a n-dimensional vector	-

List of tables

List of figures

2. Acknowledgment

I would like to express my heartfelt gratitude to several individuals and organizations who have played a significant role in my educational journey.

First and foremost, I would like to extend my sincerest thanks to Stipendium Hungarikum and the Hungarian Public Foundation for their invaluable support in funding my studies. This opportunity has truly been life-changing, and I am immensely grateful for the doors it has opened for me.

I owe a great debt of gratitude to my scientific supervisor, Dr. Felicitász Velledits. Throughout my years of study, Dr. Velledits has been a constant source of support and guidance. I not only consider them a mentor but also a part of my scientific family, and I am deeply appreciative of their unwavering assistance.

I would also like to express my gratitude to Dr. Janos Geiger for his continuous support and guidance. His generosity, kind words, and assistance have been instrumental in my academic journey, and I am thankful for his mentorship.

To the head of our department, Dr. Mádai Ferenc, I extend my heartfelt thanks for his continuous support and affection. His role in my academic life has been akin to that of a family member, and he has been a true inspiration to me.

I would also like to acknowledge the University of Miskolc and all its teaching staff for their dedication and commitment to providing me with a quality education. The gratitude extends to the 3DLab at the university of Miskolc specially Dr. Mertinger Valéria and Filep Ádám for providing the micro-CT scans and Ferenc Móricz at the Mineralogy Department for helping in samples preparation.

My thanks extend to my family for their unwavering support and patience throughout my academic endeavors. Their encouragement has been a cornerstone of my success. Last but not least, I want to express my appreciation to my uncles for their assistance and support during this journey. Their contributions have been a vital part of my educational achievements.

To all of you, I am deeply grateful for the role you have played in my academic and personal growth. Your support and encouragement have made a world of difference, and I look forward

to making the most of this education to contribute positively to our society and the world at large. Thank you from the bottom of my heart.

3. Summary

The accurate characterization of pore structures in carbonate rocks is crucial for understanding their petrophysical characteristics. These rocks possess intricate pore systems with varying interconnectivity, which significantly influence their properties. To accurately calculate these attributes, pore network models rely on capturing the complex geometry and topology of the pore network. High-resolution X-ray computed tomography (CT) has emerged as a valuable technology for geological investigations due to its non-destructive nature and ability to generate detailed images that closely resemble serial sections of the object.

In this context, image segmentation plays a vital role in interpreting and evaluating X-ray tomographic images. Successful pore network modeling depends on effectively representing the real pore space in terms of its geometric and topological characteristics. In CT scans, image segmentation separates the pore phase from the solid phase, enabling the extraction of important properties such as pore size distribution (PSD), connectivity, and tortuosity. Therefore, accurate image segmentation serves as the initial step in pore network modeling and analysis.

Various techniques for image segmentation have been reported in the literature. However, there is no universal algorithm that consistently produces accurate results for all types of data. In my Ph.D thesis, my objective is to conduct a comprehensive research study that encompasses three key components: image segmentation, a comparative microfacies analysis between productive and dry intervals, and petrophysical characterization. These elements are equally important in achieving reliable results and contributing to the field of reservoir characterization and evaluation. To accomplish this; firstly, I focus on evaluating the performance of different machine learning (ML) techniques, including clustering and entropy techniques, for image classification. Through the development of a workflow for unsupervised machine learning (ML), incorporating methods such as naive Bayes and cross-validation, I aim to create a pixel classification scheme that effectively distinguishes between different elements within the image. This scheme will lead to more accurate segmentation and enable the identification and analysis of pore properties within the 3D pore network.

Secondly, I integrate microfacies analysis of thin sections obtained from the same core samples into my research. By combining these findings with the results obtained from image segmentation and pore property analysis, I can evaluate reservoir rock samples from both dry and productive intervals. This comparative analysis allows for a comprehensive understanding of the variations in pore properties and their potential implications for reservoir performance.

Lastly, petrophysical characterization is a fundamental aspect of the research. By quantifying and analyzing various petrophysical properties, such as pore size distribution, connectivity, and tortuosity. My aim was to gain a comprehensive understanding of the reservoir rocks. These petrophysical characteristics directly impact the behavior and performance of the reservoir, making their accurate characterization crucial for effective decision-making.

In summary, my Ph.D. thesis revolves around three interconnected components: accurate image segmentation, a comparative microfacies analysis between productive and dry intervals, and petrophysical characterization. By enhancing image segmentation, conducting a thorough comparative analysis, and quantifying petrophysical properties, I aim to contribute to the field of reservoir characterization and evaluation. The comprehensive insights gained from this research will aid in making decisions within the oil and gas industry

4. Introduction

Carbonate reservoir rocks have a complicated pore system as a result of sedimentological and diagenetic processes (Scoffin 1987; Arns et al. 2004; Flügel 2004).

Contrary to siliciclastic reservoirs, where the main component is the chemically resistant quartz, carbonate minerals (calcite and aragonite) are very susceptible to extensive diagenetic change. Carbonate minerals are susceptible to rapid dissolution, cementation, recrystallization and replacement at ambient conditions in a variety of diagenetic environments or during a succession of diagenetic episodes.

Dissolution of carbonate minerals plays a determining role in the development of the pore system. This intricacy frequently results in a lack of interrelationships between porosity and permeability, making it difficult to characterize fluid flow through carbonates (Arns et al. 2004).

In the cases of XCT analyses, the very first step should be understanding the diagenetic history. Only that knowledge can make sure, that the selected small volumes can be representative of all the processes affecting the pore system. Also, such information can determine what petrophysical characters we can expect. E.g., in the case of bio-mold porosity, we can expect quite a high total, but low or moderate effective porosity, low pore connectivity, and consequently low permeability. We can also expect that the large-scale poro-perm correlation will be very low (if any).

In recent years, the use of micro X-ray computer tomography (micro-XCT) imaging to assess the pore space of reservoir rocks has grown in popularity. This technique generates 3D pore network at micron scale (Brunke et al. 2010), which can provide valuable information on the complex pore system of rock samples and their interrelationships between porosity and permeability. Prior to the availability of micro-XCT, 3D pore characterization could only be accomplished using statistical models to reconstruct 3D porous media from 2D thin section images (Hazlett 1995) or process-based models (Øren and Bakke 2002). Both statistical and process-based models have merits, but with the recent advancements in X-ray technology, complicated pore-networks in 3D down to sub-micron scale may now be seen (Brunke et al. 2007). 3D pore-network representation can improve the understanding of the evolution of porosity and permeability of a rock sample (Youssef et al. 2007a, b).

Al-Kharusi et al. (2007) showed the efficacy of micro XCT imaging for characterizing the pore space in sandstone and carbonate rocks. The authors demonstrated that this technique enables them to visualize the complicated pore network as well as identify different pore types and their interconnectedness. This data can be utilized to gain a better understanding of the processes that affect fluid flow in reservoir rocks. Chauhan et al. (2016) is another study further emphasized the relevance of using 3D pore-network representations generated by micro XCT imaging to improve the understanding of porosity and permeability evolution in rock samples. The authors used this technique to investigate the pore-scale mechanisms that control fluid flow in carbonate rocks and showed that the pore network geometry plays a critical role in determining the permeability of these rocks.

In general, laboratory experiments or well logs can be used to assess the porosity of reservoir rocks. These measurements can provide data on the overall pore space. Unfortunately, we cannot go any farther in characterizing the pore organization, such as connectivity and coordination number, in these circumstances. Another limitation of these measures is that they cannot provide a three-dimensional dispersion of the pore network. Current improvements in X-ray microcomputed tomography enable a solution to this problem by quantifying pore network geometry from high-resolution 3D images (Al-Ansi et al. 2013, Andr an et al. 2013). The use of X-ray CT and image analysis has improved 3D material characterisation, particularly for pore network geometry studies.

To a large extent the success of pore network models (PNM) depends on the way they represent the real pore space in terms of its geometrical and topological characteristics for a given application (Xiong et al. 2016). In CT scans, the pore space is segmented from the solid phase, yielding important geometrical properties such as pore size distribution (PSD), connectivity, and tortuosity. Therefore, accurate image segmentation (separating the pore phase from the solid one) is the first step toward pore network modelling and analysis (Gonzalez and Woods 2008). The literature reports a variety of techniques for image segmentation, nevertheless, no universal segmentation algorithm can produce consistent results for every type of data (Wildenschild and Sheppard 2013). Leu et.al (2014) stated in their sensitivity study that segmentation stage will determine the success or failure of the final results, where they demonstrate that small bias in the accuracy of the binarization may cause a significant error in the calculated permeability.

However, the PNM has the highest geological uncertainty in the modeling process. It is because the analyzer does not have any base to decide whether the applied cutoff/threshold value fits the pores/voids of the studied volume. In fact, the thin sections can help in that decision. But, the 2D discrete reality they can show cannot be used to derive either the 3D distribution or the 3D geometry. So all-in-all, PNM is a model, which must be validated from both geological and mathematical points of view. The mathematical validation is quite a smooth process. To perform a geological validation one can use only the comparison of the result of the geological interpretation of the PNM and the preliminary expectations. If they fit, the result is fine. If they do not fit, the whole modeling process should be reorganized.

Image segmentation is a critical step in the analysis of micro-CT images of porous materials. However, due to the inherent heterogeneity in the features of the materials as well as the imaging parameters used to obtain the data, no universal segmentation method can generate consistent results for every type of data. As a result, the development of advanced learning algorithms for image segmentation is crucial for improving process's accuracy and efficiency. The research objective of this study is to comprehensively investigate the optimal advanced learning strategies for analyzing pore space and measuring porosity in carbonate rock samples using high-resolution X-ray micro-CT images. To achieve this objective, the study incorporates several key components: image segmentation, a comparative analysis of sedimentological and diagenetic history between productive and dry intervals, and microfacies analysis to compare the structure of productive and dry intervals.

The research objective of this study is to investigate and compare the pore network characteristics and petrophysical properties in two distinct intervals: a dry interval and a productive interval. The study aims to comprehensively analyze and understand the differences in pore network geometry, connectivity, and petrophysical properties between these two intervals.

To achieve my goal I have implemented several steps:

-Firstly I evaluated and compared different machine learning (ML) techniques, including clustering and entropy techniques, to achieve accurate image segmentation. By developing a workflow that integrates unsupervised machine learning methods such as naive Bayes and cross-validation, the study seeks to create a robust pixel classification scheme that effectively

identifies and distinguishes various elements within the images. This will enable accurate segmentation and facilitate the analysis of pore properties within the three-dimensional pore network.

-Secondly I conducted a comparative analysis of sedimentological and diagenetic history between the productive and dry intervals. By examining the sedimentological characteristics and diagenetic processes that have influenced the formation of the intervals, the study aims to understand the factors contributing to their contrasting productivity. This analysis will provide valuable insights into the relationship between geological features and reservoir performance.

-Thirdly, microfacies analysis is integrated into the research to compare the structure of the productive and dry intervals. By examining thin sections obtained from the same core samples, the study aims to identify and characterize the microfacies present in each interval. This analysis will provide valuable information on the differences in pore network geometry and micro-scale features between the productive and dry intervals. With the help of microfacies analysis it is possible to reconstruct the sedimentological and diagenetic evolution of the productive and dry samples. It allows us to answer the question why is one part of the limestone is productive and the other is dry.

By combining image segmentation, comparative sedimentological and diagenetic analysis, and microfacies analysis, the study seeks to address the research gap and gain a comprehensive understanding of the relationship between pore network geometry, sedimentological characteristics, and reservoir productivity. The findings of this study will contribute to the advancement of reservoir characterization and evaluation techniques, enabling more effective optimization of oil recovery strategies.

Moreover, this is the first study to use high-resolution X-ray micro-CT scans to not only compare the pore network geometry of carbonate rock samples from these two intervals, but also delve into the diagenetic and sedimentological process that shaped them. This research gap is relevant because it has the potential to provide insights into the relationship between the pore network geometry and the productivity of the oil well, which can have important implications for the petroleum industry and could be useful for optimizing oil recovery strategies.

It is noteworthy, that most of the XCT instruments have a fixed focal point, the smaller the sample size/volume the smaller the pore diameter which can be revealed. One cannot view and analyze anything below the resolution. Consequently, only the flow properties determined by pores with pore diameters being not smaller than the resolution can be studied. Sometimes it is enough to derive general flow characters. One must keep in mind that even the 0.5-micron resolution is not enough to study the physisorption processes. The upper limit of the possible pore diameters is determined by the size of the measured volume. This fact excludes the analyses of fractured porosity. The result of the above derivations is that a PNM is useful, though its ability to show flow characteristics is strongly limited by the resolution of the scanning process. It is not a problem but must be emphasized correctly.

5. Literature review

5.1 Pore space imaging

5.1.1 Serial sectioning

Several methods have been proposed to visualize 3D microstructure. Serial sectioning method for 3D imaging can be achieved, when consecutive thin sections of the materials are removed one at a time and exposed surfaces are imaged at a high-resolution. Then, the 3D visualization can be obtained by stacking 2D serial sections (Lymberopoulos and Payatakes 1992). However, this method is considered to be time consuming due to the fact of a long laborious process. Moreover, laborious operation is restricted because preparing cross sections with a spacing of less than around 10 µm is impossible (Dullien 1992). Another drawback is the limitation of the number of the slices that can be obtained in one hour, which ranges in-between 5-20 slices reported by Spowart (2003), which makes unsuitable for imaging representative rock volume with heteroginity. Additionally serial sections analysis does not account for throats of small size making the prediction of the flow properties questionable (Koplik et al. 1984). The work flow of conventional serial sectioning is illustrated in Figure1.

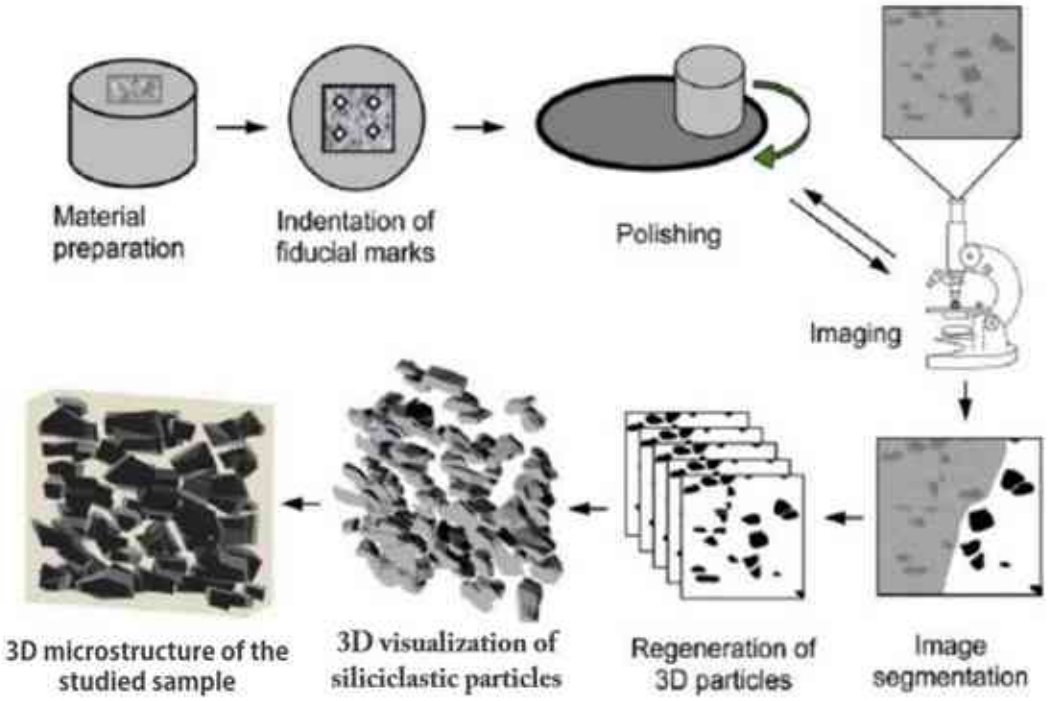

Figure 1 *Flow chart of serial sectioning to obtain 3D images of porous media (Chawla et al., 2006).*

Recently, a new method has emerged which combines serial sectioning and focused ion beam (FIB) technology (Tomutsa and Radmilovic 2003, Tomutsa and Silin 2004). This method allows the imaging of higher resolution at a sub-micron resolution of the microstructure of the geological materials such as shown in Figure 2

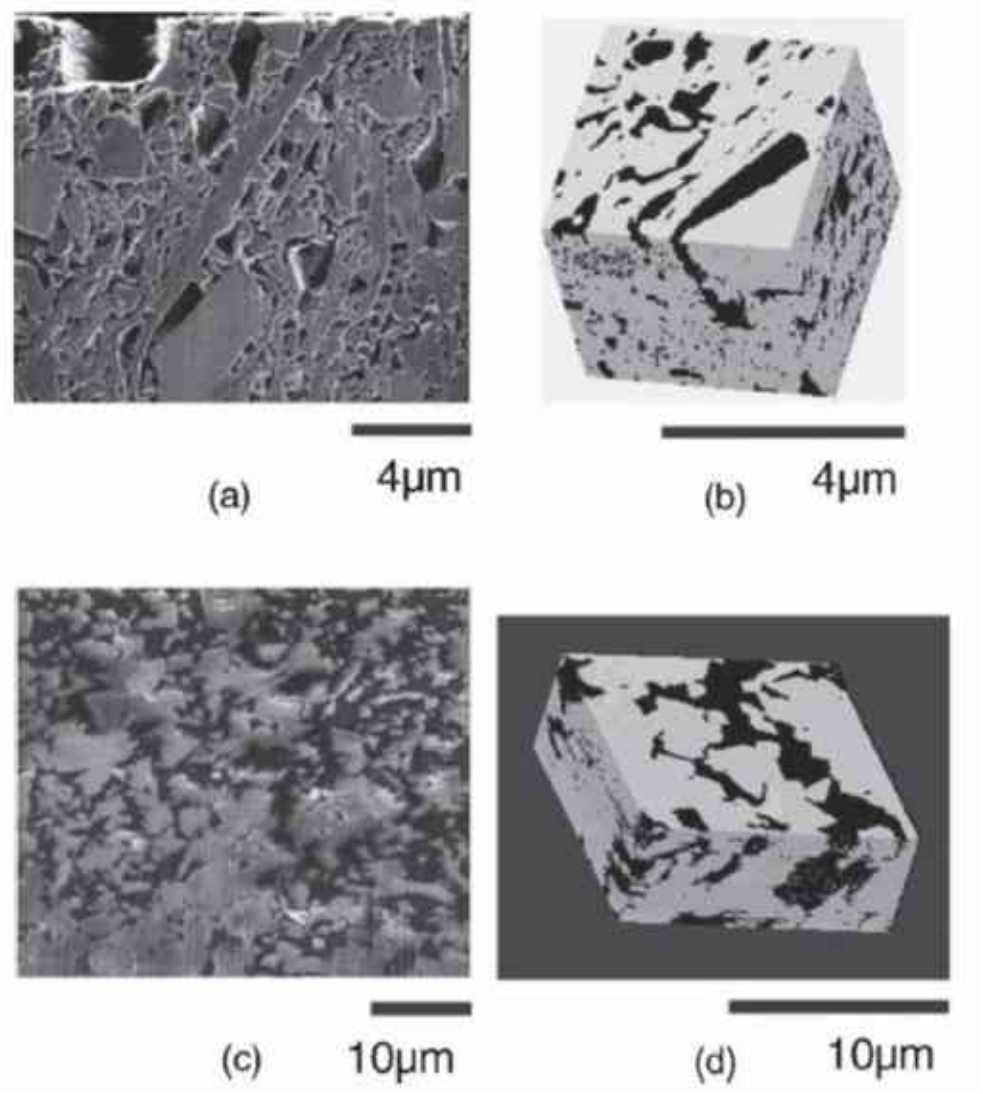

Figure 2 *Images in 2D: a) FIB image of dolomite c) image of dolomite where ;(b,d) are their 3D reconstruction images based on FIB serial sectioning. The reconstructions are from successive binarized FIB images spaced at 0.1 μm. The pore space is black (Tomutsa et al. 2007).*

The FIB was used to mill layers as thin as 100 nanometers and as wide as 50 micrometers by sputtering atoms off the sample surface. FIB uses a focused beam of gallium ions (Ga+) accelerated to an energy of 5-50 keV and then focused onto the sample by electrostatic lenses, creating images with a spot size down to nanometer. Despite the fact that this technology has a great deal of potential for imaging hydrocarbon-bearing rocks at high resolution and creates images of greater quality than electron beam imaging, it is still significantly time consuming due to the refocusing between milling and imaging as well as the sample repositioning (Tomutsa et al. 2007)

5.1.2 Stochastic reconstruction using statistical methods 2D

Contrary to 3D images, 2D thin sections are often available at high resolution, which make it suitable for studying geometrical properties such as micro porosity. Two point correlation function and porosity can be measured using thin sections and used to generate a 3D image with the same statistical properties.

3D images can be reconstructed using statistical methods with information obtained by analyzing 2D thin sections. Finding appropriate morphological descriptors that replicate the microstructure of porous materials is essential. Allowing a wide variety of porous media to be described. The geometrical properties of the original pore space are often used with a truncated Gaussian random field to reconstruct 3D images (Quiblier 1984). These geometrical properties such as porosity, one point correlation function and two points correlation function (measuring the probability of finding two points separated by a certain distance within the same phases) can be measured from these thin sections and used based on conditioning and truncation of Gaussian random fields to generate a 3D binary image given its porosity and two-point autocorrelation function (Quiblier 1984, Adler et al. 1992, Roberts 1997). These two constraints are found to be insufficient to reproduce the microstructure of particular media such as grains or sphere packs (Hazlett 1995, Levitz 1998, Kainourgiakis et al. 2000). Another useful method used to characterize the microstructure is the cord length distribution (Roberts and Torquato 1999, Levitz 1998). The pore chord length is the length of the line through the pore space between two solid voxels. It is used as a descriptor to characterize the pore geometry. The cord length distribution functions are calculated by counting the number of chords of a given length. The chord functions have been used to generate a 3D microstructure and for predicting the

microscopic properties (Roberts 1997, Hidajat et al. 2002). These descriptors surpass the simple one- and two- point correlation functions in characterizing the structure while these methods contain some connectedness information along the line and reflect a wide range of information over the system. Hence this combination between the two-point correlation function and the chord length distribution can further improve the resulting 3D microstructure and can better describe the microscopic properties such as permeability (Talukdar et al. 2002).

5.1.3 Process based reconstruction

Contrary to other statistical models process based reconstruction try to take into account the physical processes that create the pore space**.** Bryant et al (1993) developed a process-based model for sedimentary rocks by modeling different rock forming process such as compaction and cementation on a packing of equal spheres constructed by Finney (1968). For instance, diagenesis was modeled by uniformly swelling the spheres and allowing them to overlap and compaction was modeled by moving the centers of the spheres vertically and bring them closer together also allowing them to overlap. This approach has shown how different geological processes affect the pore structure hence the permeability of sedimentary rocks (cade 1994). Using this method, they were able to predict the absolute and relative permeability, capillary pressure, and electrical and elastic properties of water-wet, sand pack, sphere packs, and a cemented quartz sandstone. This was a major advancement in pore scale modeling. However, the predict ability of the model was restricted by the assumption of constant grain size. Bakke and Øren (1997) developed a process-based reconstruction method where different sized spheres were included, to simulate more sophisticated geological process. Such as sedimentation, and diagenesis processes. The grain size distribution was obtained from direct analysis of the 2D thin sections taking from the rock. The diagenesis were similarly modeled in the work of Bryant et al (1993). The stochastic models have a poor representation to the real sandstone Biswal et al. (1999) whereas the geological reconstruction models gave a good representation of the pores connectivity leading to accurate prediction of the transport properties (Øren and Bakke 2002). Several studies tried to extend this work to simulate the deposition of non-spherical shaped grains so the model can be generalized to include other types of rocks (Pilotti 2000, Coehlo et al. 1997) Figure 3 comparing micro-Ct and process based image.

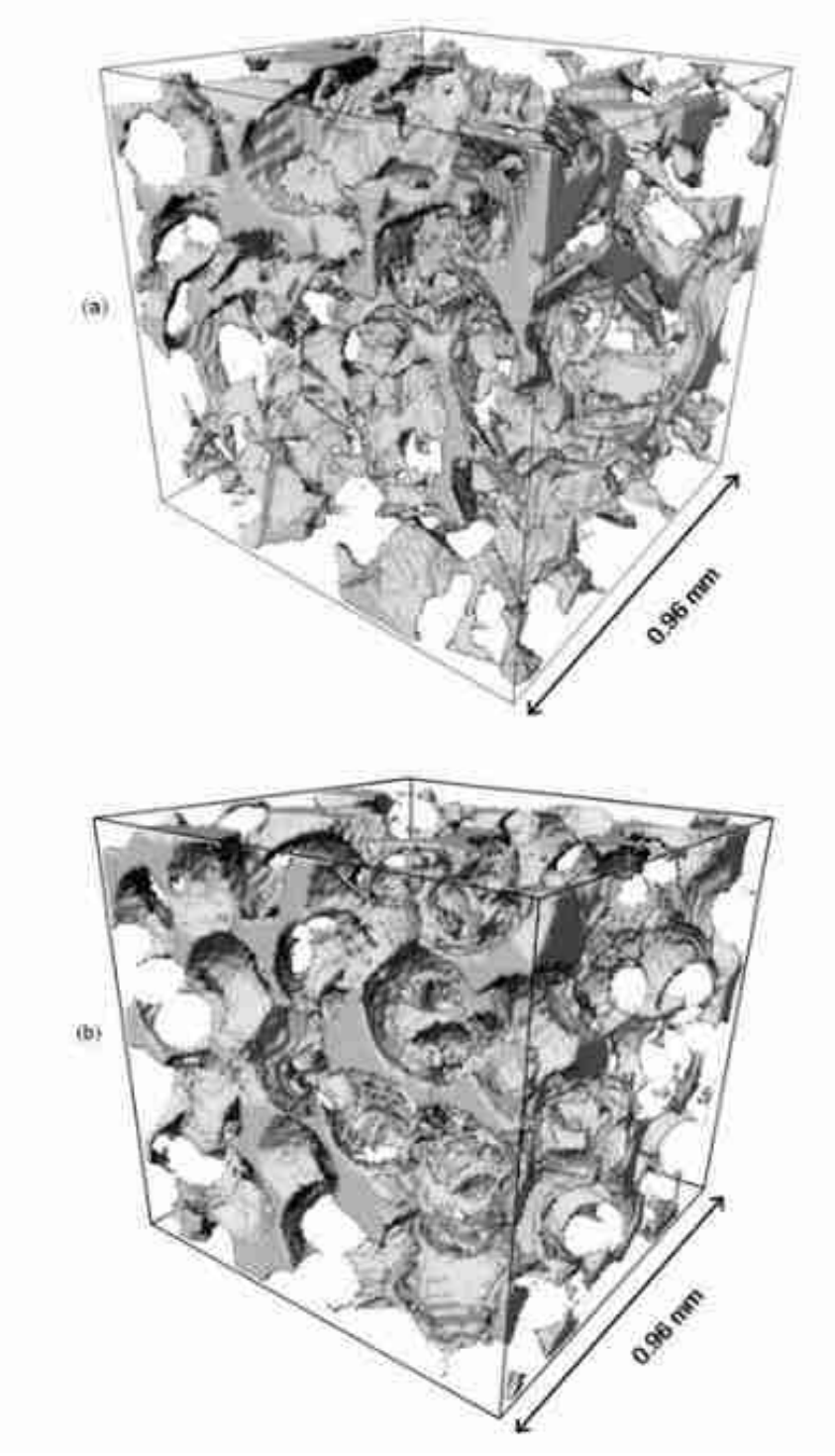

Figure 3 *Fontainebleau sandstone 3D pore comparison a) of a micro-CT image and b) process based image (Øren and Bakke 2002).*

5.1.4 X-ray computed tomography XCT

All of the previous methods aim to produce a 3D representation of the pore structure. However, as it was mentioned earlier, they all have their own limitations. X-ray computed tomography or XCT is another technique for depicting the internal structure of a reservoir rocks and obtaining a 3D representation. It is a non-destructive technique which can be used to visualize the internal structure of a study object.

CT was invented in the 1972 by British engineer Godfrey Hounsfield of EMI laboratories, England and by Allan Cormack physicist Tufts University, Massachusetts. Hounsfield and Cormack received a Nobel Prize in Physiology and Medicine for 1979 for their contributions to medicine and science. The first micro-CT system was built and conceived by Jim Elliott in the early 1980s (Elliott and Dover 1982). The micro-CT technology has been developed and the possibility of its use in geological and petroleum engineering was soon recognized (Dunsmuir et al. 1991).

Since its invention in the 1970s, X-ray computed tomography (CT) has spread and developed quickly, mostly stimulated by growing medical needs for diagnostic procedures and interventions. The X-ray CT has been used in different fields of geosciences, such as studying microstructural and rock physical properties of geological media, aiding and enhancing production in petroleum geology, or assessing soil contamination or waste repository issues in environmental geology (Cnudde et al. 2006). CT enables the analysis of the interior features of core samples, including bedding features, sedimentary structures, natural and coring-induced fractures, cement distribution, small-scale grain size variation, and density variation (Coles et al., 1991; Orsi et al., 1994; Coles et al., 1998). This method has a wide application in geosciences, including analyses of the complex porosity and pore geometry of carbonate reservoirs (Purcell et al., 2009), rock-fluid analysis (Pyraknolte et al., 1997; Purcell et al., 2009; Wennberg et al., 2009), the performance of diverting agents in unconsolidated sandstones (Vinegar and Wellington, 1987; Wellington & Vinegar, 1987; RIBEIRO et al., 2007A), and many other topics. For instance, Bonner et al. (1994) confirmed fluid migration in rocks by X-ray CT. Schwartz et al. (1994) modeled the fluid flow in porous rocks by combining theoretical simulations with 3D imaging of the material studied. Additionally, according to the considered

rock type, accurate permeability and conductivity estimations are possible using CT (Coker et al. 1996; Coles et al. 1998; Arns et al. 2001, 2004).

Geological porous material can be imaged with two major sources of X-ray radiations, used in micro-CT application: synchrotrons emitting collimated, almost parallel monochromatic X-rays, and so-called industrial CT where the X-ray tubes producing fan- or cone-beam polychromatic X-rays (Figure 4). Synchrotron radiation is superior to X-ray system in terms of achievable spatial resolution and signal-to-noise ratio (Baruchel et al. 2006). But the synchrotron facilities are limited and the operational cost is high. Whereas, the lab based micro-CT have lower X-ray flux but more cost efficient. Thereafter, for studies where a lot of samples is needed the industrial micro-CT would be the system of choice (Oliver Brunke et al. 2008). The first demonstration of X-ray micro tomography to look at geological samples was in 1987 (Flannery et al. 1987) and used synchrotron sources to image a Coconino sandstone with a pixel size of 10 microns (Figure 5). Since then, the micro-CT has been used to study single-phase (Dunsmuir et al. 1991) and two-phase flow (Hazeltt et al. 1995). It has also been used to extract pore statistical information such as pore surface, volume ratios, average coordination numbers and aspect ratios (Jerauld et al. 1990). When performing a study of a core samples, internal features such as bedding, fractures, pore morphology, grain size and density variation can be analyzed (Coles et al. 1998). Moreover, extensive research has included applications on the complex porosity and pore geometry of carbonate reservoirs and rock-fluid analysis (Purcell et al. 2009). Details on micro-CT scanning will be discussed on chapter 6.

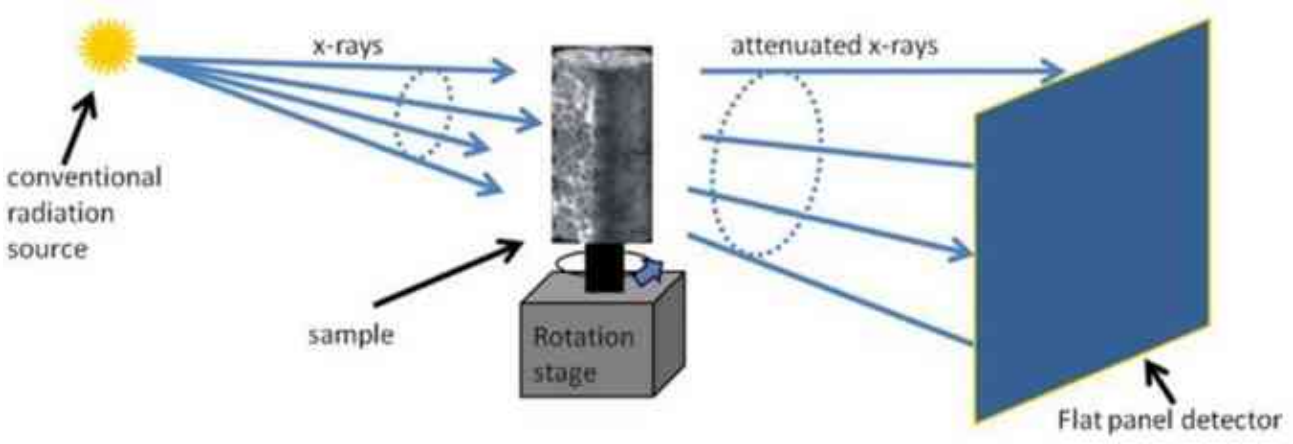

Figure 4 *Cone beam configuration (Wildenschild & Sheppard 2013).*

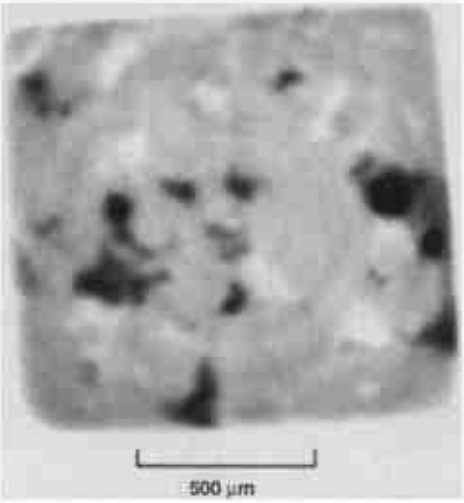

Figure 5 *Tomographic reconstruction of Coconino sandstone from the original work on micro-CT imaging (Flannery 1987).*

5.2 Image segmentation methods

There are numerous attempts to categorize image segmentation methods in the literature. Fu and Mu (1981) categorized segmentation techniques into three classes; characteristic feature thresholding or clustering, edge detection, and region extraction. Haralick and Shapiro (1985) classified image segmentation as: measurement space guided, spatial clustering, single linkage region growing scheme, hybrid linkage region growing scheme, centroid linkage region growing schemes, spatial clustering schemes, and split and merge schemes. Pal et al. (1993) alluded in his study that these previous reviews did not consider fuzzy set theoretic segmentation neural network segmentation and objective evaluation of image segmentation. Pal et al. (1993) classified image segmentation as; gray level thresholding, interactive pixel classification, surface-based segmentation, edge detection, and methods based on fuzzy sets theory. I will briefly discuss different techniques

5.2.1 Gray level thresholding

Gray level thresholding is a popular technique for image segmentation. Thresholding can be achieved based on the histogram of the entire image or by local information such as co-occurrence matrix. By selecting a single threshold value T, separating the foreground pixels

from the background it is called global thresholding and if the image is divided into sub regions by selecting different threshold values for each region is called local thresholding or adaptive thresholding schemes. When the image histogram has different peaks, each corresponding to one region and the peaks are separated by a deep valley, in this case selecting a global threshold value become an easy task. However, normally the case is not like this and the threshold selection need additional study. There are different global thresholding techniques including minimum error thresholding, iterative thresholding, histogram concave analysis, Otsu (Otsu 1979), optimal thresholding, and entropy-based thresholding. Well-known global thresholding method is Otsu (Otsu 1979) where he improved the class separately by maximizing the ratio between class variance and local variance to obtain the threshold. Entropy based thresholding is another technique where the chosen threshold maximizes a known posterior entropy of the image. Pun (1980) suggested a new threshold selection method by using the derivation of entropic threshold for images having irregular histograms. In the local thresholds methods the image subdivided into multiple regions by multiple threshold values. Several techniques were proposed such as Niblack's technique (Niblack 1985) technique which were basically used for text recognition also Bernsen's technique (Bernsen 1986) were he used the local contrast to binarize the image locally. Dynamic thresholding is another thresholding technique similar to local thresholding in dividing the image into regions by multiple thresholds, additionally, this method allows for the thresholding by various dynamic gray values for an object that resides in various grayscales. This method includes but not limited to watershed, image thresholding, and interpolation thresholding (Kang 2009).

5.2.2 Interactive pixel classification

Interactive pixel classification can be subdivided into relaxation, Markov random field (MRF) based approaches and neural network-based approaches.

Relaxation is an iterative approach to segmentation where each pixel's classification decision can be made simultaneously. The decisions made at neighboring points in the current iteration are then integrated in the next iteration to make a decision. Relaxation can be classified into two types probabilistic and fuzzy.

MRF based approaches is a multidimensional extension of Markov chains. This method uses the spatial interaction model to model a digital image. Where, the marginal density of any

random variable X_i depends only on the neighboring points in the image but not on all image points. MRF was generally proposed in image segmentation by Geman and Geman (1984) and been broadly used in edge detection (Zerubia et al. 1993) and image restoration (Blake 1989) long range motion and image classification (Kato 1996). Held (1997) is an example of 3D image segmentation using MRF where the parameters were computed from some manually labeled training samples and the image was segmented using a simulated annealing algorithm.

Neural network-based approaches; Neural networks are vast networks of simple processors (artificial neurons or nodes) that are massively connected. These nodes are associated with a particular wight and threshold. Babaguchi et al. (1990) used multi layers network trained with back propagation for thresholding the image, where, semantic segmentation can be done using convolutional neural networks (CNN), as each pixel is assigned to a class or label (Wei et al. 2016) . CNN can be trained using unsupervised or supervised machine learning algorithms for image segmentation. There are typically three types of layers in CNN: 1) convolutional layer where a small region of the input neuron is connected to a hidden layer, 2) pooling layer to reduce the dimensionality of the feature map. 3) Fully connected layer from the last few layers in the network. Sultana et al. (2020) categorized the CNN based segmentation models on the basis of the most important feature as; based on Fully Convolutional Network (FCN), based on dilatation/ Atrous convolution such as DeepLab, based on top down/ bottom up approach as Deconvnet, based on global context as ParseNet, based on receptive field enlargement and multi-scale context incorporation as Pyramid Scene Parsing Network (PSPNet).

5.2.3 Edge detection

The edge in an image may be described as the boundary that separates two different image regions. The operation of image detection is the procedure to detect and localize these boundaries of sharp discontinuities in the image (Kirti 2017). Edge detection-based segmentation is referring to the boundaries where an abrupt change in intensities or brightness values occur. Essentially, by detecting the edges of an object this will mark the boundary of the object and the object can be segmented from the image. There are three fundamental steps in edge detection:

-filtering and enhancement; in order to suppress the noise presented in the image.

-detection of edge points by differentiating between noise and edges and deciding which one should be retained.

-edge localization; determining the exact location of an edge.

Moreover, there are two main techniques used for edge detection; the gray histogram, and the gradient-based approach (Kaur 2014). The gradient-based segmentation can be described as associating the boundaries of the object of interest with the intensity of the gradient crests observed in an image. Some of the popular methods used for edge detection are Sobel operator, canny operator, and Robert's operator.

5.2.4 Region based segmentation

In this technique the image is partitioned based on pixel similarities. Connected pixels with similar properties are grouped, and the image is partitioned into regions. Region based segmentation can be categorized into two types: region growing and splitting and merging techniques (Khokher 2012).

Region growing: In this method the image can be segmented into regions based on a growing seed point (initial pixels). These seeds can be selected either manually on the basis of a prior knowledge or it can be automated based on a certain application. The growing of the seeds are controlled by the connectivity of the pixels with similar properties and the growing of the pixels can be stopped based on a prior knowledge of the problem.

Region splitting and merging: This method uses two techniques first iterative splitting of the image into regions based on similarities. Subsequently, merging occurs to combine adjacent regions that exhibit similarities.

5.2.5 Clustering based segmentation

Clustering technique is used to organize objects into a meaningful structure based on some similarities between objects. In such a structure, the similarities between objects in the same group are high while the similarities between objects in different groups are low. Hierarchical clustering is a method of cluster analysis where the algorithm builds a hierarchy of clusters either in agglomerative or divisive mode. In the cases of partitional clustering algorithms, the algorithms find all the clusters simultaneously, as a partition of the data, and do not impose a

hierarchical structure. The most popular and simplest partitional algorithm is *K*-means clustering (Jain. 2010). Clustering is divided into two types hard and soft clustering.

In hard clustering the clustering of the image pixels is achieved in a way that one pixel can only belong to one cluster whereas, in soft clustering the division of pixels is not strict and the pixel can belong to more than one cluster. Fuzzy c-means is a popular method of soft clustering where the pixels are portioned into clusters based on a membership function.

5.3 Pore reconstruction

After the segmentation of the gray level images for separating the void space (pore space) from the solid phase (matrix), a three-dimensional binary image can be obtained representing the pore space and the porosity can be measured along with a morphological description of the pore space. Subsequently, the pore and throat type can be built for petrophysical analysis. Figure 6 shows the workflow for generating the pore network model (PNM).

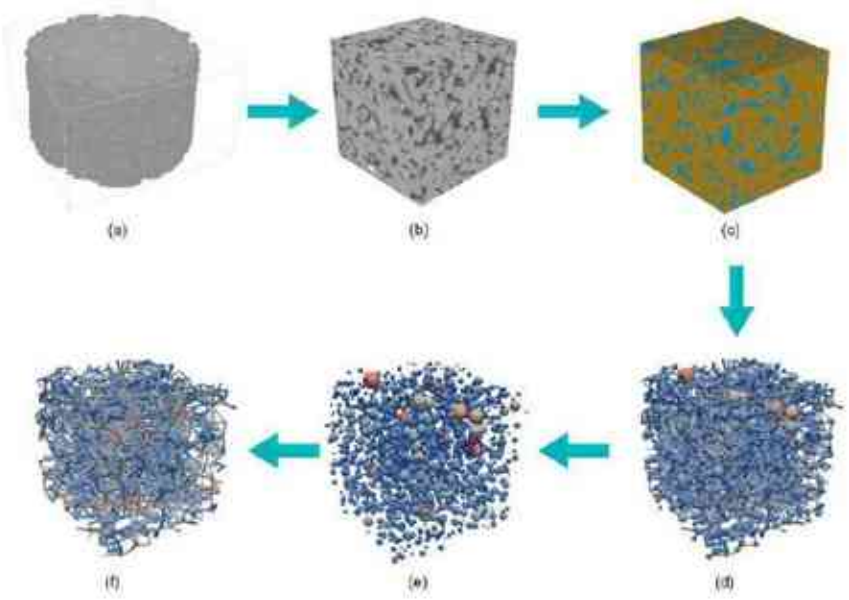

Figure 6 *Workflow to generate the pore network model (PNM). a) the original sample 3D volume; b) the sub- volume; c) the binary sub-volume; d) the full PNM, including nodes and links; e) nodes in the PNM; and f) links in the PNM. After Gong et al. (2020).*

A successfully built network model should represent the real pore space in terms of geometrical and topological characteristics of the porous media. Based on the work of Xiong et al. (2016), there are three ways to achieve and build a representative PNM. The first model is achieved by building a statistically equivalent network using the distribution of basic morphologic parameters. This model generates a PNM only statistically equivalent to the modeled system. The second approach uses a direct mapping of the network structure onto a specific porous medium. This technique offers one-to-one spatial correspondence between the comparable network structure and the porous medium structure. The last model is called grain- based approach, based on the diagenesis of porous media (Xiong et al. 2016).

Two of the direct mapping methods will be briefly illustrated;

5.3.1 Medial axis method

The medial axis algorithm transforms the pore space into a medial axis that is the reduced representation of the pore space (Figure 7) acting as a topological skeleton roughly running along the middle of the pore channels either by a thinning algorithm (Baldwin et al. 1996) or a pore space burning algorithm (Lindquist et al. 1996). The pore space partitioning can be validated along the skeleton to decide the pore throat by local minima along branches of pore bodies at the nodes (Lindquist et al. 1996). During the thinning procedure a clean-up process of the pore skeleton is done by removing the points with some additional geometrical constraints along the pore skeleton until no more points can be deleted (Lindquist et al. 1999). One advantage of this method is that it preserves basic topological and morphological properties of the entire pore space. However, due to the intrinsic sensitivity of the algorithm to noise in digitalized images a clean-up process needs to be performed thus, it is hard to identify pores unambiguously (Lindquist et al. 1999). Moreover, they typically cover more than one medial axis junction to adequately trim the skeleton and fuse the junctions together while avoiding unreasonably high coordination numbers; various merging methods must be created (Sheppard et al. 2005). Where the coordination number refers to the number of neighboring pores or void spaces that are directly connected to a given pore or void.

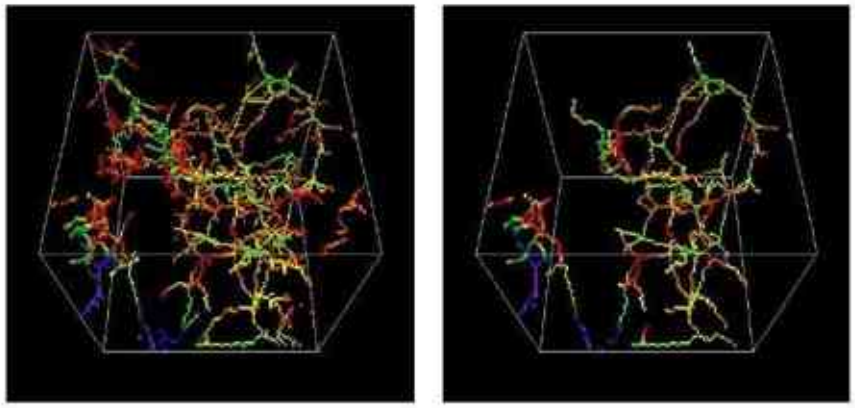

Figure 7 *The left picture shows the medial axis extracted from a small region of a Berea sandstone image (voxel side length is 4.93 µm); the right one is the set of medial axis after trimming all dead ends where no fluid flow through. The colors represent, in rainbow scale, distance to the closest (at least two) grain voxels (http://www.ams.sunysb.edu/~lindquis/3dma/3dma_rock/3dma_rock.html).*

5.3.2 Maximal ball (MP)

The maximal ball method also denoted as MB starts from each voxel in the pore space to find the largest inscribed spheres that just touch the grain or the pore boundary Figure 8. Then those included in other spheres are viewed as inclusion and removed; the rest are called maximal balls and describe the pore space without redundancy. Locally the largest maximal balls identify the pores while the smallest balls between pores are the throats. The maximal balls were used mainly for calculating the dimensionless capillary pressure for the space rather than to extract a pore network from the image (Silin et al. 2003, 2006). A MB must touch the grain surface and so MBs cannot be a subset of any other MB. Therefore, every MB is in possession of at least one voxel that is not contained in any other MB. The aggregate of all MBs defines the void space in a rock image without redundancy. This method was later developed by Al-Kharusi and Blunt (2007) to investigate the pore space of sandstones and carbonates. Their method has similar starting point of finding maximal ball at each voxel, then they have developed a more extensive set of criteria for determining the optimal ball hierarchy. While in Silin et al ‘s (2007) work only two criteria of relations are defined masters and slave which corresponds to the bigger and smaller balls respectively compared to their neighbors.

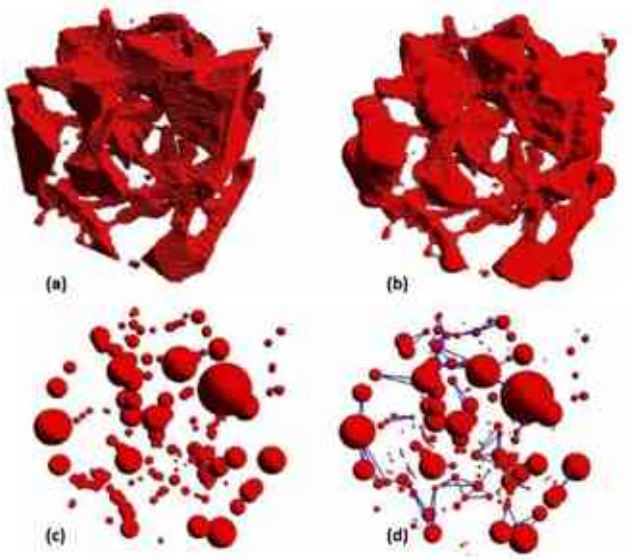

Figure 8 *a) is the pore space image of a Fontainebeau sandstone with a porosity of 17%; b) is maximal balls in the pore space. The dimensionless sizes of the images are 200 × 200 × 200 counted in voxels; c) shows the master balls (pores) found in a); d) are the pores and their connectivity of the pore space. Modified after Dong et al. (2007).*

In Al-Kharusi and Blunt (2007) new relationship was introduced where they included the cluster to hold nearby maximal balls of the same size (Figure 9). Which resolved the problem of uncertainty caused by these identical balls after changing the pore space to maximal balls from the voxels. Their model was successful in predicting the absolute permeability; however, it requires a huge memory usage therefore it was limited for small data sets which contains fewer than a thousand pores.

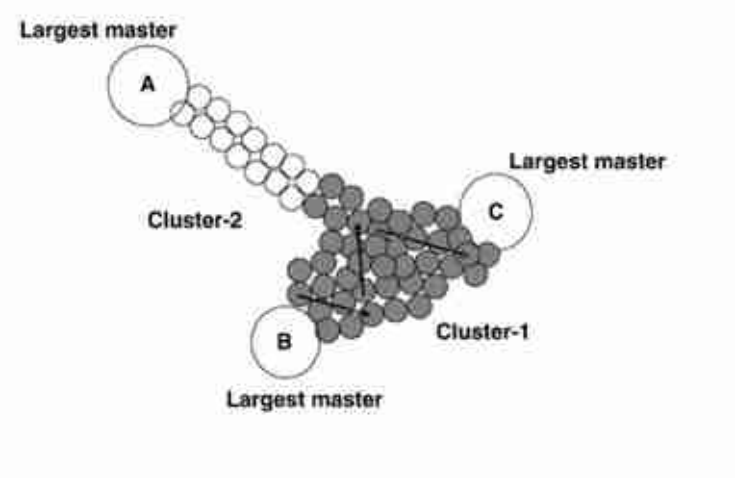

Figure 9 *Clusters are defined to fuse the identical spheres in the pore space. (Al- Kharusi and Blunt 2007).*

6. Materials

6.1 Geological background of the studied cores

The Pannonian Basin was formed over three mega-structural facies units (terranes) the ALCAPA, the Tisza, and the Mid-Hungarian Mega-units Figure 10 (Haas et al. 2010).

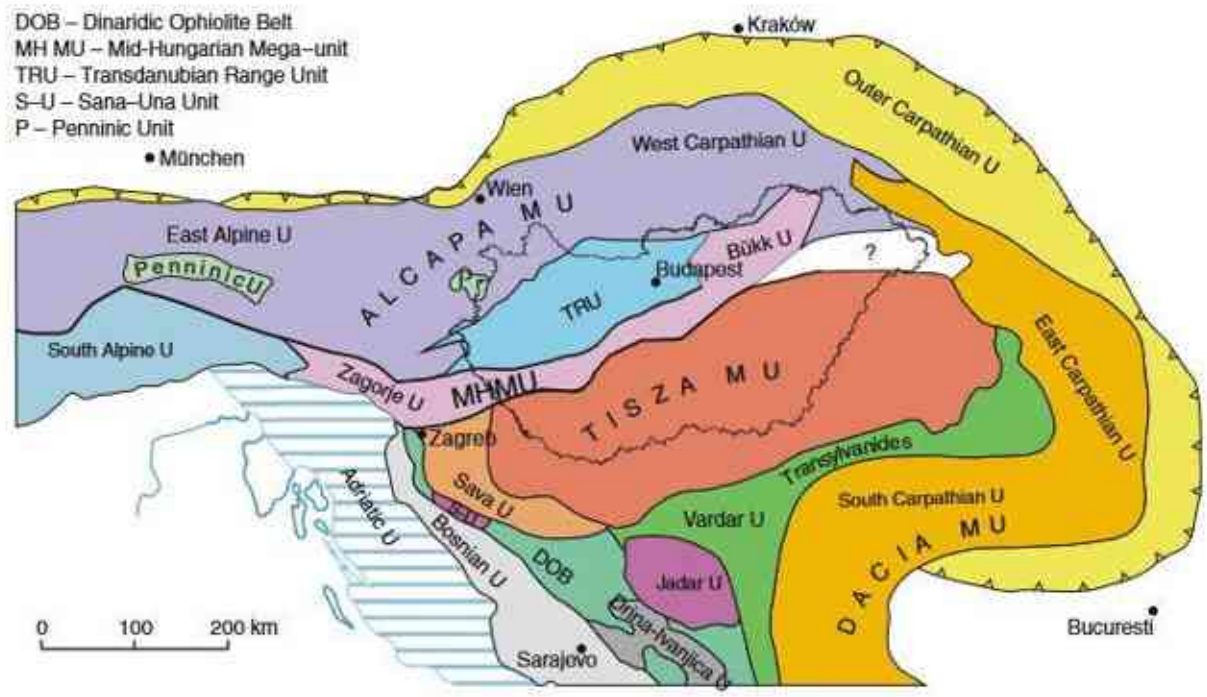

Figure 10 *The main structural units of pre-Cenozoic basement of the Carpathic- Balkan – Dinaric region after Haas et al (2010).*

From tecto–palaeogeographical point of view the evolution of the Pannonian Basin took place in three stages;

1- Stretching of the Pannonian lithosphere during the first half of the middle Miocene.

2- In the Badenian (middle miocene) pelagic basins were formed and opened in the trenches in the Karpathian, where fine grained siliciclastic sediments were deposited. During the sea-level rise in the middle Badenian, carbonate sediments took place in the shallow marine

environments, while sedimentation was characterized by fine-grained siliciclastic deposits in the deep marine environments (Budai and Maros, 2018). At the beginning of the Sarmatian (middle Miocene) volcanic activity renewed with riolitic tuff falls, followed by carbonate sedimentation in shallow marine shelf environments (Budai and Maros, 2018).

3- By the beginning of late Miocene due to orogeny uplift and major eustatic sea-level drop, the Intra-Carpathian area became separated from the Paratethys. In the Pannonian the lacustrine sediments started with a widespread unconformity (Sztanó et al. 2013)

6.1.2 Sarmatian limestone

The Sarmatian limestone samples originated from a cored section of a well drilled in the Mid-Hungarian Mega-unit on the northern part of Somogy-Drava basin, SW Hungary.

Sarmatian belongs to the middle part of the Miocene series. Jámbor (1977) in agreement with Kókay (1989) divided the Sarmatian strata into three different parts: 1) Lower limestone, calcareous marl; 2) middle part alternations of alginitic clay and sand layers, 3) upper part: ooidic limestone.

Rögl and Steininger (1984) illustrated two sea level rising and falling cycles during Sarmatian. Based on gastropods foraminifera and ostracods studies. Cornée et al. (2009) showed two sedimentary units in the Samaritan limestone. The lower one consists of underwater dunes, its age is Elphidium regium - Elphidium hauerinum zones, the age of the upper cycle is Spirolina austriaca zone. Additionally, an erosion surface separating the two units, which can be traced regionally within the Spirolina austriaca zone. This erosion surface is a result of a terrestrial event occurred in between the cycles when the upper part of the lower unit is eroded in the late Sarmatian during the Spirolina austriaca zone. The two units correspond to fourth-order cycle according to Cornée et al. (2009).

Figure 11 depicts the location of our samples.

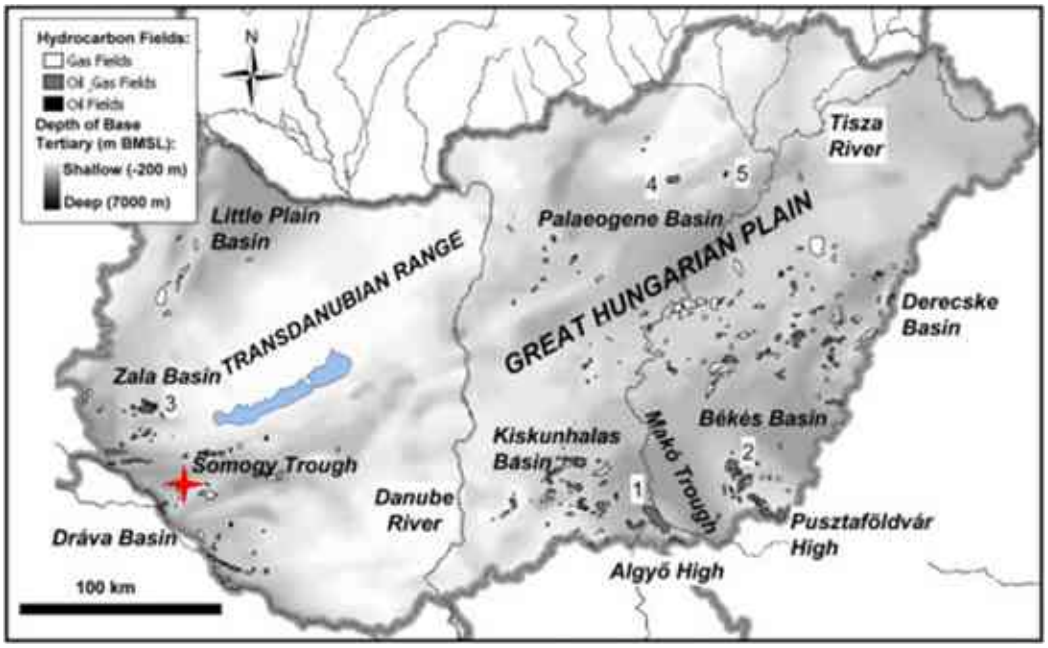

Figure 11 *Sample location marked with a red star at the Drava basin after Balázs et al. (2012)*

Ooidic-bioclastic aggrading – prograding underwater dunes make up the lower unit which was deposited on a ramp. The lagoon and inner ramp are the sources of the dunes' material. Seldomly bryozoan patch reefs occur as well. The sediment of upper unit consists of ooliths. Wind and wave action governed the upper unit's sedimentation. For the lower unit the estimated water depth is several to 50 m whereas its only several meters for the upper unit.

6.2 A detailed description of the studied cores

The investigated samples originate from an oil well drilled in the Mid-Hungarian Mega-Unit on the Northern part of the Somogy Dráva basin, SW Hungary. The well penetrated 24.5 m Sarmatian (Middle Miocene) limestone (Figure. 12). The reason I have chosen this part of the Pannonian Basin is the object of the study because it had not been extensively studied using micro-CT scanning techniques before, making it a unique opportunity to explore new ground in reservoir characterization.

Furthermore, carbonate reservoirs, due to their inherent complexity, have long been an area of interest and challenge for the oil and gas industry. However, there has been a notable gap in comprehensive studies and detailed investigations of these reservoirs in this region.

For the analysis, four samples were used from two different depth intervals. Two samples were from the upper interval of the shallow marine Sarmatian limestone (Mukhtar 2020) and two others from a lower interval of marine Sarmatian limestone. The depths of the samples from the upper part are 1966 m (the sample ID is 1966) and 1967 m (sample ID is 1967), and from the lower part are 1979 m (sample ID 1979) and 1980 m (sample ID is 1980). He porosity and N-permeability for sample 1966 were 21% porosity and 33 mD permeability, respectively, with 28% porosity, and 55 mD permeability, for sample 1967. However, for the other two samples from the lower part the measured porosity and permeability were very low at 12.41% and 0.07 mD for sample 1979, and for sample 1980 they were 11.83% and 0.0037 mD. For all samples, cylindrical plugs were taken from the main cores with a diameter of 2 mm for μ-CT acquisition. The samples were scanned by the YXLON FF35 CT industrial micro-computed tomography in the 3DLab at the university of Miskolc, the scanning parameters were: scan type cone beam stop and go, 140 (KV) accelerating voltage, focus object distance 8 mm, focus detector distance 700 mm, and voxel size 2 μm. The number of images resulted from 1000 scans for each sample. For image segmentation and segmentation evaluation, one tomogram was used. To avoid artifacts occurring on the edges of the scanned sample – such as beam hardening – a sub volume in the middle part of the image was extracted for segmentation. The resolution of the extracted sub-volume lattice for the four samples was $680 \times 660 \times 1000$ with a pixel size of 2 μm Figure 12.

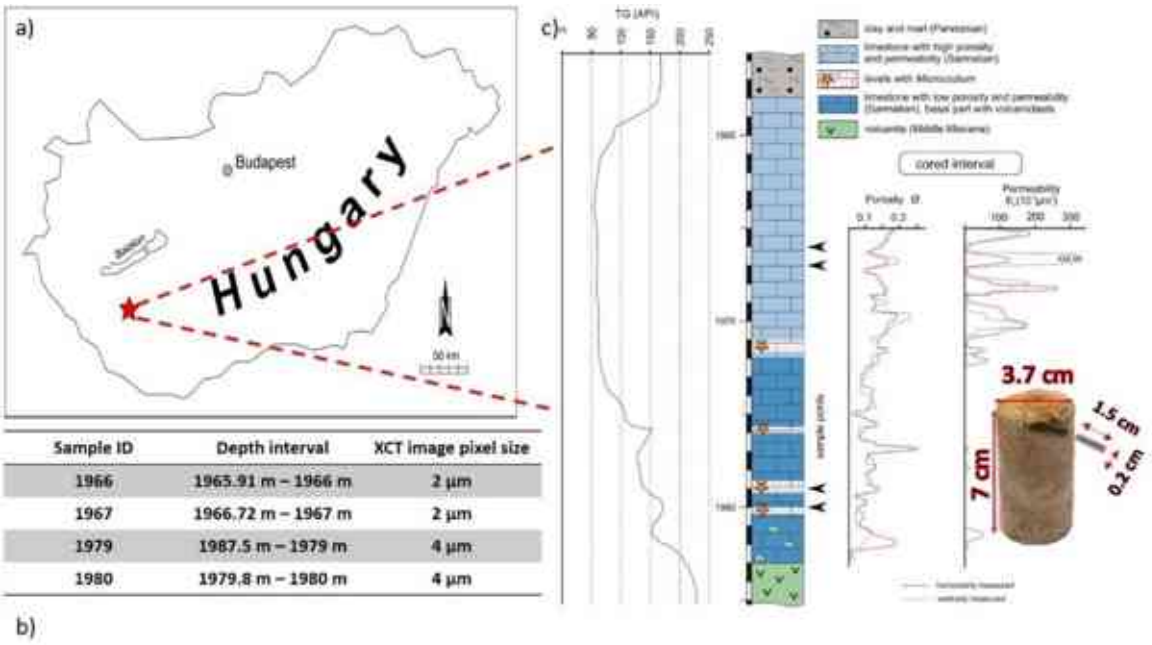

Sample ID	Depth interval	XCT image pixel size
1966	1965.91 m – 1966 m	2 µm
1967	1966.72 m – 1967 m	2 µm
1979	1987.5 m – 1979 m	4 µm
1980	1979,8 m – 1980 m	4 µm

Figure 12 *a) well location, b) sample description, c) Gamma-ray log (TG) & lithological column. The black arrows indicate the position of the cores, porosity permeability logs for the cored interval and sample dimensions used for micro-XCT scan to the right (edited by H.A.).*

6.3 The results of thin section analyses in the productive and dry reservoir sections

The aim of the microfacies analyses was to detect any differences in the depositional and diagenetic environments between the productive and dry rocks.

For microfacies analyses blue-dyed epoxy was used. After polishing the rock sample, it was dipped in blue epoxy resin which fills the pores. Under the microscope the pores appear as blue patches, enabling the pores to be easily distinguished from the components and matrix of the rock.

Because large parts of the calcareous sediments consist of the chemically instable aragonite, diagenesis plays a much bigger role in the case of carbonate reservoirs than in siliciclastic ones. When calcareous mud is deposited it is plastic. During diagenesis it is compacted and fluids with different composition infiltrate the calcareous mud.

The chemical composition and the CO_2 content of the circulating interstitial water determines whether or not dissolution or precipitation of calcareous cement will dominate during

diagenesis. If the circulating interstitial water is undersaturated in $CaCO_3$ dissolution will take place and secondary pores will be created. Porosity will be increased. If the circulating water is saturated in $CaCO_3$ the pores will be filled with cement, reducing or even eliminating porosity. Based on the composition of the waters in the pores we differentiate meteoric marine and deep burial diagenetic environments. The cement crystals precipitating in different diagenetic environments are specific to the diagenetic environment in which they originate.

In the marine diagenetic environment, the pores are filled by sea water.

Meteoric diagenesis occurs at or near seawater. The meteoric environment is divided into vadose (above the water table) and phreatic (under the water table) zones. In the vadose meteoric environment the pores are filled with air and fresh water and in the phreatic meteoric with a mixture of fresh and sea water (Scholle and Ulmer-Scholle 2003).

Samples 1966, 1967 (productive interval)

The porosity of the rocks is 28% and 25% respectively. Both the matrix and most components (fossils, grains) are dissolved. The rock consists more or less of a frame of micritic envelopes (Figure 13e).

Sediment deposition happened in a marine environment. After deposition rims of grains and fossils were micritized due to organic activity. Later the diagenesis continued in a meteoric phreatic environment. Here the interstitial water is a mixture of fresh and marine water, which is under saturated in $CaCO_3$. Dissolution dominated. All aragonitic components, fossils, the grains, and even the matrix were dissolved. Only the micritic envelope resisted outlining deposition of the dissolved aragonitic components. The envelopes have a thin coating of phreatic calcite cement, referring to meteoric phreatic diagenetic environments also.

Samples 1979, 1980 (dry interval)

In the micritic matrix fossils such as foraminifera (Figure 14a) algae and other fossil fragments can be found.

The rock consists of glaebules (incipient nodules) with spar-filled circumgranular shrinkage cracks, Figure 14d). Microcodium also appears in large quantities. Microcodium is characterised by tubular fabrics around the roots of terrestrial plants (Scholle and Ulmer-Scholle 2003).

Because of the presence of foraminifera and algae I can conclude that the sediment was deposited in a marine environment. Diagenesis started in subaerial exposure which is evidenced by the presence of Microcodiums and dessication cracks. The diagenesis was finished in a marine environment where all pores were filled by mosaic calcite.

Comparison of the productive and dry rocks clearly demonstrates that the diagenetic environment has a profound influence on porosity increase and decrease. In our case the sediments of both the productive and the dry intervals were deposited in marine environments, but the diagenesis of the productive rocks happened in the meteoric phreatic, whereas the diagenesis of the dry rocks started in a meteoric vadose environment and finished in a marine environment.

We can conclude that during diagenesis of the productive rocks the relative sea level decreased considerably, while in the dry rocks an initial decrease of the relative sea level caused subaerial exposure, which was followed by a relative sea level increase, covering the area with sea water.

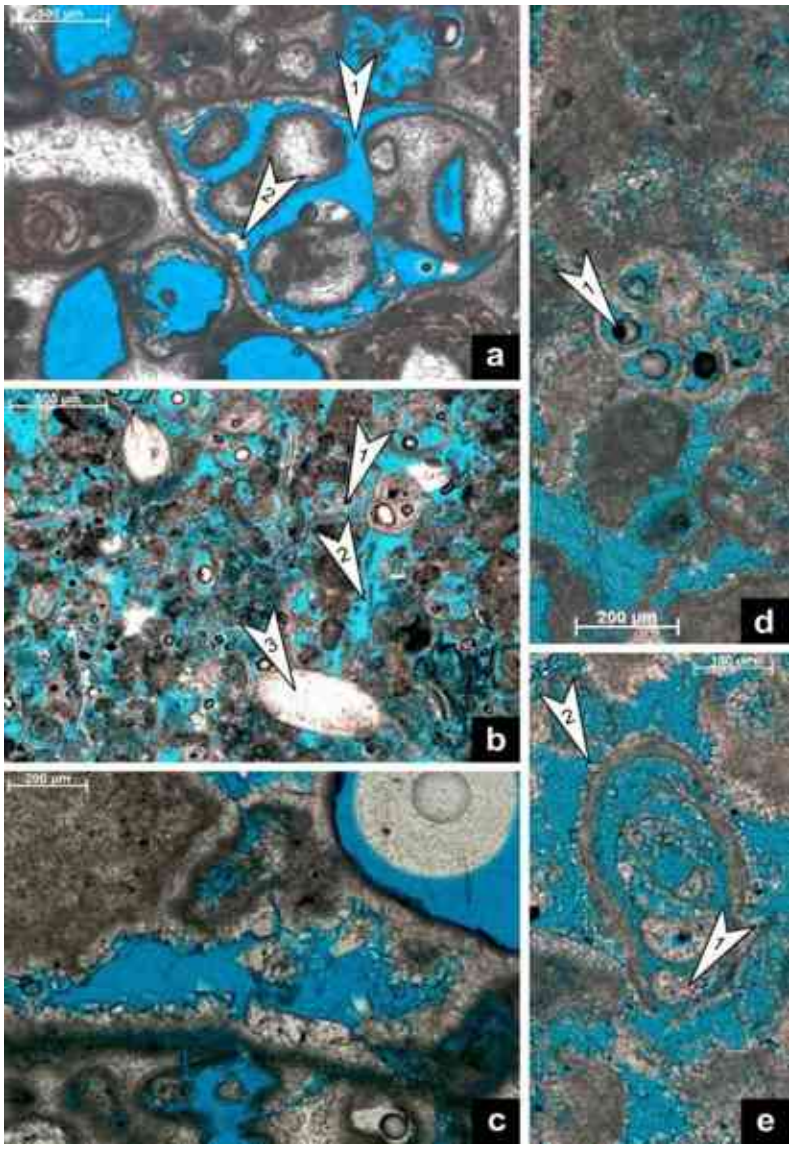

Figure 13 *a) Moldic porosity. The shell of a gastropod was totally dissolved creating moldic porosity (arrow 1). In the meteoric phreatic zone bladed cement crystals precipitated on the internal wall of the moldic pore (arrow 2). Well.4-7.3 1966 m, horizontal thin section. b) Intra- and interparticle pores. The primary pores within the fossils remained empty (primary pores: arrow 1), and during meteoritic diagenesis the majority of the matrix was dissolved creating secondary intergranular pores (arrow 2). Note, that shells of the ostracods were not separated after the death of the animal and were later filled by calcite (arrow 3). Well.4-7.2 1967 m vertical thin section. c) Dog tooth cement. On the edge of the pore bladed calcite cements precipitated in freshwater phreatic zone. Well.4-7.3 1966 m. Horizontal thin section. d) Intra-and interparticle porosity. The internal part of the foraminifera chambers remains empty, forming primary porosity (arrow 1). During diagenesis much of the matrix was*

dissolved by secondary intergranular pores being created. Well.4-7.2 1967 m horizontal thin section. e) During diagenesis the original chambers of the foraminifera were partly filled by calcite cement (arrow 1). On the outer part of the shell bladed calcite cements were precipitated in the fresh water phreatic zone (arrow 2). The bio and intraclasts were partly dissolved and on their outer parts bladed cement precipitated. Well.4-7.2 1967 m, vertical thin section (edited by H.A.).

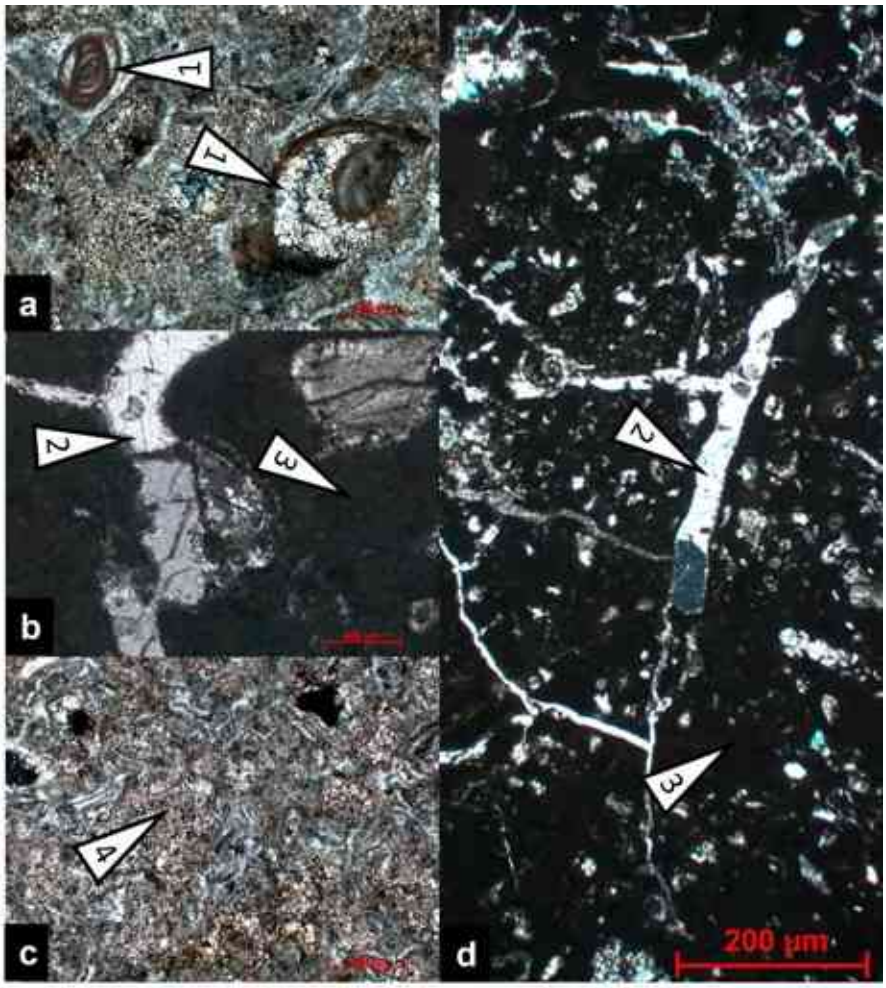

Figure 14 *Horizontal thin sections from the lower interval samples a) The shell of a foraminifera was partly dissolved creating moldic porosity during a relative see level drop followed by infiltration of freshwater. Later, in a deeper water environment, rapid cementation occurred, and the moldic porosity was entirely filled with mosaic calcite. (arrow 1). b) Channels were completely filled by mosaic calcite (arrow 2). The rock matrix was totally dissolved and replaced by carbonate mud precipitation (arrow 3). c) The matrix was replaced by mosaic calcite (arrow 4). d) Channels and pores were filled by mosaic calcite and the matrix was replaced by carbonate mud (edited by H.A.).*

7. Methods

7.1 XCT imaging

X-ray computed tomography (CT) is a non-destructive tool that is used widely in geoscience. It can be used for making three-dimensional reconstruction of the variation of attenuation through the object of study. The data obtained from this technique is digitalized making it suitable for quantitative analysis. The foundation of X-ray CT lies in X-ray radiography, of which the main components are an X-ray source, an object that is irradiated and a detector that measures the attenuated X-rays. As result a radiograph is produced. Unlike a few two-dimensional radiographs which causes a loss of depth information X-ray computed tomography, or CT, provides a complete 3D reconstruction of the original structure of the sample which enables the rock grains and pores to be distinguished.

The principle of 3D reconstruction appeared in the 1970's when a computerized transverse axial tomography was developed. This method acquires multiply sets of radiographs of an object over a range of angular orientations and a 3D volume is reconstructed using computer algorithms (Cnudde & Boone 2013, Ketcham & Carlson 2001). Here at the University of Miskolc, at the Centre for X-ray Tomography, a new generation of (Computer Tomograph YXLON FF35) is used in which a resolution up to 06µm (3D) and 0.15µm (2D) can be detected with dual X-Ray tube. However, in practice I use the 2µm focal spot size to maintain sufficient photon flux radiating through the samples and detected by the detectors panel. The 16-bit digital X-ray Cesium Iodide detectors of this system is a flat panel detector with a pixel size of 150 µm. VGSTUDIO MAX software which is a high-end software for the analysis and visualization of industrial computed tomography (CT) data.

7.1.1 Introduction of the measuring equipment

X-ray CT comprises three fundamental components: the X-ray source, the object subjected to X-ray irradiation, and the detector responsible for capturing attenuated X-rays as 2D projection images. In µ-CT, a series of steps is involved:

Data acquisition: This stage entails correctly positioning the sample in the holder, ensuring that the rotation axis of the sample aligns with that of the holder to maximize magnification.

Scanning parameters, such as energy, radiation intensity, and exposure time, are adjusted to control image contrast. It is crucial to avoid oversaturating the image with excessive white.

X-ray irradiation and data collection: During the measurement process, the sample is exposed to X-rays, and the differences in X-ray absorption properties of materials, depending on their mineral composition, are measured. The measurement data is collected and stored in computer memory.

Reconstruction: The object is irradiated with X-rays and rotated incrementally on a rotational stage, capturing a series of X-ray projection images. These images are acquired over a 180º rotation (or sometimes a 360º rotation, depending on the sample type) to create a comprehensive 3D representation of the object. Subsequently, the attenuated X-rays are measured by the detectors as 2D projection images.

In figure 15a a schematic diagram of micro-CT. In Figure 15b is an illustration of the setups of the desktop micro-CT scanner at the University of Miskolc. The CT scanner uses an industrial tube to irradiate the sample of a bundle of X-rays as a cone beam.

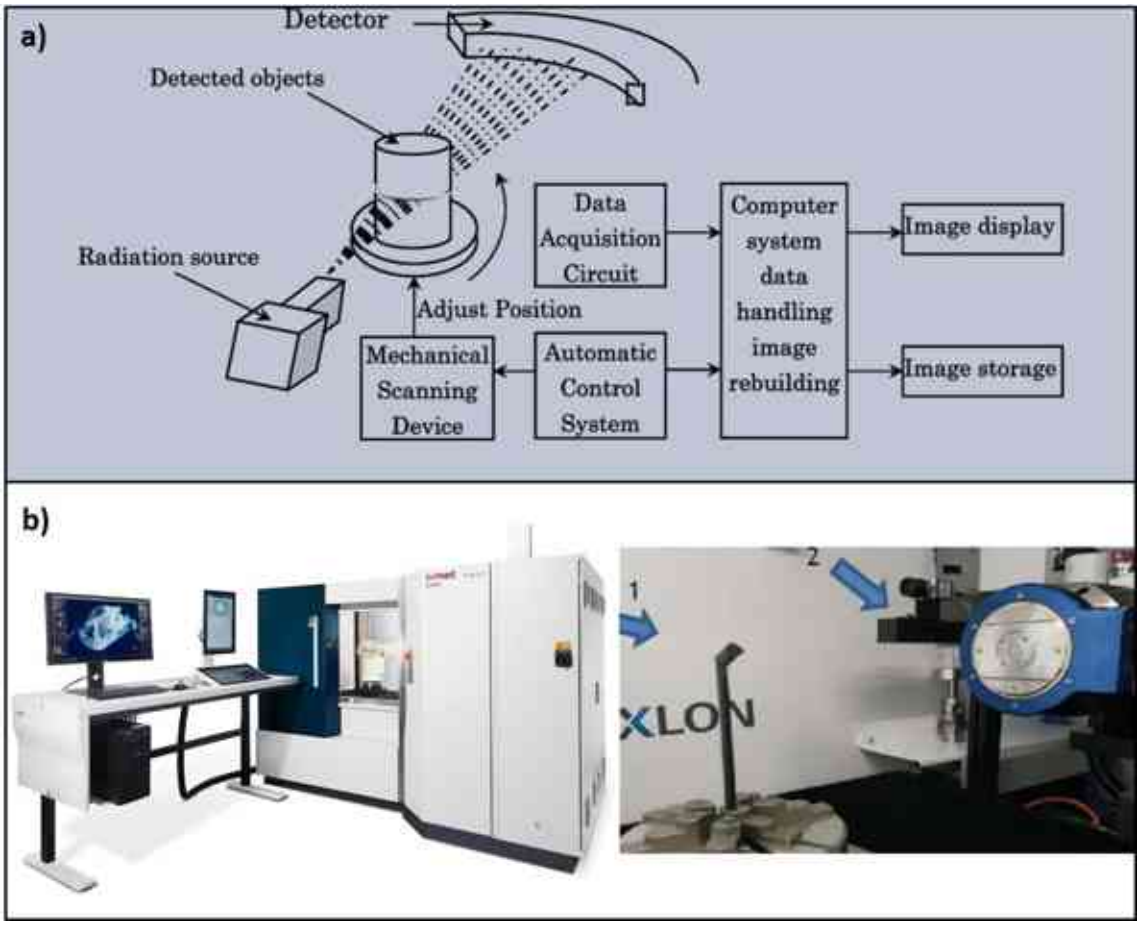

Figure 15 *a) A schematic illustration of micro-CT after Chen et al (2016). b) The setup of the XCT scanner at the University of Miskolc. Arrow one indicates the sample mounted on the rotary table, and arrow two is the X-ray source (edited by H.A.).*

7.1.2. Sample preparation

Since I aimed high resolution images to study the micro pore sizes, there two factors must be considered to achieve the desired results; the influence of the sample size on the resolution, and the detector coverage during the sample rotation. Therefore, the scanned specimen must be small and well-shaped. I used a cylinder column drilling machine to drill out small cylindrical samples from a larger core (Figure 16). To maintain the integrity of the samples from the destructive physical drilling, a relatively large plugs were drilled out, then after, the diameter of the plugs was reduced manually by the use of the sand papers. The typical cylinder diameter of the scans was around 2-4 mm.

Figure 16 *Taking small plug from the sample by using cylinder column drilling machine (edited by H.A.).*

7.1.3 Calibration

A calibration of the machine is necessary before starting the scan. This can be achieved by capturing the correction images to remove the inhomogeneity in the background images for instance taking images with only air in between the source and the detectors. This can be done by the detectors reading one with the X-ray on and another one with the X-ray off and it's called the flat field. This flat field is important to take into account the non-uniformities in the X-ray beam and the ununiform response detector.

7.1.4. Scanning parameters

It is important to setup the measurement parameters of the CT scan before starting the scan which could influence the measurement outcome and thus the uncertainty of measurements. These parameters are the imaging parameters such as (tube voltage, tube current, prefilter, number of projections, etc.). These parameters are mostly defined by the user, based on experience and having some knowledge about the sample to measure and the kind of

information needs to be taken out of the scan. Below is an overview of the factors should be considered while sitting up for the measurement.

7.1.4.1 Selection of the resolution

An important factor before starting the scan is the selection of the resolution that can be obtained from a sample with known dimensions. Since the sample geometry could affect the measurement and increase the artifact therefore it is suggested to use only the central part of the detectors due to two reasons: first, the intensity of the beam cone intended to reduce near the edges, and the second, far from the central slice the reconstruction of the cone beam geometry is not ideal.

7.1.4.2 Voxel size

Voxel size can be defined by the user, the voxel size is defined as the 3D physical dimension of the pixel in the image and it depends on the magnification which is the distance in-between the object and the source. The smaller the voxel size the higher the resolution (Figure 17) but smaller voxel sizes are coupled with longer scan times and large data sets. When considering all of these outcomes, a minimum voxel to object size ratio of 2:1 is a good guideline to follow (Bouxsein et al. 2010).

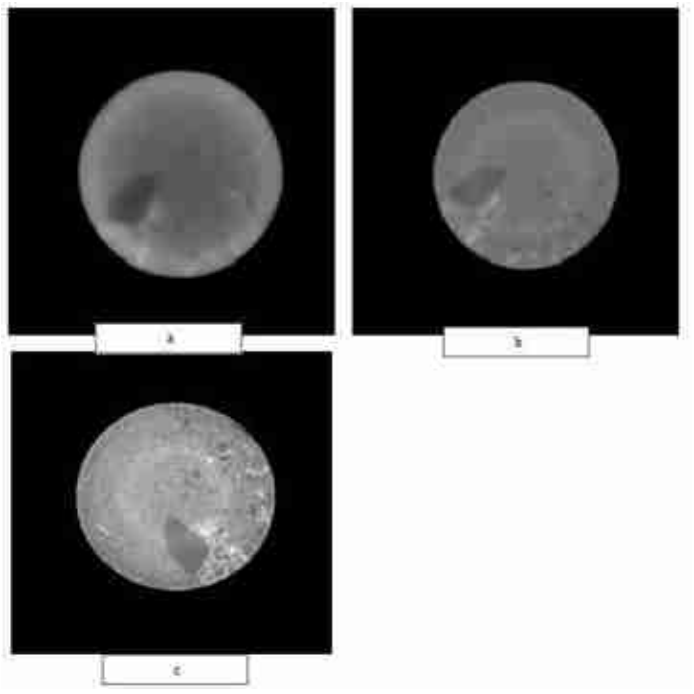

Figure 17 *Three scans taken for the same sample at different resolutions where: a) has a voxel size of 99.7 µm b) has a voxel size of 41.7 µm and c) has a voxel size of 10.4 µm (edited by H.A.).*

7.1.4.3 Number of projections:

The number of the projection image taken during the rotation of the sample until the sample completes its 360 degrees which results in a series of projection images is called number of projections. Low number of projection cause artifacts and acquiring too many projections not only increase the acquisition time but also the reconstruction time of the data. Therefore, before deciding on the number of the projection many factors should be considered such as the sample shape (ex: cylindrical samples take less projection number than a cubic sample (because of the reconstruction of the cubic surfaces), the kind of data needs to be investigated. For instance, if the goal from the scan is to acquire information about the pores the number of projections needs to be high in order to show the desired results and unnecessarily long acquisition time.

7.1.5 Reconstruction

The final three-dimensional images acquired by the CT-scan is proceed from stacking sequence of two-dimensional slice images. These two-dimensional images resulted from a large number of projection images attained by the scanning system.

Then the inversion process take place to produce the special images from projections, employing the filter-back projection algorithm.

This algorithm is adapted to cone geometry and consists of two steps, filtering the projection and back projecting the information on the three-dimensional image volume that represents the scanned sample. The reconstruction software used at University of Miskolc is VG Studio Max 3.1. At the end of the reconstruction stage a stack of two-dimensional slices is produced.

7.1.6 Spatial resolution

The spatial resolution in radiography is defined as the ability of an imaging modality to differentiate two adjacent objects as being distinct from each other. In our case these two objects are the void phase (the pore space), and the solid phase (or the matrix). Pixel size, focal spot size, magnification, slice thickness and detectors size all plays an important role of affecting the spatial resolution. However, since our studied samples are carbonates, a decent spatial resolution down to 2 µm is required where the micro porosity has a great impact on the fluid transport. Examples on different image resolutions are shown in Figures 18 to 20.

The resolution of a CT-system is defined by the resolution of the X-ray source and the detection system. The resolution can be calculated through the following equation (Mouze 1996):

$$R = \frac{d}{M} + (1 - \frac{1}{M})s \quad (1),$$

where:

$$M = \frac{d_c + d_d}{X} \quad (2),$$

with R the achievable resolution in the object, where s is the spot size of the X-ray source, d the resolution of the detector and M the magnification (see Equation 2), which is related to the position of the object, where d_c being the source-object distance and d_d the object-detector distance and x is the lenses radius.

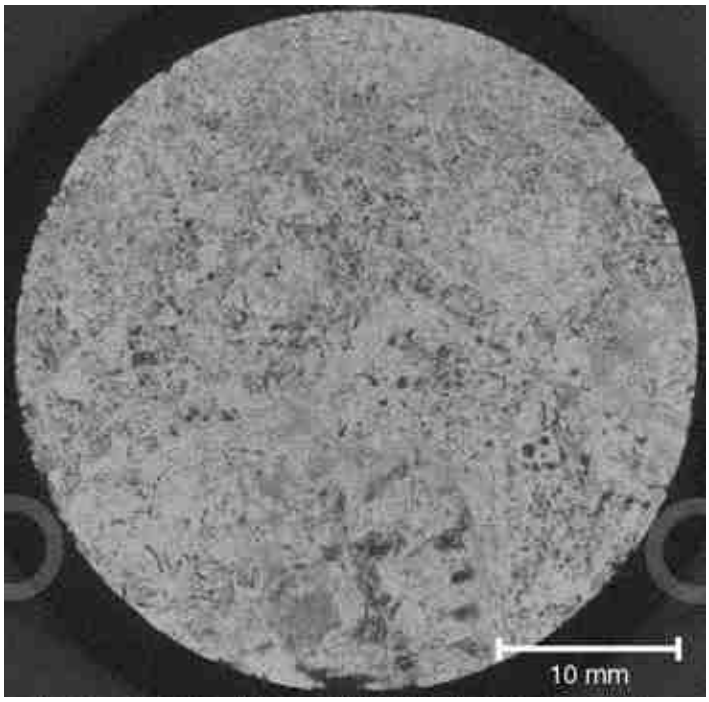

Figure 18 *An example of a carbonate rock image with a resolution of 21 microns (edited by H.A.).*

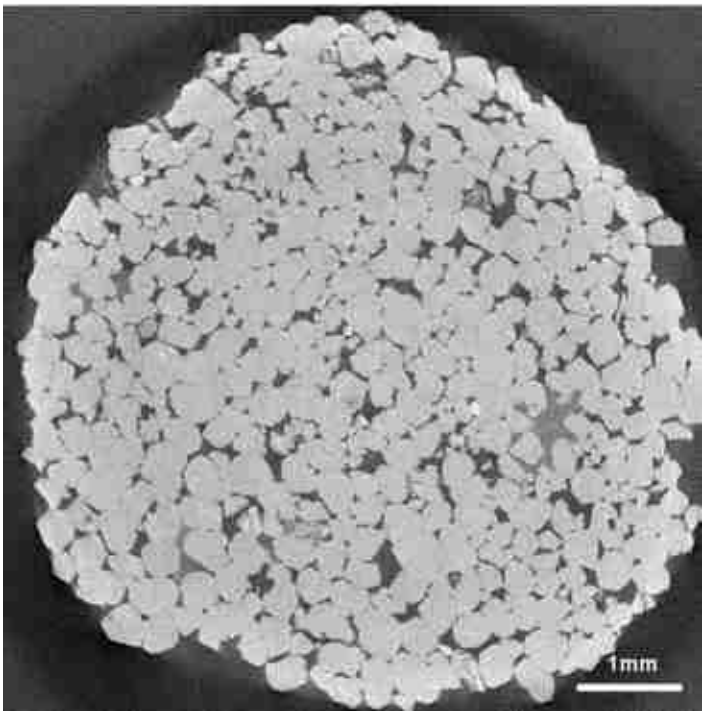

Figure 19 *An example of unconsolidated sandstone image with a voxel size of 8 microns. After Dong et al. (2007).*

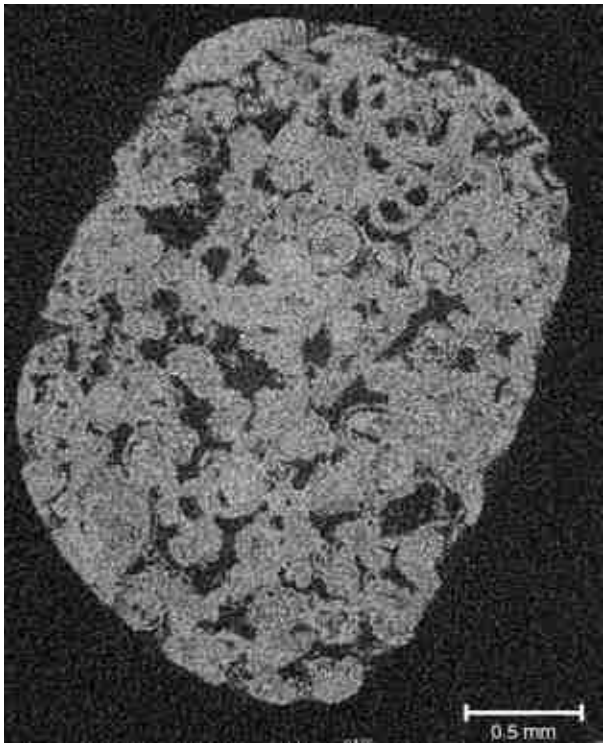

Figure 20 *Sample 1967, an example of carbonate rock image with a resolution of 2 microns (edited by H.A.).*

7.1.7 X-ray attenuation

X-Ray attenuation is the reduction of intensity of the X-ray beam when it passes through the subject. Energy scattering and absorption are the main reasons for the attenuation of the X- ray beam and it can be affected by many factors like atomic number, density of the absorber, and beam energy. The denser the object or the higher the atomic number is, the more the X-rays are attenuated. The attenuation measured in each volume of CT image is the linear coefficient, thereafter, the monoenergetic beam attenuation in a homogeneous material can be calculated through Beer's law (Kak and Slaney 2001) as follows:

$$I = I_0 e^{-\mu x} \quad (3),$$

where I_0 is the initial X-ray intensity, I/I_0 is the attenuation of X-ray intensity per unit length of a given material; μ is the linear attenuation coefficient for the material being scanned and x is the length of the X-ray path through the material. For a composite material the equation (3) becomes:

$$I = I_0 e^{-\sum_i \mu_i x_i} \quad (4).$$

Most reconstruction strategies solve for equation (4) insofar, as they assign a simple value to each voxel rather than some energy dependent range (Ketcham & Carlson 2001). The attenuation coefficients in a CT image are expressed in Hounsfield Unit (HU), which quantifies the amount of attenuation of any specified tissue relative to the attenuation of water. In general, changes in X-ray photon energy will also result in a change in the tissue HU value. Finally, the attenuated X-ray intensities are transferred to a computer for 3D image reconstruction using the 2D projections.

7.1.8 X-ray source

X-rays are a type of electromagnetic radiation with a very high frequency and energy. In the X-ray tube a cathode filament is heated, which ejects electrons by a process called thermionic emission. By applying an electric field, the fast-moving electrons are targeted on an anode. The kinetic energy created from the collision of the electrons with that anode creates for 99 %

thermal energy and less than 1 % is responsible for X- ray production. X-rays are created by two different processes, the first are created by the retardation of electrons, when they interact with the anode and are called Bremsstrahlung or deceleration radiation, which is polychromatic. The second type of radiation comes from the creation of characteristic X-rays (Cnudde 2005). The important variables that determine how effective an X-ray source will be for a particular task is the size of the focal spot, the spectrum of X-ray energies generated, and the X-ray intensity (Ketcham & Carlson 2001). The focal-spot size partially defines the potential spatial resolution of a CT system by determining the number of possible source–detector paths that can intersect a given point in the object being scanned. The more source–detector paths are, the more blurring of features will be (Ketcham & Carlson 2001). The energy spectrum defines the penetrative ability of the X-rays, as well as their expected relative attenuation as they pass through materials of different density. Higher-energy X-rays penetrate more effectively than lower-energy ones, but are less sensitive to changes in material density and composition (Ketcham & Carlson 2001). The X-ray intensity directly affects the signal-to-noise ratio and thus image clarity. Higher intensities improve the underlying counting statistics, but often require a larger focal spot. The energy spectrum generated is usually described in terms of the peak X-ray energy (keV or MeV), but actually consists of a continuum, in which the level with maximum intensity is typically less than half of the peak (Wellington 1987). Figure 21 shows the theoretical energy spectra after Wellington (1987).

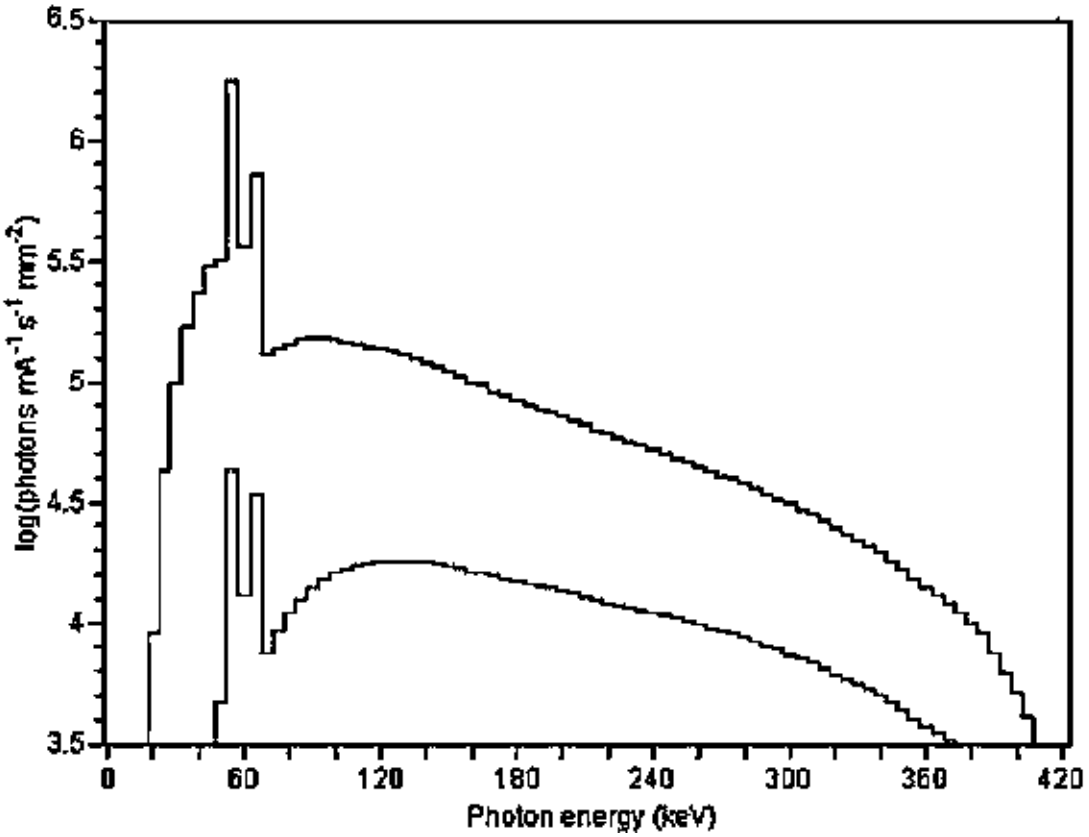

Figure 21 *Theoretical energy spectra for 420-KV X-ray source with tungsten, calculated combining 5-Kev interval spectra consist of continuous Bremsstrahlung and characteristic K-series peaks at 57-59 and 67-69 Kev. Upper spectrum is modified only by inherent beam filtration by 3 mm of aluminum at tube exit port. Mean X-ray energy is 114 Kev. Lower curve represents a spectrum that has also passed through 5 cm quartz. Preferentinal attenuation of low energy X-rays causes' average energy to rise to 178 Kev. After Wellington et al. (1987).*

7.1.9 Detectors

Detectors are made of scintillators to gather the attenuated X-rays. A scintillator converts the incoming X-ray into flashes of light which on their turn are being counted. Detectors influence image quality through their size and quantity, and through their efficiency in detecting the energy spectrum generated by the source. The size of a single detector determines how much energy will be averaged for an amount of object into a single intensity range. While, the number of detectors will determine how much information will be captured at the same time. Moreover,

the level of X-ray energy influences which kind of detector must be used. YXLON FF35 uses a 43 x 43 cm² CsI scintillator flat panel detector Optimized for microfocus CT applications.

7.2 Generation of Pore Network Model (PNM)

Our rock sample were provided from the Hungarian oil company Mol Group. The samples were scanned by the YXLON FF35 CT industrial micro-CT at the University of Miskolc. As mentioned earlier, the cores were taken from an oil and gas well drilled in south west part of Hungary. The choice of the cores was made based on reading the well logs and learning the production profiles to identify the productive and dry intervals of the wells. Tiny plugs were drilled out from larger cores. The goal is to conduct a comprehensive study in pore space images and the derived pore network to establish a process for analyzing pore space using CT tomograms, define the appropriate sample size, the scanning parameter, and the most effective segmentation technique to create acceptable thresholding values. The second goal is to identify, on a micro scale, the distinctions between the four examined core intervals.

7.2.1 Segmentation/Binarization

An X-ray computed tomography (XCT) images, also known as tomograms, consist of a cubic array of reconstructed linear X-ray attenuation coefficient values (also known as pixel values). Accurate image segmentation is the first step toward pore-network modeling and analysis (Gonzalez 2008). Image segmentation is the process of classifying similar values of image gray intensity into distinct groups or classes using machine learning (unsupervised or supervised) segmentation algorithm. The literature reports a variety of techniques for image segmentation (Haralick 1992, Pal 1993, Sezgin 2004), yet none of which is universal and suitable for all types of images.

Porous materials such as carbonates contain areas of void, called the pore space, as well as a number of distinct mineral components, each with a comparatively uniform density consequently similar gray value. Acquiring a clear distribution separating the pore phase from the mineral phase has some difficulties. These difficulties arise from low density pore inclusions (e.g., microporosity, clays) below the image resolution making the distinctions between phases unclear.

There have been intensive studies to improve segmentation methods for better quantitative characterization of pore space feature. Iassonov et al. (2009) broadly classified segmentation algorithms into globally and locally adaptive segmentation. The fundamental concept behind global thresholding scheme is that a single gray value is selected as threshold value separating one phase from the other. There are many subcategories under the scheme, the most commonly used is the histogram shape (triangulation) (Zack et al. 1977). Whereas, in adaptive thresholding each individual pixel is assigned to a particular class based on the information contained on the neighboring pixels. Utilization of local information helps in reducing the effects of some image artifact such as beam hardening. One repeatedly used method is the probabilistic fuzzy c-means (Zack et al. 1977) it belongs to the unsupervised segmentation category but it requires high computational power. In other work Cortina-Januchs et al. (2011) a combination of different algorithms used where they applied clustering and artificial neural network (ANN) to segment binary soil images. Whereas, (Khan et al. 2016) used the supervised technique least square support vector machine (LS- SVM) for segmentation of rock images. The Machine learning and neural networks were developed to mimic human sight and were initially used for speech and image recognition (Fukushima 1980, Lecun 2015). They were rapidly used for the resolution enhancement, for example, satellite images (Chang 2019) and medical images (Pham 2019) and industrial computed tomography XCT (You 2019). Unsupervised learning is a machine learning technique, where there is no need to supervise the model. Instead, the model is allowed to work on its own to discover information. It mainly deals with the unlabeled data and no prior knowledge about the data set is required.

Supervised learning allows to collect data or produce a data output from the previous experience. It helps to optimize performance criteria using experience. A supervised learning model uses training data to learn a link between the input and the outputs. This link is used to sort out information similar to the training data from an unknown data set. Several algorithms can be used in the supervised approaches (e.g. Support vector machine, Neural network, Linear and Logistics Regression, Random forest, Classification trees, and Naive Bayes). The classification and interpretation tasks determine which of the many available segmentation routines should be used (Chauhan 2016).

In this chapter the details of the segmentation algorithm will be presented. First, I introduce the basic concepts of the unsupervised methods used in this algorithm. They are the basic building blocks for training the unsupervised ML algorithms. Then, the Naïve Bayes classifier is proposed for training in which the feature vectors resulted from each unsupervised learning classifier will be used individually for training the Naive Bayes. For evaluating the accuracy of the segmentation results resulted from each training method, the 10 k-fold cross validation technique was used schematic illustration of the segmentation workflow presented in Figure 22. Finally, I compare the results by visual inspection and by feature extraction in terms of pore volume, and pore diameter.

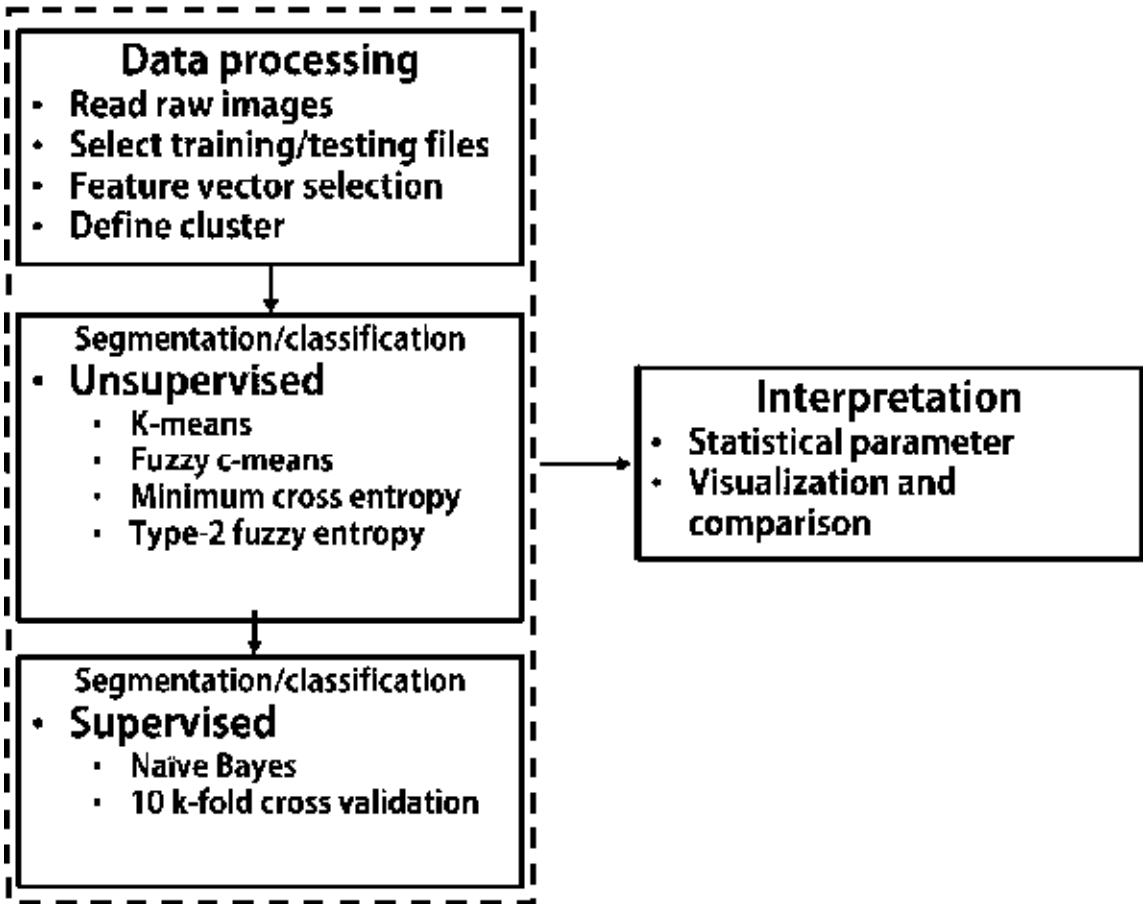

Figure 22 *Schematic illustration of the segmentation workflow applied (edited by H.A.).*

7.2.1.1 Unsupervised pixel classification

7.2.1.1.1 k-means clustering

Cluster analysis is the concept used to recognize observed data into a meaningful structure by discovering the natural grouping(s) of a set of patterns, points or objects, to gain further insight from them. In such a structure, the similarities between objects in the same group are high while the similarities between objects in different groups are low. Hierarchical clustering is a method of cluster analysis where the algorithm builds a hierarchy of clusters either in agglomerative or divisive mode. In the cases of partitional clustering algorithms, the algorithms find all the clusters simultaneously, as a partition of the data, and do not impose a hierarchical structure. The most popular and simplest partitional algorithm is *K*-means clustering (Jain 2010). It is a simple unsupervised learning procedure. The calculation consists of two separate phases. The first phase is for the initializing *K* centroids. In the second phase, each data point is assigned to its closest centroid. The initial centroids are iteratively updated to the mean of the constituent data points. The algorithm finally converges when no further change occurs in the assignment of data points to the centroids. In this state, the points in any cluster have a minimum distance to the corresponding centroid. Several methods can be used to define the distance of the nearest centroid. Among them, Euclidean distance is one of the most used approaches.

7.2.1.1.2 Fuzzy c-means clustering (FCM)

FCM is superior to hard clustering as it has more tolerance to ambiguity and retains more original image information (Lei 2018). The concept of characterizing an individual points similarity to all the clusters was introduced by Zadeh (1965). Zadeh's idea is to depict the similarity a point shares with each cluster by a membership function. Additionally, the sum of the memberships for each sample point must be unity. Each sample will have a membership in every cluster. Memberships close to zero imply a little similarity between the sample and that cluster. The net effect of such a function for clustering is to produce fuzzy c-partitions of a given data set Zadeh (1965). FCM value uses an iterative optimization of an objective function based on a membership function (Toz 2019). A local extremum of this objective function indicates an optimal clustering of the input data (Andrzeij 2007).

FCM has been used in image segmentation (Lei 2018) and it proved efficacy for images with simple texture and background (Lei 2018). Nonetheless, it fails to segment images with complex

texture and background or images corrupted by noise because it only considers gray-level information without considering the spatial information (Lei 2018). To resolve the problem, one popular idea is to incorporate the local spatial information in an objective function to improve the segmentation effect (Lei 2018). Tao Lei et al. (2018) have an improved FCM algorithm based on morphological reconstruction, and membership filtering (FRFCM). By introducing a morphological reconstruction operation, the algorithm manifests tolerance to the noise presented in the image. Consequently, image details are preserved. In the next step the membership partition is replaced by membership filtering that depends only on the spatial neighbors of the membership partition (Lei 2018). The FRFCM algorithm can be summarized as follows:

Step 1: Set the cluster prototype value, fuzzification parameter, the size of the filtering window, and the minimal error threshold.

Step 2: Compute the new image and then compute the histogram of that image.

Step 3: Initialize randomly the membership partition matrix.

Step 4: Update the clustering centers.

Step 5: Update the membership partition matrix.

7.2.1.1.3 Thresholding by minimum cross entropy:

Entropy is a thermodynamic quantity used in physics; it was introduced by German physicist Rudolf Clausius in the second half of the 18th century. It measures the disorder of a system and the spontaneous dispersal of energy as a function of temperature. In physics, the notion of entropy is typically regarded as a measure of the degree of randomness, and the tendency of physical systems to become less and less organized. In 1870, Gibbs gave a general entropy expression for a thermodynamic system as:

$$S = \sum_j P_j log P_j \quad (5),$$

where Pj is the probability that the system is at state j. In 1877, Boltzmann quantifies entropy of an equilibrium thermodynamic system as:

$$S = K \cdot logW, \quad (6),$$

where S is entropy; K is Boltzman constant and W is the number of states in the system.

In 1949, Shannon redefined the entropy concept of Boltzmann/Gibbs as a measure of uncertainty regarding the information content of a system (Sengur 2006). In information theory,

entropy measures the amount of uncertainty of an unknown or random quantity (Mahmoudi 2012). Many entropy-based thresholding methods exist in the literature. These methods can be categorized into three groups: entropic thresholding, cross-entropic thresholding, and fuzzy entropic thresholding (Mahmoudi 2012). Cross-entropic thresholding formulates the thresholding as the minimization of an information-theoretic distance (Sezgin 2004). Entropy could also be used as a measure of separation that separates the information into two regions, above and below an intensity threshold (Al-Attas 2006). Entropic thresholding considers the image foreground and background as two different signal sources so that when the sum of the two-class entropies reaches its maximum, the image is said to be optimally thresholded (Sezgin 2004). When the minimum cross-entropy criterion is applied to threshold segmentation, it refers to searching the threshold which can minimize the information content before and after segmentation.

The simplest and most direct scheme for threshold selection would be to iterate through all possible threshold values and to select that threshold, which corresponds to the minimum of the cross entropic.

7.2.1.1.4 Type-2 fuzzy entropy thresholding:

A classical set A can be defined as a collection of elements that can be either belong to or not belong to set A. In contrast, a fuzzy set is a collection of objects without clear boundaries or well-defined characteristics. There are two types of fuzzy sets. A type-1 fuzzy set A, in a finite set, X = {x1, x2, …, xn} may be represented as in equation (7):

$$A = \{x, \mu_A(x) \mid x \in X, 0 \leq \mu_A(x) \leq 1\} \quad (7),$$

where $0 \leq \mu_A(x) \leq 1$and $\mu_A(x)$ is called the membership function, which measures the closeness of x to A and it can only take a single value.

In a Type-2 fuzzy set, a range of membership values is used instead of a single value. If A is a type-2 fuzzy set, then:

$$A = \left\{x, \mu_A^{High}(x), \mu_A^{Low}(x) | x \in X, 0 \leq \mu_A^{High}(x), \mu_A^{Low}(x) \leq 1\right\} \quad (8).$$

In the above definition, μ_A^{High} , and μ_A^{Low} are upper and lower membership functions, respectively.

A digital image, I_{Gr} contains M × N pixels, where each pixel has a position defined by (m; n). The images have L intensity values that are stored in the pixels. In this context, the distribution of the intensity levels on the image can be represented by a histogram that can also be normalized as:

$$h_i = \frac{np_i}{(NP)},\ \sum_{i=1}^{NP} h_i = 1 \quad (9),$$

where i is a level of intensity ($0 \leq i \leq L-1$) and $NP = M \cdot N$ is the total number of pixels contained in the image. The term ultra-fuzziness can be used as a metric associated with a fuzzy set. It gives a 0 value when the membership values can be represented without an uncertainty. However, the value rises to 1 when membership values can be specified within an interval. For a digital image, the ultra-fuzziness for the i [th] level of intensity is defined as:

$$P_k = \sum_{i=0}^{L-1}(h_i * (\mu_k^{high}(i) - \mu_k^{low}(i))),\ K = \{1,2,\dots,nl\}$$

(10).

Fuzzy entropy measure is a concept used to assess the amount of vagueness within a fuzzy set. The type II fuzzy entropy for a k^{th} −threshold is therefore given as:

$$Fe_k = -\sum_{i=1}^{L-1}\left(\frac{(h_i*(\mu_k^{high}(i)-\mu_k^{low}(i))}{P_k}\right) * in\left(\frac{(h_i*(\mu_k^{high}(i)-\mu_k^{low}(i))}{P_k}\right),\ K = \{1,2,\dots,nl\}$$

(11).

The sum of all the entropies for the (nl + 1) levels is the total entropy defined as:

$$T_{Fe}(a_1, c_1, \dots, a_n, c_n) = \sum_{k=1}^{nt+1} Fe_i \quad (12)$$

7.2.1.2 Supervised clustering: Naive Bayes classifier

In supervised learning classifier only labeled data (training patterns with known category labels) are involved. A supervised classifier is trained using a set of predefined features or classes (known as training data), where similar pixels values are sorted out from unknow data set (testing data) using supervised learning techniques. The performance of this classifier on the testing subsets(s) indicates the stability of the clustering algorithm.

Treating image properties as random variables, and deriving a probabilistic model based on Bayesian image segmentation. The motivation for the application of a stochastic framework is

based on the assumption that the variation and interactions between image attributes can be described by probability distributions (Dong-Chul 2016). Naïve Bayes classifier is based on Bayes' theorem (Jang 2016). The Bayes' theorem says, that the probability that an event x belongs to a class k can be calculated by using the following equation:

$$P(c_k|x)=\frac{P(x|c_k)P(c_k)}{P(x)} \quad (13)$$

In the equation (13); $P(c_k|x)$ is a posterior probability, $P(x|c_k)$ is the probability of x occurring given evidence c_k has already occurred, P (c_k) is the Probability of c_k occurring, P(x) is the probability of x occurring. Based on the Bayesian decision we can decide the optimum class k for the event x by choosing the class with the highest probability among all possible classes. This choice can minimize the classification error (Dong-Chul 2016). For doing so, we need to estimate $P(x|c_k)$ providing that any particular value of vector x conditional on c_k is statistically independent of each dimension (Dong-Chul 2016).

$$P(x|c_k) = \prod_{i=0}^{n} P(x_i|c_k) \quad (14)$$

where x is a n-dimensional vector.

The Naïve Bayes classifier can then be calculated as:

$$K = \text{argmax}_k \, p(c_k) \prod_{i=0}^{n} P(x_i|c_k) \quad (15)$$

7.2.1.3 Metrics of evaluation and accuracy assessment

In classification problem there are several evaluation metrics to assist the classification accuracy. These metrics can be described as follows:

K-fold cross validation: the idea for cross-validation was first proposed by Larson (1931). Cross validation is a statistical method of evaluating and comparing learning algorithms. It divides the data set into two subsets: one is used to learn or train a model and the other is used to validate the model. The problem in such a model that it may demonstrate adequate prediction capability on the training data, but it might fail to predict future unseen data (Chauhan 2016). There are several approaches to estimate the accuracy of classifier using different combinations of k-fold cross- validation techniques. Kohavi (1995) and Dietterich (1998) recommended 10-fold cross-validations as one of the best cross-validation techniques, as it mitigates biases despite variances

in the size of training and testing datasets. At the onset of 10-fold cross-validations, the dataset is initially stratified and partitioned into 10 equal (or nearly equal) subsets or folds. Subsequently, 10 iterations of training and validation are performed such that, within each iteration, a different fold of the data is held out for validation, while the rest of the folds are used for learning. A schematic illustration of the workflow of l0 k cross-validations in conjunction with Naïve Bayes is shown in Figure 23.

The evaluation metrics can be summarized briefly as follows; Precision: is the proportion of positive cases that were correctly identified. The precision is the ratio tp /tp + tf where tp is the number of true positives (positive cases that were correctly identified) and fp is the number of false positives (negative cases identified as, positive). Recall: Is the proportion of actual positive cases which are correctly identified. F1: is the harmonic mean of precision and recall values for a classification problem. Area under ROC curve: the ROC (Receiver operating characteristic) curve is the plot between sensitivity and (1- specificity). (1- specificity) is also known as false positive rate and sensitivity is also known as True Positive rate. To bring this curve down to a single number, we find the area under this curve (AUC). Classification accuracy CA: which measures the number of correct predictions made divided by the total number of predictions made.

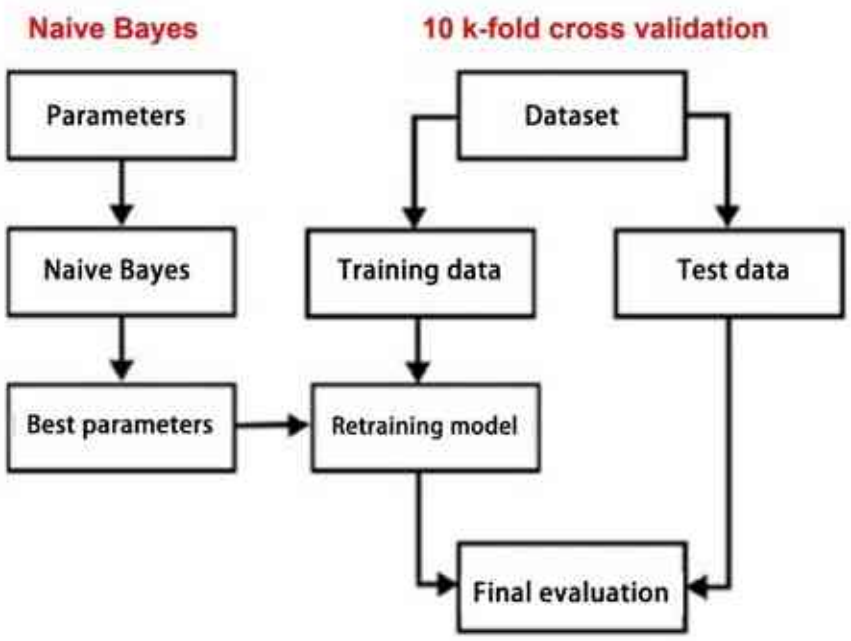

Figure 23 *Schematic illustration of supervised machine learning algorithm using Naïve Bayes and k-fold cross validation in the left side are the parameters resulting from Naïve Bayes classifier, and in the right side the data trained and tested, and the final evaluation is done using 10 k-fold cross validation (edited by H.A.).*

7.2.2 Building PNM using hybrid method

I mainly used the software Avizo® to extract pore networks from digital images and analyze the pore properties of four carbonate rock samples. The reason I used Avizo software is because it is a specialized software that offers advanced capabilities for extracting pore networks from digital images and analyzing pore properties in rock samples. It provides the necessary tools and functionalities for this specific research task, enabling more accurate and comprehensive analysis. The algorithm of Avizo® is a hybrid algorithm proposed by Pudney (1996, 1998). This hybrid algorithm is called the Distance Ordered Homotopic Thinning (DOHT) method. It uses the distance map algorithm to compute the shortest distance of each point from void space to the background using Chamfer methods. Then the thinning algorithm is applied to get the skeletonization of the pore space and retain the topology guided by the distance map. In this approach the distance map marks each point of the skeleton with the minimum distance to the boundary of the space. The workflow of the hybrid method is illustrated by Youssef et al.

(2007). As in Figure 24 where the channels are described by a single line and pores are represented by a group of lines and vertices. The algorithm is conducted in three main steps. The first step is to identify the channel lines based on the skeleton of the pore space (Figure 24a). Meanwhile, the identification and calculation of the connectivity number and the length for each line are determined, leading to the identification of the pore space tortuosity (Figure 24b). Each line is represented by a set of connected voxels and the connectives of a line are equal to the connectivity of its two ends voxels. The second step is to partition the skeleton into a group of lines belonging to the same pore (Figure 24c). Finally, in the third step, the geometrical separation and labeling of pores are done by adding the binary image of the void space to the labeled cluster image (Figure 24d). Then comes a voxel growth constrained algorithm. This pore network extraction method maintains the advantages of the medial axis and watershed algorithm, i.e. retaining the topology of void space. Based on the above algorithms, this hybrid algorithm can determine pore connectivity and tortuosity. A subsample was extracted in the middle part of the 2mm sample at 680 x 660 x 1000 volume for the four samples as illustrated in Figure 25. Figure 26 presents the pore network model extracted using the aforementioned algorithms.

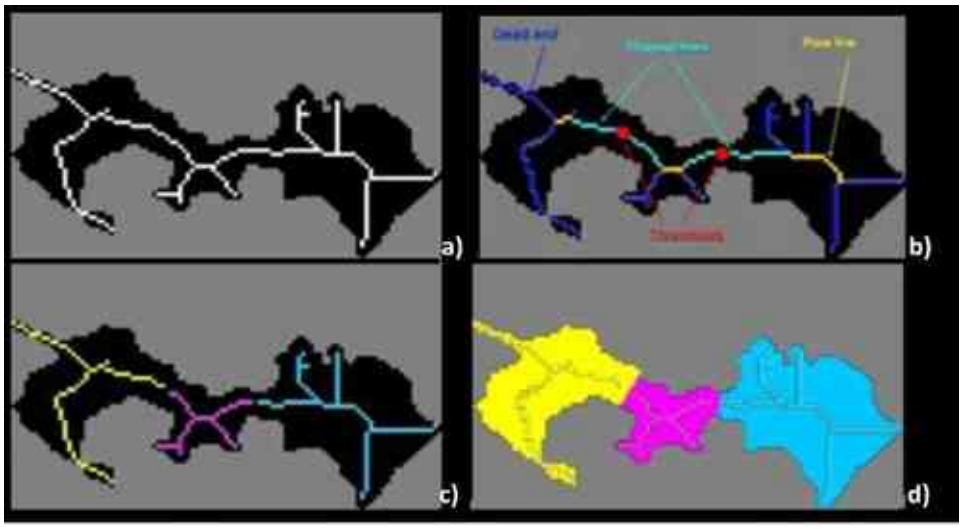

Figure 24 *Schematic illustration of the workflow of the Distance Ordered Homotopic Thinning algorithm where: a) Initial skeleton of the pore space b) Identifying channel lines (light blue), pore lines (yellow) and dead ends (dark blue), (c) Identifying thresholds in the channels lines (minimum diameter) and labeled pore segments, (d) Reconstruction of labeled pores for pore volume estimation. Youssef et al. (2007).*

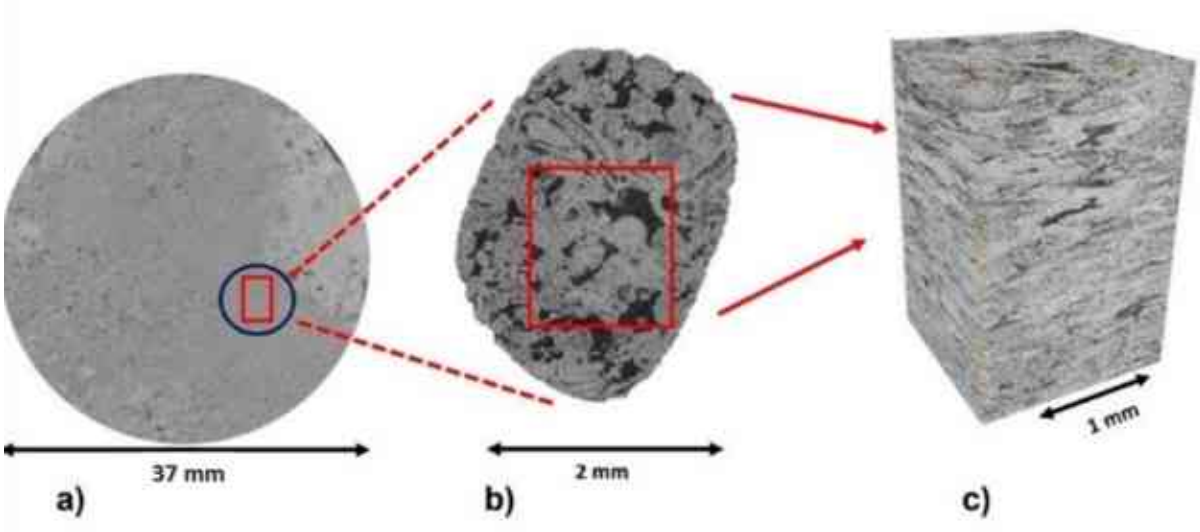

Figure 25 *Micro-CT image of Sample 1966: a) 2D slice of the 26 mm plug with a resolution of 20 microns; b) 2D slice of the 2 mm plug with a resolution of 2 microns; c) 3D view of the extracted volume (edited by H.A.).*

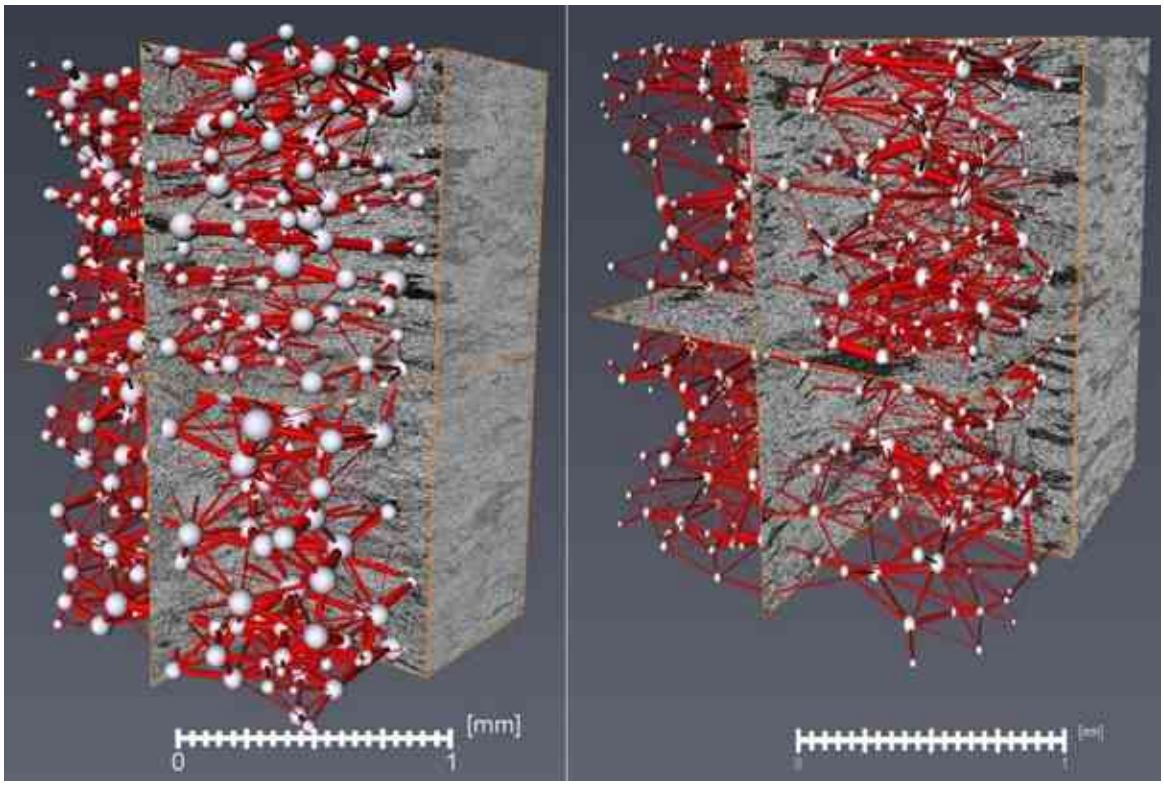

Figure 26 *3D pore network representation with the corresponding assigned radii for the two samples.1966 to the left and 1967 to the right (edited by H.A.).*

7.3 Transport properties

7.3.1 Image derived permeability

Absolute permeability is defined as the measurement of the capacity of a porous material to transmit a single-phase fluid. Its SI equivalent is the square meter however square micrometer is more common since it almost equivalent to one Darcy (d) = 0.9869233 µm

Absolute permeability appears in Darcy's law see (Darcy, 1856) as a constant coefficient relating fluid, flow and material parameters:

$$\frac{Q}{S} = \frac{K}{\mu}\frac{\Delta P}{L}$$

(16),

where Q is the global flow rate that goes through the porous medium (unit: $m^3 .s^{-1}$), S is the cross section of the sample which the fluid goes through (unit: m^2), K is the absolute permeability (unit: m^2), µ is the dynamic viscosity of the flowing fluid (unit: Pa.s), ΔP is the pressure difference applied around the sample, L is the length of the sample in the flow direction (unit: m).

The permeability simulation is conducted using Avizo software with input of the binary images resulted from our classification scheme (with isolated pores excluded). To numerically estimate the absolute permeability the Stokes equation was solved based on a finite-volume method which builds the volume mesh directly on the voxels of the 3D pore data (Zhang et al. 2012):

$$\nabla . u = 0 \; ; \; \nabla p = \mu \nabla^2 u \qquad (17)$$

Where u is the fluid viscosity vector, p is the pressure, µ is the dynamic viscosity. Permeability is then evaluated by the Darcy's law. The Avizo XLab-Hydro solver has been validated by comparing to theoretical models and standard glass bead packaging models (Zhang et al. 2011). The equations system is a simplification of the Navier-Stokes:

-an incompressible fluid, which means that its density is constant;

-a Newtonian fluid, which means that its dynamic viscosity is a constant;

-a steady-state flow, which means that velocity does not vary over time;

-a laminar flow, which means that the concerned velocities are small enough not to produce turbulence.

The last point is equivalent to considering flow at a low Reynolds number see (Reynolds, 1883). Once this equation system is solved, estimating the permeability coefficient consists of applying Darcy's law.

The experiment simulation in Avizo software is based on Stokes equations resolution; this is done in Absolute Permeability Experiment Simulation module. The boundary conditions are specified as:

- A no-slip condition at fluid-solid interfaces.

- One-voxel-wide plane of solid phase (with no-slip condition) is added on the faces of the image that are not perpendicular to the main flow direction. This allows isolation of the sample from the outside, allowing no flow out of the system.

- Experimental setups are added on the faces of the image that are perpendicular to the main flow direction. They are designed in a manner that creates a stabilization zone where pressure is quasi static, and the fluid can freely spread on the input face of the sample.

- Two among the following three conditions can be chosen by the user, the third being estimated from the chosen two: input pressure, output pressure, flow rate.

For the simulation experiment representative sub-region of the sample was selected as shown in Figure 27.

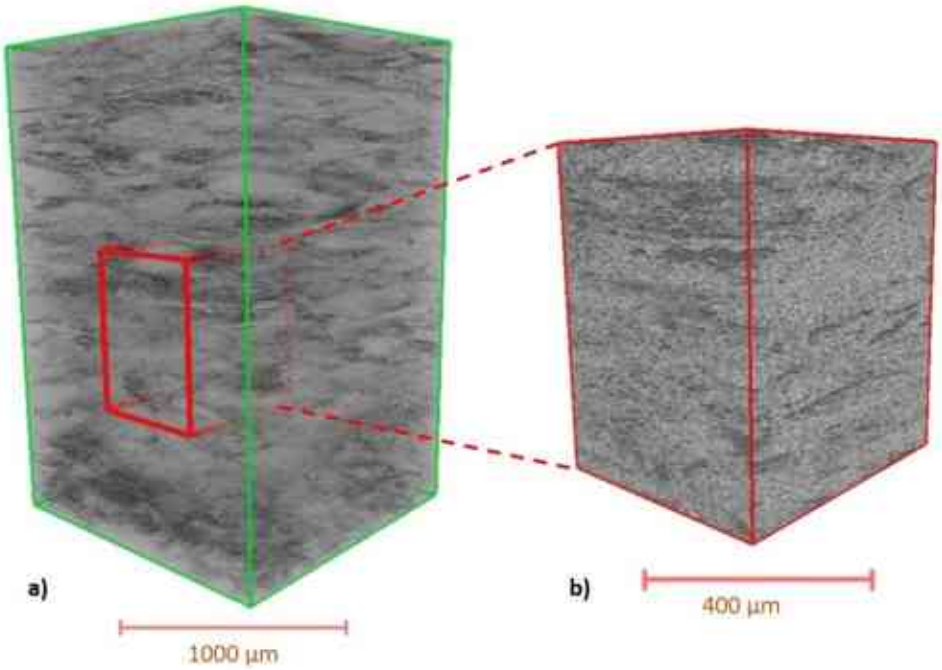

Figure 27 *Selecting a region of interest (ROI) for permeability simulation a) is the examined sample and, b) is the region of interest (edited by H.A.).*

7.3.2 Bulk sample laboratory measurement of permeability

A cylendrical core (3.7 cm diameter, 7 cm height) from the rock samples was used for the bulk sample measurement to compare with the results from image analysis and simulations. The permeability were measured by core laboratory at Miskolc (AFKI) according to the standard methods. Where different flow rates throughout the sample are adjusted, and the corresponding Δp values are determined. From the resulting value pairs, the Klinkenberg effect was corrected to derive the permeability (Klinkenberg, 1941).

In table 1 the Lab and image derived permeabilities are compared for all four samples.

Table 1 *Comparing lab measured permeability against image derived permeability*

Sample ID	Sample dimensions		Permeability	
	LAB	µ-XCT	Lab	µ-XCT
1966	33 mm diameter × 70 mm height	0.598 mm × 0.530 mm × 0.560 mm	33.1 mD	190 mD
1967	33 mm diameter × 70 mm height	0.392 mm × 0.542 mm × 0.514 mm	54.32 mD	880 mD
1979	37 mm diameter × 70 mm height	0.456 mm × 0.385 mm × 0.450 mm	0.0721 mD	-
1980	37 mm diameter × 70 mm height	530 mm × 490 mm × 510 mm	0.0037 mD	-

In the dry interval samples (1979 and 1980) both exhibited notably low permeability as measured in the laboratory. Additionally, the micro - XCT images did not reveal any discernible connections between the pores in these samples. In the productive interval samples (1966 and 1967) both networks over-predict permeability. The purpose of the permeability laboratory experiment was to validate µ-XCT results, and provide a comprehensive understanding of the rock samples. Regarding the difference in magnitude between laboratory permeability measurements and µ-XCT results, this can be explained by several factors:

-Scale Differences: Laboratory permeability measurements are typically conducted at a larger scale, involving larger sample volumes and longer flow paths. µ-XCT, on the other hand,

operates at a microscopic scale, where it captures the behavior of individual pores and their connections. The scale difference can lead to variations in the measured permeability values.

-Resolution Limitations: μ-XCT has a limited resolution, and it may not capture the smallest pores and fine-scale heterogeneity present in the rock samples. These small-scale features can contribute significantly to permeability but may not be fully accounted for in the imaging technique.

-Sample Heterogeneity: Rock samples often exhibit heterogeneity in their properties, including permeability. Laboratory measurements can provide an average permeability value for a larger sample, whereas μ-XCT captures variations in permeability at a finer scale. This inherent heterogeneity can contribute to differences in magnitude between the two measurement methods.

-Porosity and Connectivity: The way pores are interconnected within the rock can impact permeability. Laboratory measurements may not capture the full complexity of pore connectivity, whereas μ-XCT can reveal details about pore networks.

8. Results

8.1 Segmentation / binarization accuracy:

The classification process intends to categorize every pixel in a digital image. Each class of pixel is based on a specific feature. The categorized data could then be used to retrieve useful information. In this study, these classes were applied to compute porosity and assist in the calculation of pore size distribution (PSD).

One of the main challenges for the comparison of segmentation algorithms for X-ray images of porous materials is the lack of ground truth. That is the lack of knowledge of the optimal binarization results. Generally, two basic techniques are applied to the objective evaluation of image segmentation: analytical and experimental technique (Sharon 2000).

The analytical technique evaluates an image segmentation algorithm by analyzing the principle of the algorithm. The experimental technique, which is widely used, interprets and compares experiment results of image segmentation algorithms to make an evaluation, and it can be subdivided into two distinct methods: superiority evaluation method and deviation evaluation method (Brink 1992).

The superiority evaluation method evaluates an image segmentation algorithm by utilizing human visual traits (Brink 1992). In the deviation evaluation method, firstly a standard segmentation image is provided for comparison criteria. Then the disparity between actual segmentation and ideal one can be calculated to evaluate the image segmentation algorithm (Brink 1992).

In the experimental technique the different image segmentation algorithms were tested and compared in terms of three criteria: visual comparison, calculated parameters (pore size, pore volume) and pore count. Finally, the results were compared to a ground truth segmented image, where the latter is obtained by manual labeling of the pixels of the tested image based on the visual evaluation. It is worth mentioning that a ground truth image is not necessarily an optimal segmentation since the evaluation of the ground truth image is done visually. Rather an additional datum to assists in making the final decision.

My dataset for training and testing consists of 100 tomograms, with 50 tomograms used for training and another subset of 50 tomograms used for testing. This subset of 100 tomograms was selected to best represent our samples in terms of investigated features.

I created a ground truth images for validation by manual annotation and labeling. To create a training data and to classify the pixels in the images into labeled features representing pores and matrix constituents I used the aforementioned clustering and entropy algorithms on a Matlab environment. All the available features were classified into two groups. Each group has homogeneous features (in my case pores and matrix) and form a feature vector. The resulting features were used to train a Naive Bayes classifier. I calculated the mean and standard deviation of the posterior probabilities for each cluster in the training set and used these values to predict the posterior probability for each testing data point. To test the classifier and to avoid data overfitting, a 10 K-fold cross-validation was implemented. In that process, the data was stratified and divided into 10 folds. One-fold held out for testing and validation, and the other nine were for the training. This process was repeated for each fold iteratively. Our approach was evaluated using various evaluation metrics including under the curve (AUC), classification accuracy (CA), F1 score and precision. The AUC metric provides a measure of the overall quality of the classification, with higher values indicating better performance. The CA metric represents the proportion of correctly classified pixels, while the F1-score is a weighted average of the precision and recall metrics. Precision refers to the proportion of true positive classifications among all positive classifications, while recall measures the proportion of true positive classifications among all actual positive pixels. The classification accuracy resulting from each training was relatively high. It was reasonable since the unidentified threshold value was confined within a limited gray intensity range which was mainly represented by the transition zone lying in between the two phases. Nevertheless, the set of misclassified pixels detected by the supervised machine learning algorithm for each training set varied. In Fuzzy C-Means and Type 2 Fuzzy Entropy, the number of the misclassified pixels was the highest. The reason for that could be attributed to the fact that in fuzzy classification, a single gray value could be a member in more than one group at the same time. In contrast, the Naïve Bayes algorithm does not consider spatial location. Classification accuracy in the Naïve Bayes classifier is listed in Table 2. The resulting binarized images for each segmentation method are shown in Figure 28.

Table 2 *Comparison of classification accuracy on Naïve Bayes classifier with different feature vectors*

Classifier	AUC	CA	F1	Precession	Recall	Misclassified	Misclassified pixels gray range	Naïve Bayes predicted threshold value
K-means	0.965	0.877	0.871	0.897	0.877	156000	85-107	90
Fuzzy c-means	0.967	0.888	0.882	0.904	0.888	403100	85-104	90
Minimum cross entropy	0.974	0.946	0.944	0.95	0.946	96410	85-91	90
Fuzzy entropy	0.984	0.965	0.965	0.967	0.965	180640	85-112	103

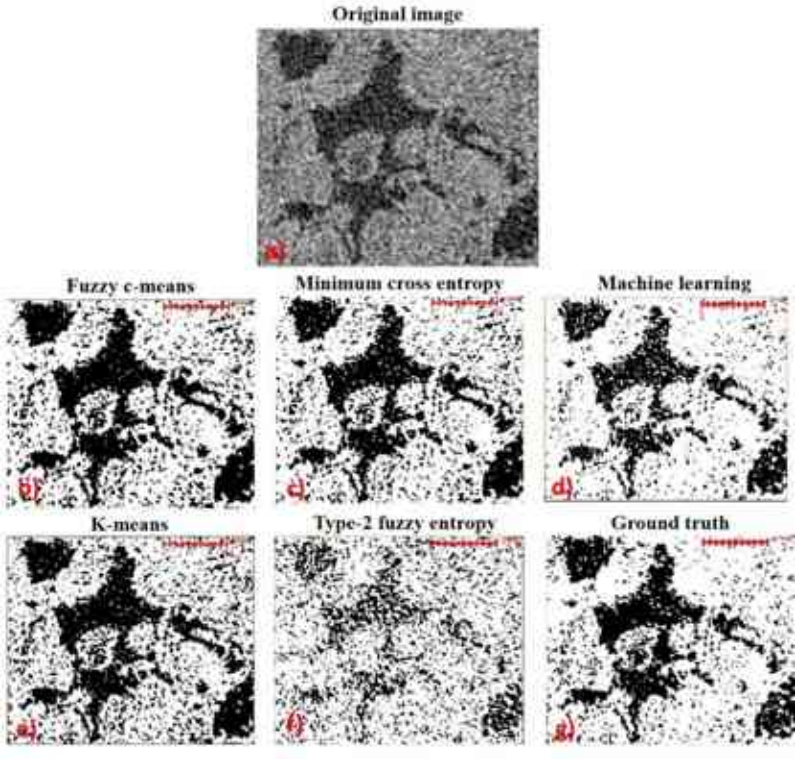

Figure 28 *2-D segmented images and binarized using unsupervised and supervised segmentation where pores appear in black and matrix in white (edited by H.A.)*

8.1.1 Segmentation evaluation

The performance of the unsupervised and supervised classification methods is evaluated in terms of how well they classified the pore shape pixels in the XCT images. The volume fraction and pore counts are shown in Figure 29. The geometrical pore size distribution was calculated from the 8-bit segmented image using Avizo software. The resulting pore size distribution coming from each segmentation method are shown in Figure 30a the calculations of P10, P50, and P90 values percentiles allowed the interpretation of geometrical pore size contribution in terms of macro-pore to the total pore volume (Figure 30b). In figure 30a the shapes of the distributions suggest some grouping possibilities. Seemingly three groups can be defined; 1- T2FE, 2- MINCE and k-Means, 3- Fuzzy c-means, Ground Trouth, and Naive Bayes. Moreover, in Table 3 I compare the results in terms of measured parameters resulting from each segmentation scheme. Additionally, and to clarify the sensitivity of the segmentation process to a certain threshold value, the global thresholding technique was used by selecting different threshold values in the vicinity of the identified or computed ones. The changes in pore counts and average pore radii indicate the thin margin that separates the pore constituent from each other and the background or the matrix constituent. Figure 31 shows a visual illustration of the sensitivity study.

Classifier	Pore count	Pore volume (%)
K-mean	845	38.02
FRFCM	610	37.32
MINCE	796	30.24
T2FE	982	27.17
Naive bayes	680	25.80
Ground truth	564	29.30

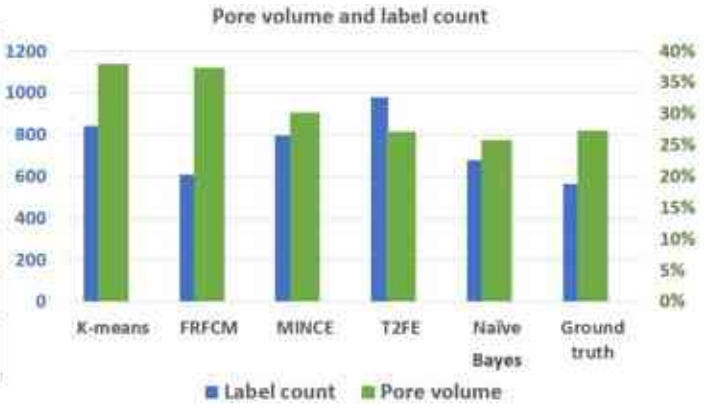

Figure 29 *Porosity values and pore count obtained by using unsupervised and supervised classifiers (edited by H.A.).*

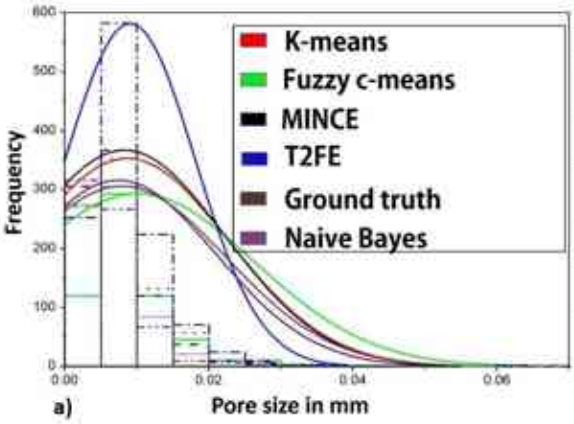

Classifier algorithm	P10 mm	D50 mm	D90 mm
K-means	0.00226	0.00638	0.01514
FRFCM	0.00391	0.00748	0.01596
MINCE	0.00226	0.00597	0.01373
T2FE	0.003909	0.007137	0.01497
Naïve Bayes	0.00226	0.00505	0.01131
Ground truth	0.00391	0.00677	0.01329

b)

Figure 30 *a) Histogram and Normal curve for pore size distribution resulted for each segmentation method for the tested 2-d tomogram b) Pore size diameter obtained for six segmentation algorithms from the same tomogram (edited by H.A.).*

Table 3 *Sensitivity table comparing different threshold values of measured parameters resulting from supervised, unsupervised, and global thresholding*

	Segmentation method	**Threshold value**	**Measured pore volume**	**Average pore radii**	**Pore count**
Supervised and unsupervised segmentation	K-means	108	0.38	0.0088	845
	Fuzzy c-means	-	0.37	0.0103	610
	MINCE	95	0.3024	0.008	796
	T2-FE	127	0.276	0.0117	494
	Naive Bayes	90	0.258	0.0075	756
Global thresholding sensitivity	Global thresholding	85	0.24	0.0073	680
	Global thresholding	92	0.28	0.077	767
	Global thresholding	98	0.32	0.0081	811

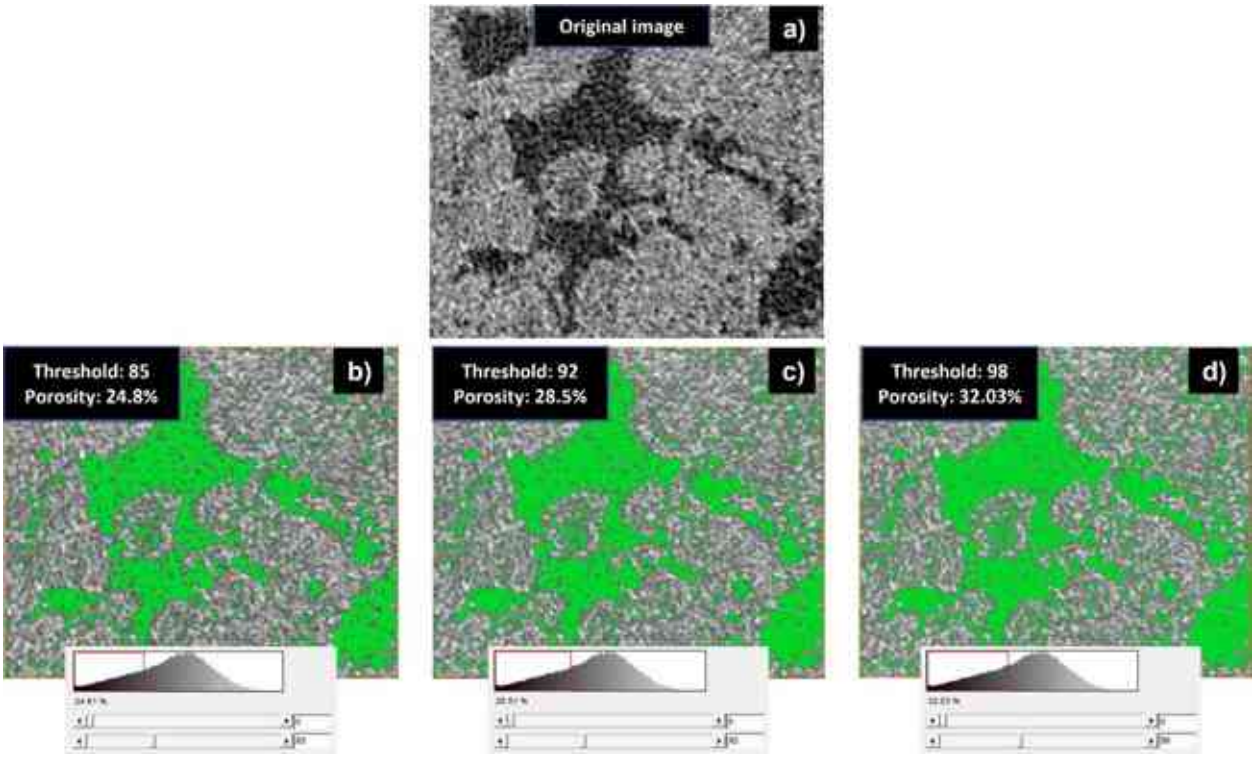

Figure 31 *Global thresholding applied to the original image with different threshold values. The pore is highlighted in green (edited by H.A.).*

8.2 Pore reconstruction and description

8.2.1 Productive interval

Sample 1966: A subsample was extracted in the middle part of the 2mm sample at 680 x 660 x 1000 volume. The porosities were determined from the stack of 1000 XCT slices with a low voxel size at 2 microns. The binarized images resulting from the segmentation scheme were imported to Avizo® software for pore analysis. The average porosity obtained from XCT images is 24%, which is in good agreement with the effective porosity to the gas of 25 % measured by He porosimetry in the lab. The 3D pore distribution and two illustrations of the pores connection on a micron scale are shown in Figure32. For further analysis, (the pore size and throat size distribution Figure 33 and Table 4, channel length Figure 34, and coordination number Figure 35) of the given sample are investigated.

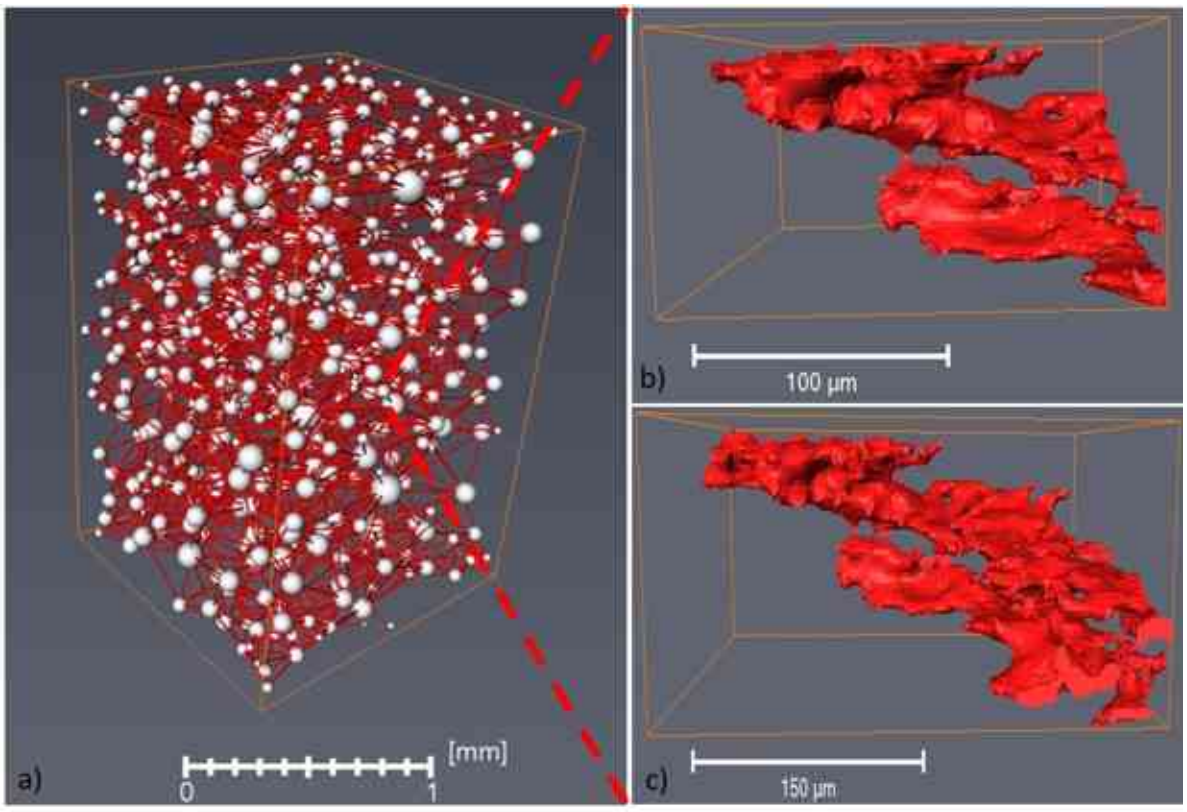

Figure 32 *a) 3D view of the pore network of sample 1966 b) and c) are two illustrations of the pores connection on a micron scale (edited by H.A.).*

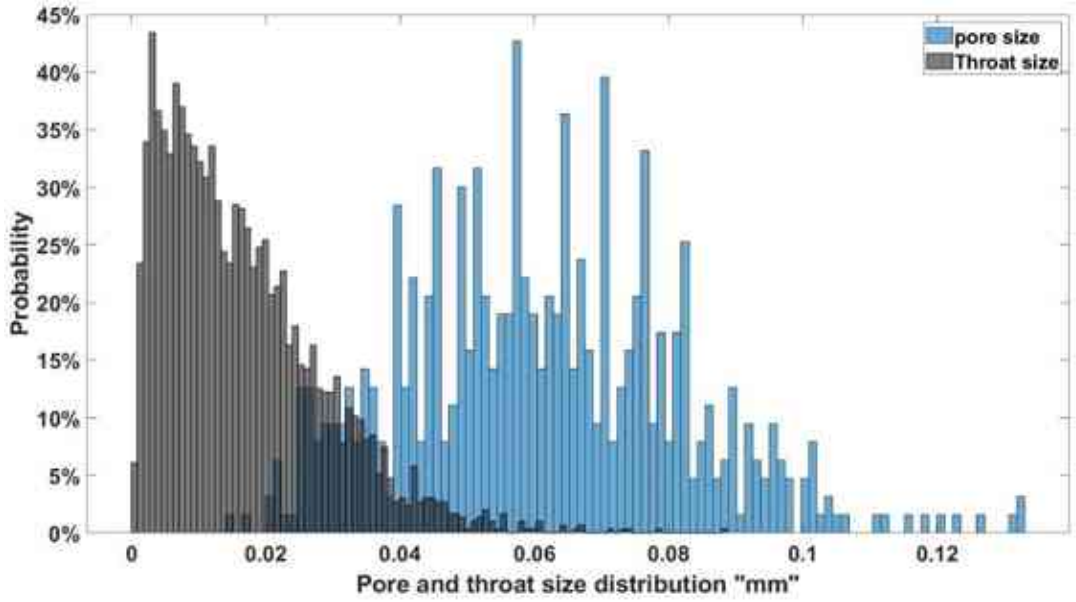

Figure 33 *Sample 1966 pore size and throat size distribution (edited by H.A.).*

Table 4 *sample 1966 Pore volume and pore / throat sizes*

Sample ID: 1966	Count	Total pore volume (%)	Connected pore volume (%)	Average size	Minimum size	Maximum size	Pore radii percentiles		
							D10 mm	D50 mm	D90 mm
1966	Pore: 632	24	22	0.0609	0.014	0.132	0.035	0.06	0.087
	Throat: 2946			0.0164	0.000604	0.0886	0.003	0.014	0.033

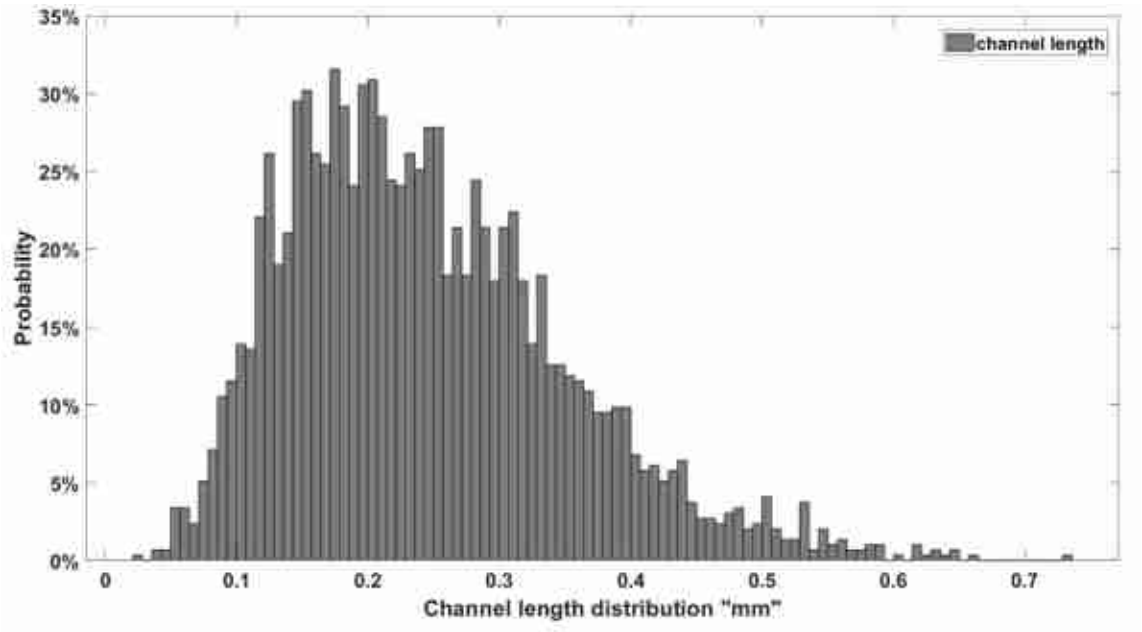

Figure 34 *Sample 1966 channel length distribution (edited by H.A.).*

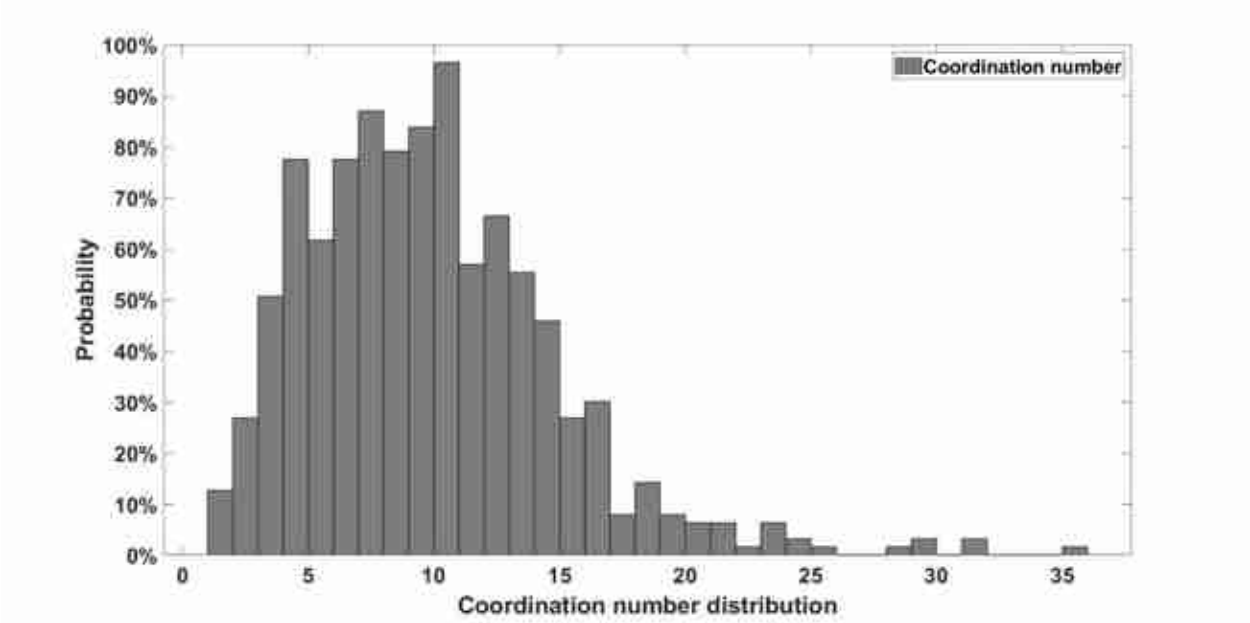

Figure 35 *Sample 1966 coordination number distribution (edited by H.A.).*

The interrelationship between pore throat and pore radii is shown in Figure 36a. The correlation between these two measured parameters is not so clear; still, a correlation is observed between the pores and throats when the throat radii are smaller than 65 microns, which is the most frequent throat size as shown in Figure 36b. Figure. 36a also shows the relationship between pore radii and coordination number; as is expected, the larger the radius, the higher the coordination number.

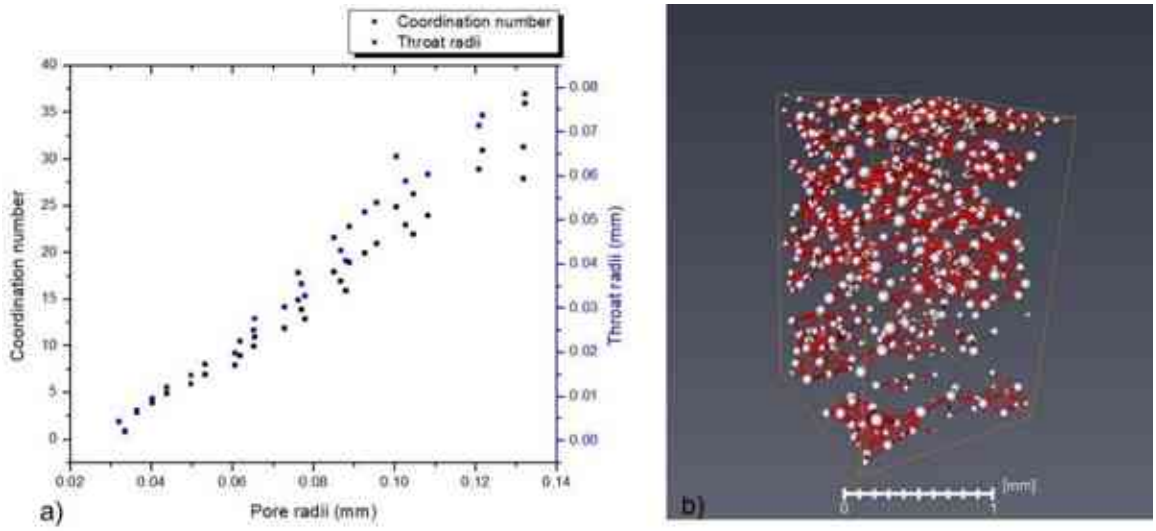

Figure 36 *Pore radius/coordination number and pore radius/throat radius correlations in Sample 1966, b) 3D view of the pore distribution pore sizes smaller than 0.08 mm (edited by H.A.).*

Sample 1967: The subsample was extracted in the middle part of the 2mm sample at 680 x 660 x 800 volume. The porosities were determined from the stack of 800 XCT slices with a low voxel size of 2 microns. The binarized images resulting from the segmentation scheme were imported to Avizo® software for pore analysis. The average porosity obtained from XCT images is 27% which is in good agreement with the effective porosity to the gas of 28.04% measured by the He porosimetry in the lab. 3D pore distribution and an illustration of the connection between pores on a micron scale are shown in Figure 37. For further analysis, the connected porosity (pore and throat size distribution Figure 38 and Table 5, channel length distribution Figure 39, and coordination number Figure 40,) of the given sample are investigated.

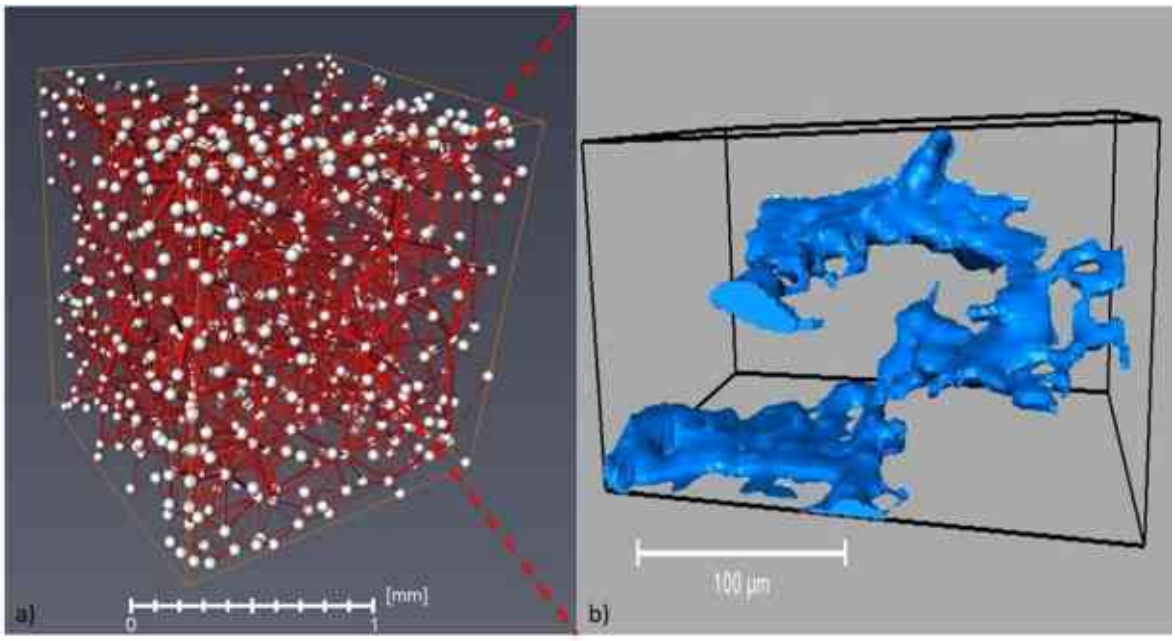

Figure 37 *a) Sample 1967 3D view of the pore network of sample 1967 b) illustration of pore connection on a micron scale (edited by H.A.).*

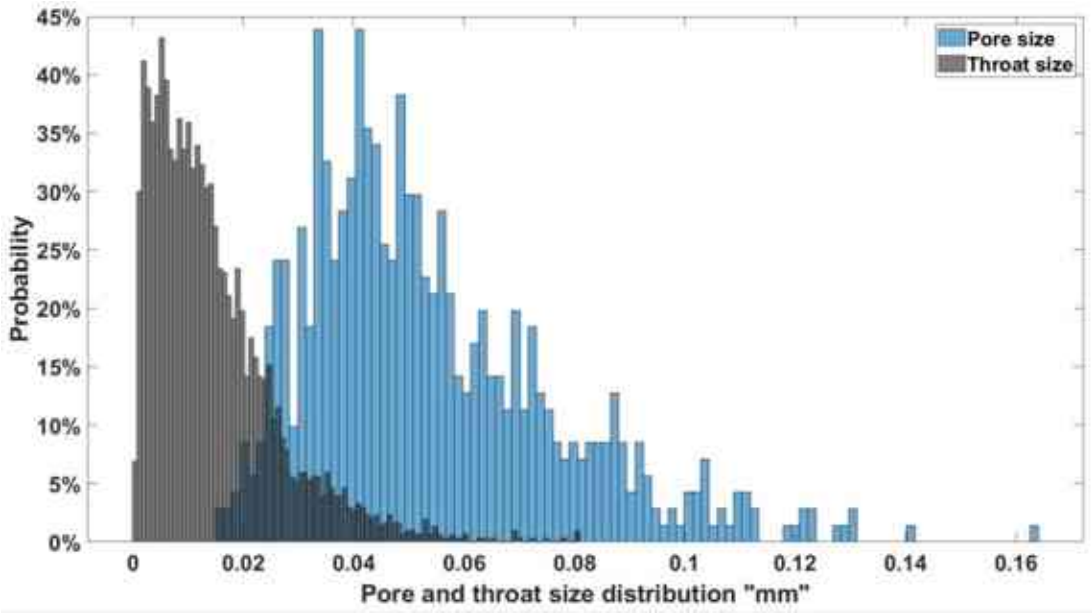

Figure 38 *Sample 1967 pore and throat size distribution (edited by H.A.).*

Table 5 *Pore volume and pore / throat sizes in sample 1967*

Sample ID: 1967	**Count**	**Total pore volume (%)**	**Connected pore volume (%)**	**Average size "mm"**	**Minimum size "mm"**	**Maximum size "mm"**	**Pore radii percentiles**		
							D10 mm	**D50 mm**	**D90 mm**
1967	Pore: 707	27	25	0.0535	0.0152	0.163	0.029	0.049	0.086
	Throat:3035			0.0145	0.000604	0.0809	0.003	0.012	0.03

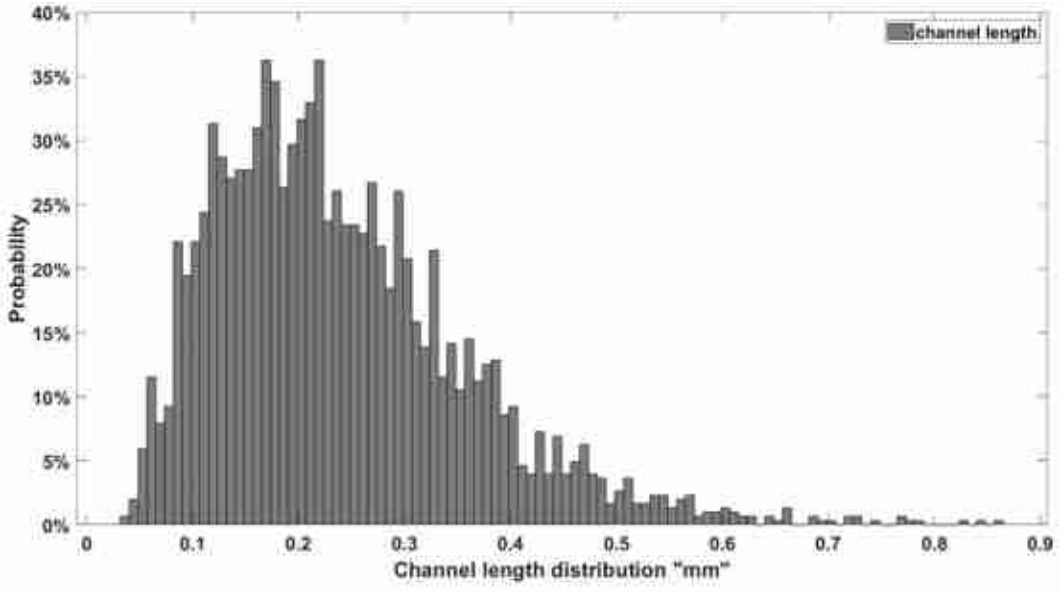

Figure 39 *Sample 1967 channel length distribution (edited by H.A.).*

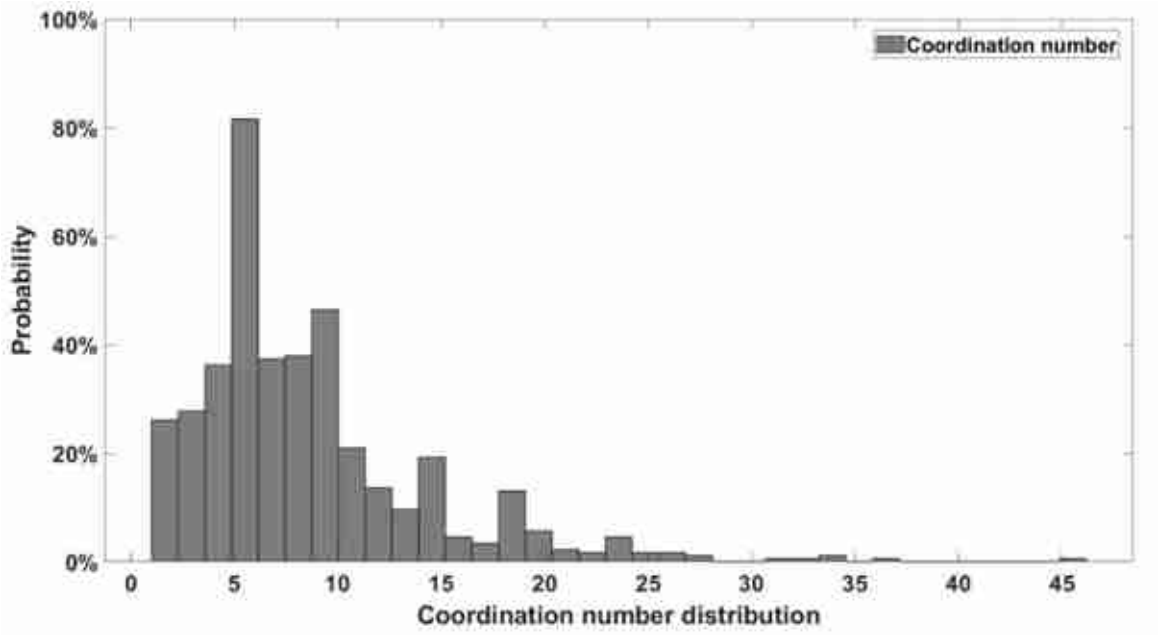

Figure 40 *Sample 1967 coordination number distribution (edited by H.A.).*

The interrelationship between pore throat / pore radii and pore throat / coordination number is shown in Figure 41a. The correlation between these two measured parameters is not so clear; still, a correlation is observed between the pores and throats when the throat radii are smaller than 65 microns. Which is the most frequent size as shown in Figure 41b. Figure 41a also shows the relationship between pore size / coordination number; as it is expected, the larger the radius, the higher the coordination number.

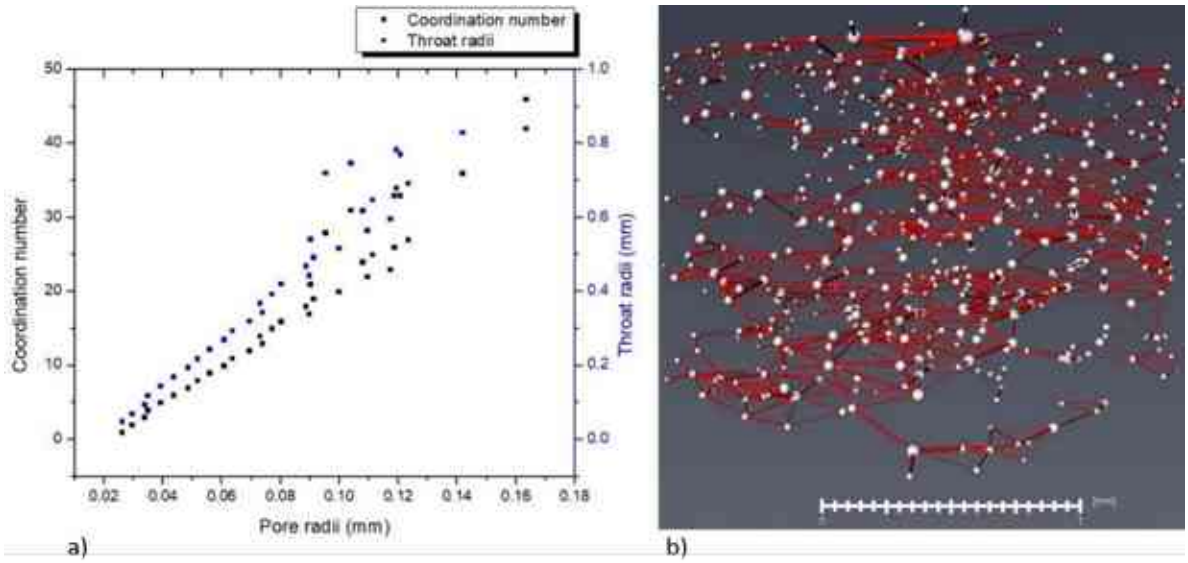

Figure 41 *a) Pore radius/coordination number and pore radius/throat radius correlations in Sample 1967, b) 3D view of the pore distribution with sizes smaller than 0.08 mm (edited by H.A.).*

8.2.2 Dry interval

Sample 1979: The subsample was extracted in the middle part of the 2 mm sample at 260 × 260 × 3000 volume. Porosities were determined from the stack of 3000 XCT slices with a low voxel size of 4 microns. The average porosity obtained from XCT images is 11.9%. The 3D pore network is presented in Figure 42. In Figure 42 a 3D view of the isolated pores are displayed. The pore size distribution is presented in Figure 43. This sample contains no pore connections, only solitary macro and micro pores, and the bulk of the channels were filled with carbonate cement as discovered during the thin section investigation. A few pore connections were observed randomly scattered across the sample. The pore radius varies between 4 μm and 15 μm and the most dominant pore size is 9 μm as shown in Table 6.

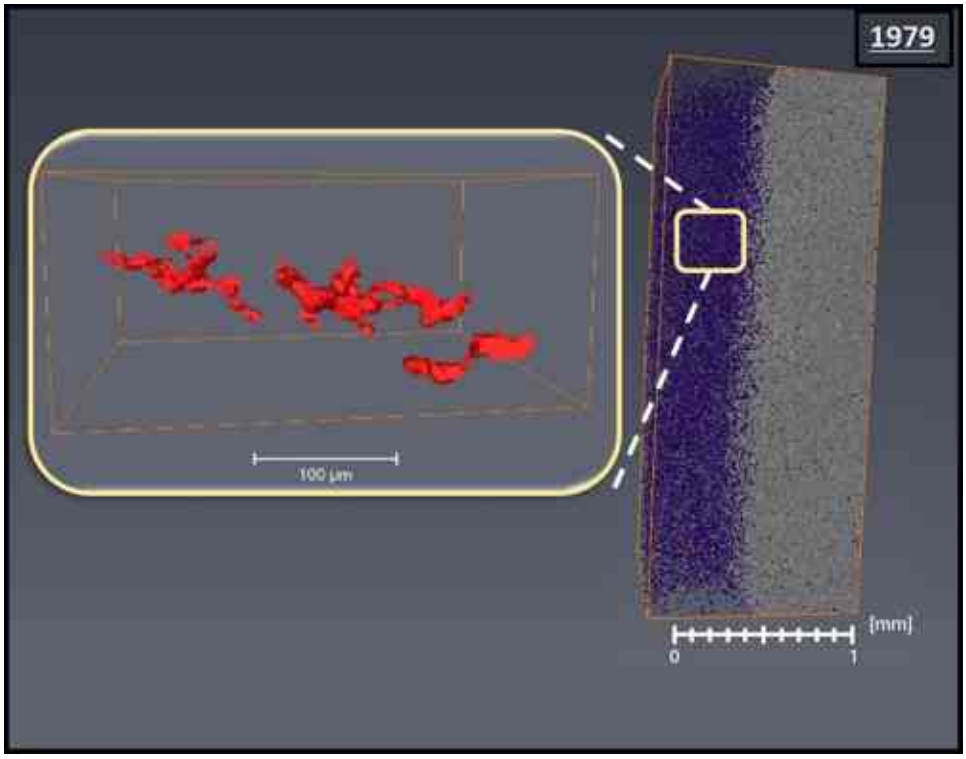

Figure 42 *Sample 1979 3D view of the pore space, with an example of the prevalent pore form in the sample (edited by H.A.).*

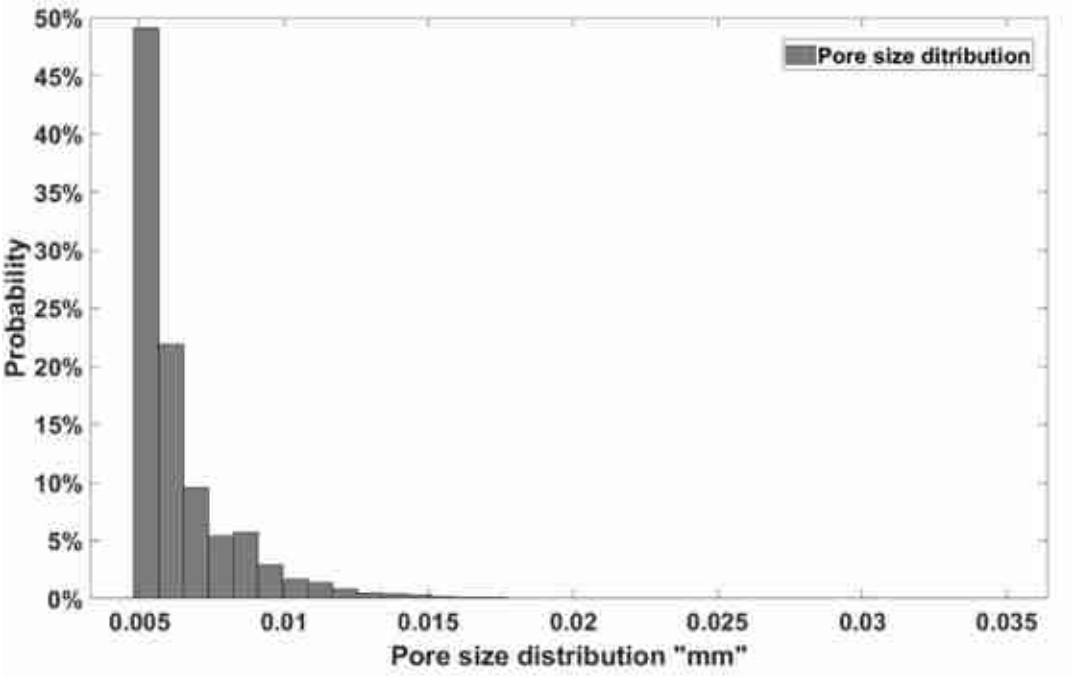

Figure 43 *Sample 1979 42 Pore size distribution (edited by H.A.).*

Table 6 *Pore volume and pore size in sample 1979*

Sample ID:	Total pore volume (%)	Total pore count	Minimum pore size "mm"	Average pore size "mm"	Maximum pore size "mm"	Pore radii percentiles		
						D 10 "mm"	D 50 "mm"	D 90 "mm"
1979	11.9	269318	0.00796	0.00636	0.0348	0.00496	0.00625	0.00901

Sample 1980: The subsample was extracted in the middle part of the 2 mm sample at sample at 380 × 300 × 3700 volume. The porosities were determined from the stack of 3700 XCT slices with a low voxel size of 4 microns. The average porosity obtained from XCT images is 14%. The 3D pore network is presented in Figure 44. A 3D view of the isolated pores is displayed in Figure 44. The pore size distribution is presented in Figure 45. This sample doesn't contain any pore connections, only solitary macro and micro pores, and the bulk of the channels were filled with carbonate cement as discovered during the thin section investigation. A few pore connections were observed randomly scattered across the sample. The microscopic analysis showed similar features as in the Sample 1979, where fossils, fossils fragments and even the matrix were dissolved and later totally filled with mosaic calcite. The pore radius varies between 4 μm and 40 μm and the most dominant pore size is 13 μm as shown in Table 7.

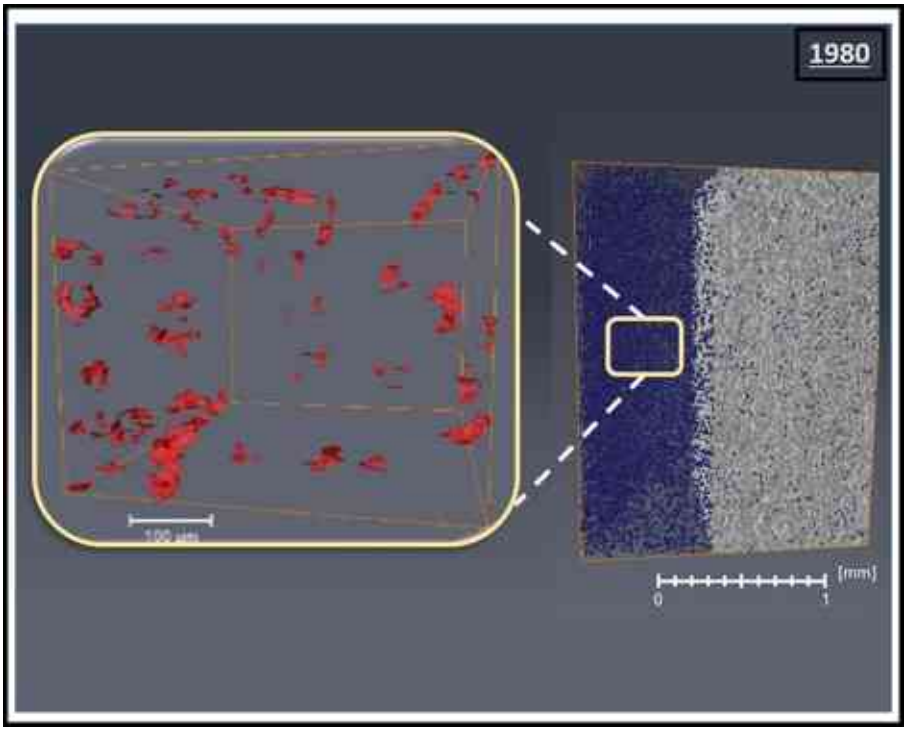

Figure 44 *Sample 1980 3D view of the pore space, with an example of the prevalent pore form in the sample (edited by H.A.).*

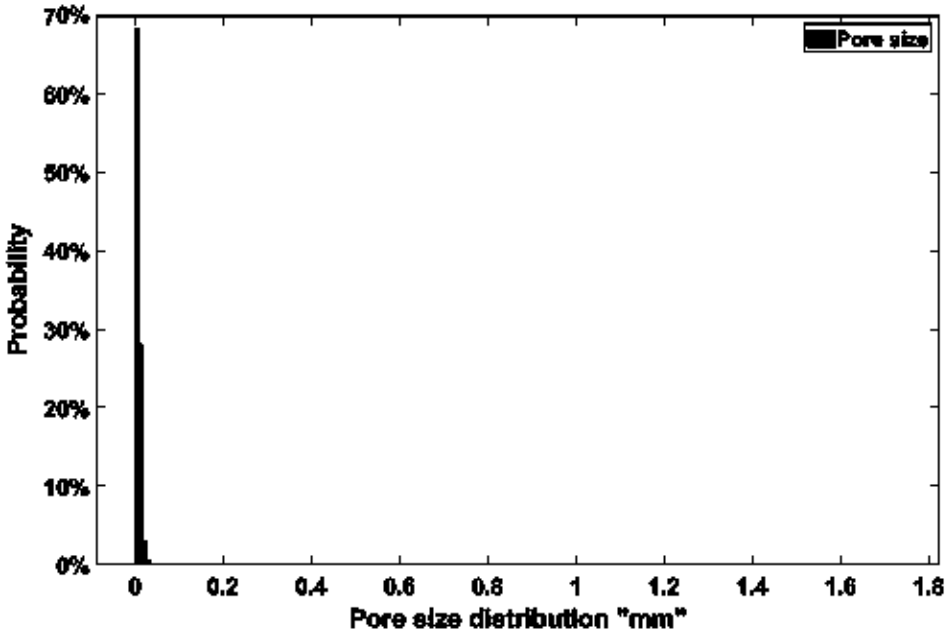

Figure 45 *Sample 1980 pore size distribution (edited by H.A.).*

Table 7 *Pore volume and pore size in sample 1980*

Sample ID:	Total pore volume (%)	Total pore count	Minimum pore size "mm"	Average pore size "mm"	Maximum pore size "mm"	Pore radii percentiles		
						D 10 "mm"	D 50 "mm"	D 90 "mm"
1980	14	1048575	0.00496	0.00836	0.0992	0.00496	0.007158	0.013471

In Figure 46, the PSD for the four samples is compared and Figure 47 gives the D10, D50 and D90 percentiles for the samples. For the dry interval represented by samples 1979 and 1980, the most dominant pore size is 0.009 mm and 0.013 mm, respectively. Larger pore sizes are dominant in the other two samples from the productive interval, where the most frequent value is around 0.085 mm and large pore sizes as high as 0.14 mm were found.

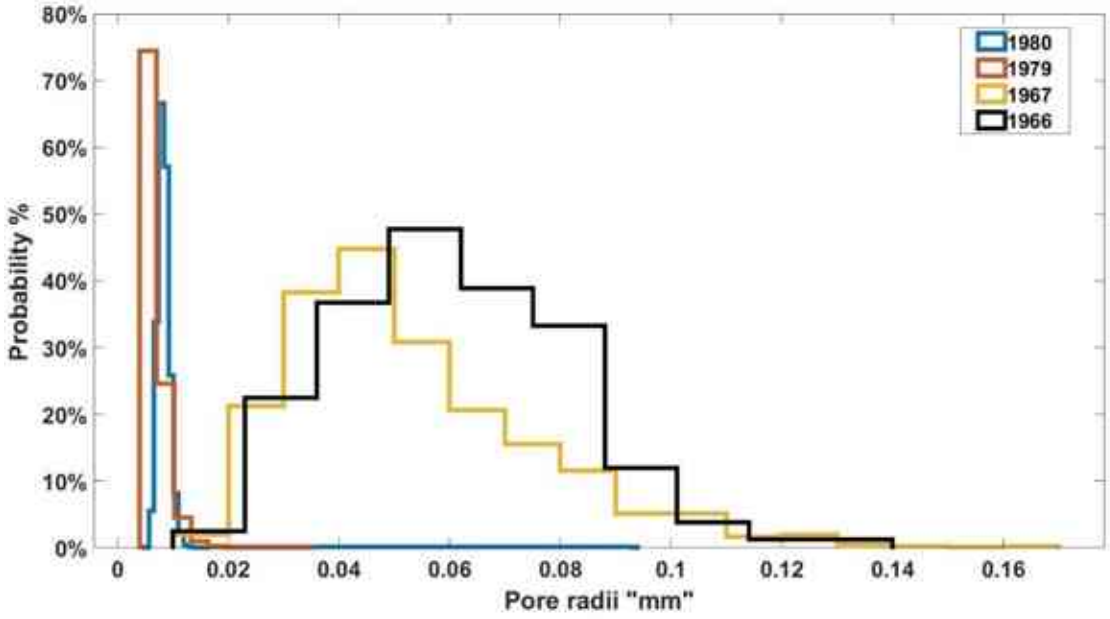

Figure 46 PSD for the four samples (edited by H.A.).

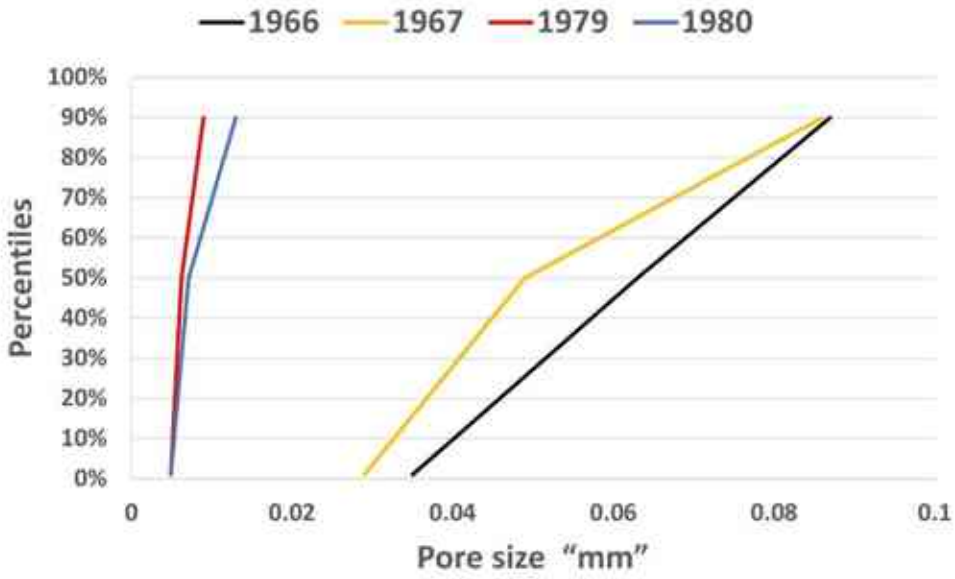

Figure 47 *Pore size percentiles for four samples (edited by H.A.).*

The 2D pore volume fraction against the calculated 2D fractal dimension is depicted from Figure 48 to Figure 51. The 2D fractal dimension is a number higher than 1 and lower than 2. 1 in the case of standard geometric features such as lines and circles, the more complex and irregular the shape is, the higher the number. For the two samples from the upper part a trend was observed between the porosity and the fractal dimension, indicating a direct relation. Moreover, the 2D fractal dimension has high values ranging between 1.65 and 1.67 indicating irregular pore shapes and rough pore surfaces. The pore structure takes complex irregular shapes and no correlation was observed between the pore volume and the fractal dimension for the lower interval samples (1979 and 1980). The pores have irregular complicated shapes, and this irregularity continues to appear at all depth intervals regardless of pore sizes.

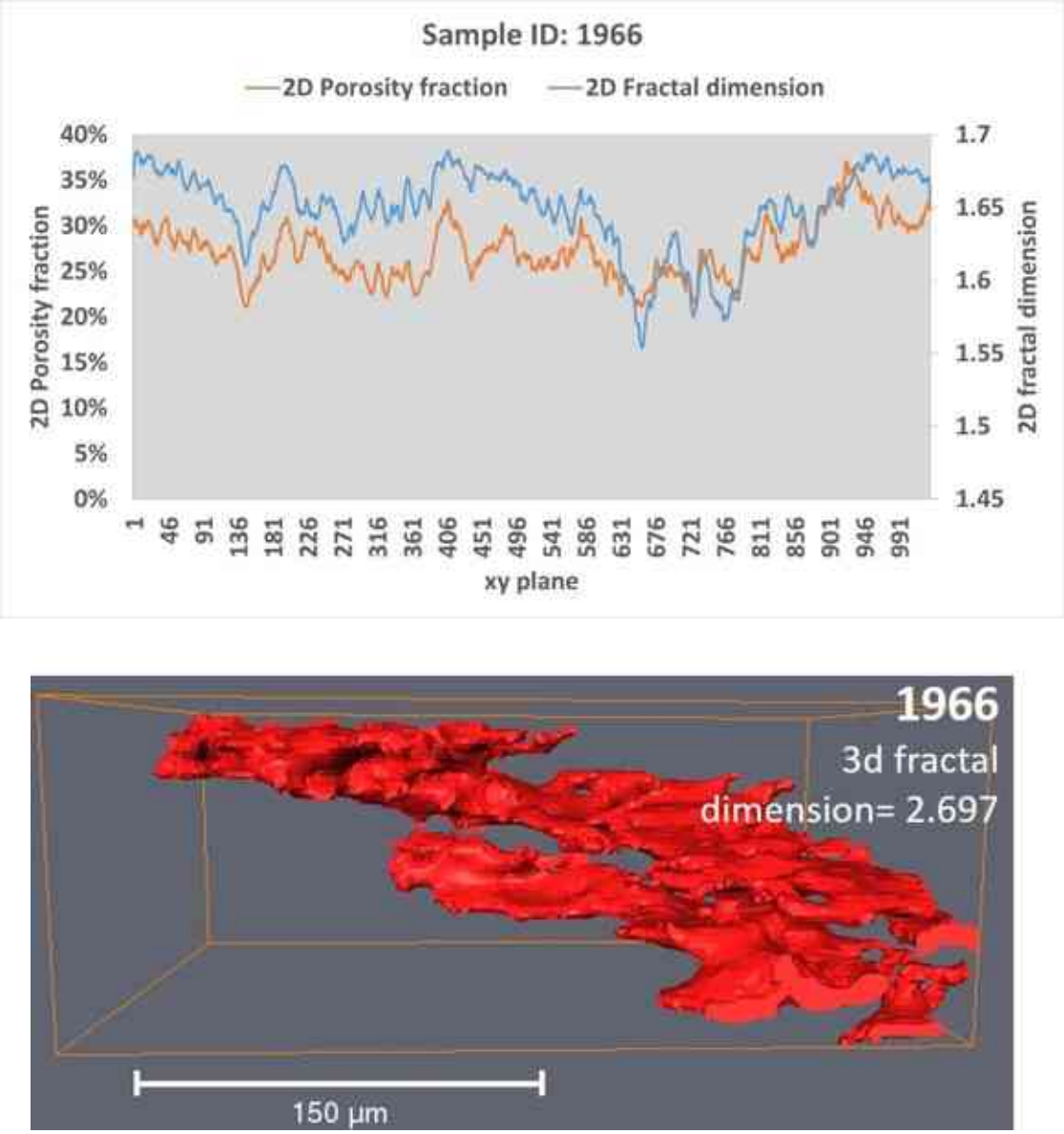

Figure 48 *Pore volume / 2D fractal dimension distribution (up), and 3D pore view showing the pore connectivity and the 3d fractal dimension in a macro scale (down) (edited by H.A.).*

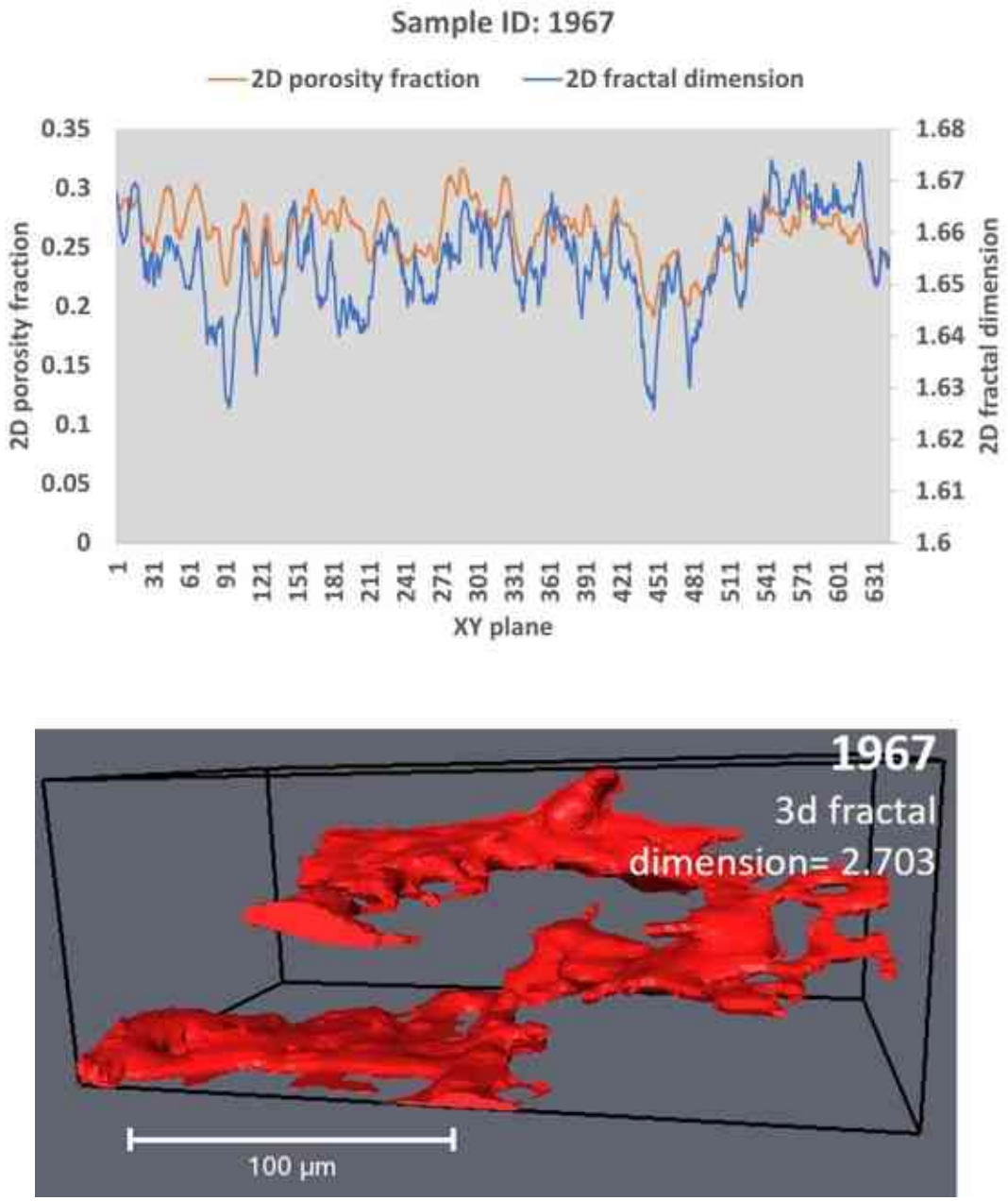

Figure 49 *Pore volume / 2D fractal dimension distribution (up), and 3D pore view showing the pore connectivity and the 3D fractal dimension in a macro scale (down) (edited by H.A.).*

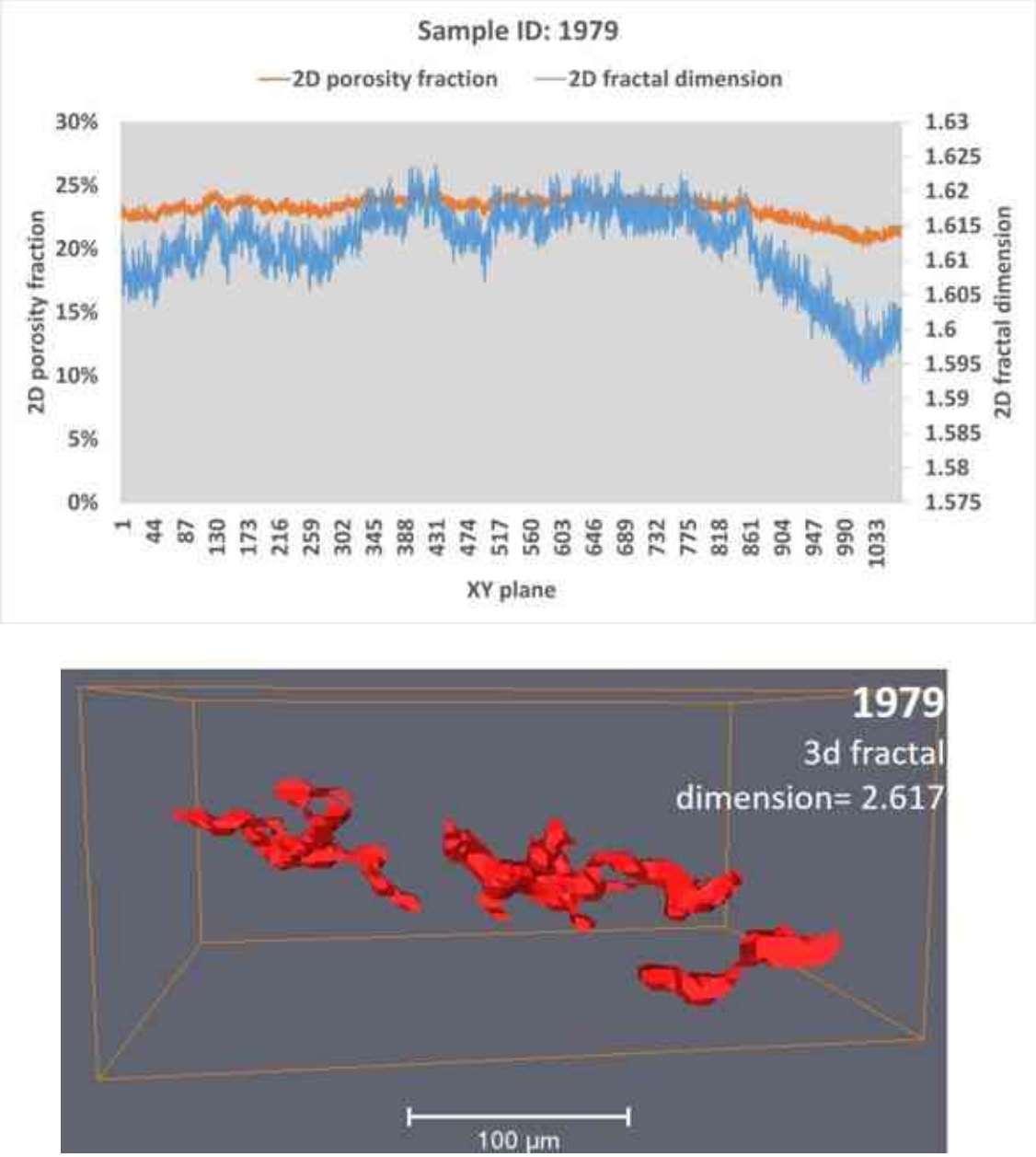

Figure 50 *Pore volume / 2D fractal dimension distribution (up), and 3D pore view showing the pore shapes in a macro scale and 3D fractal dimension (down) (edited by H.A.).*

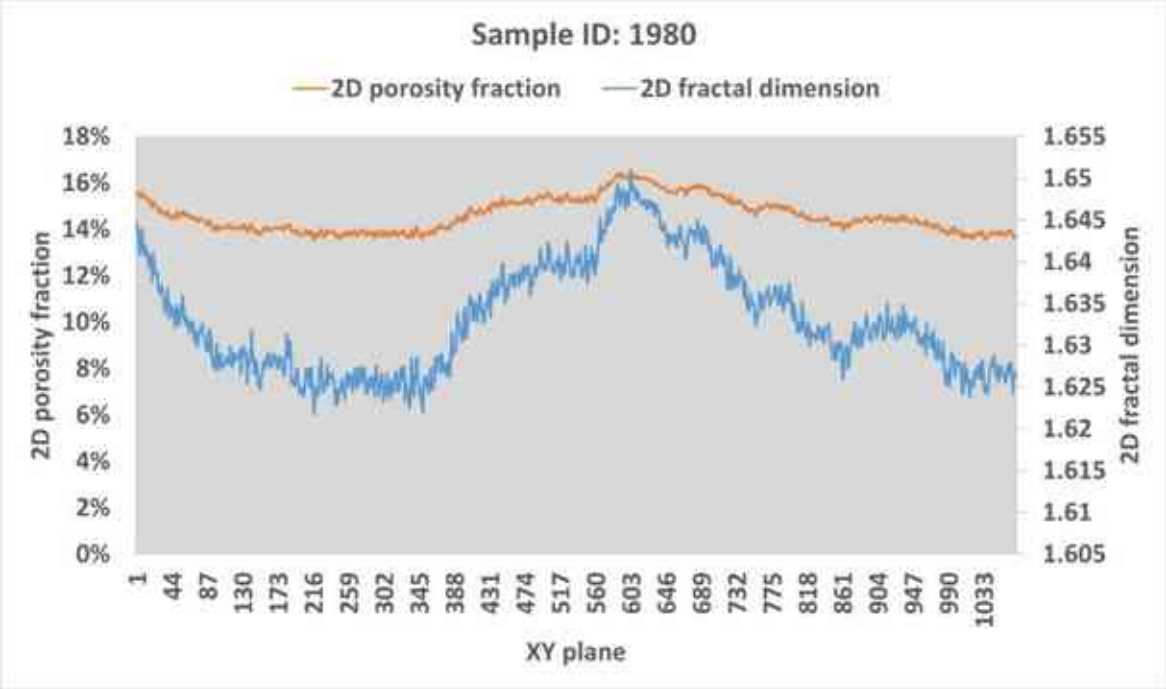

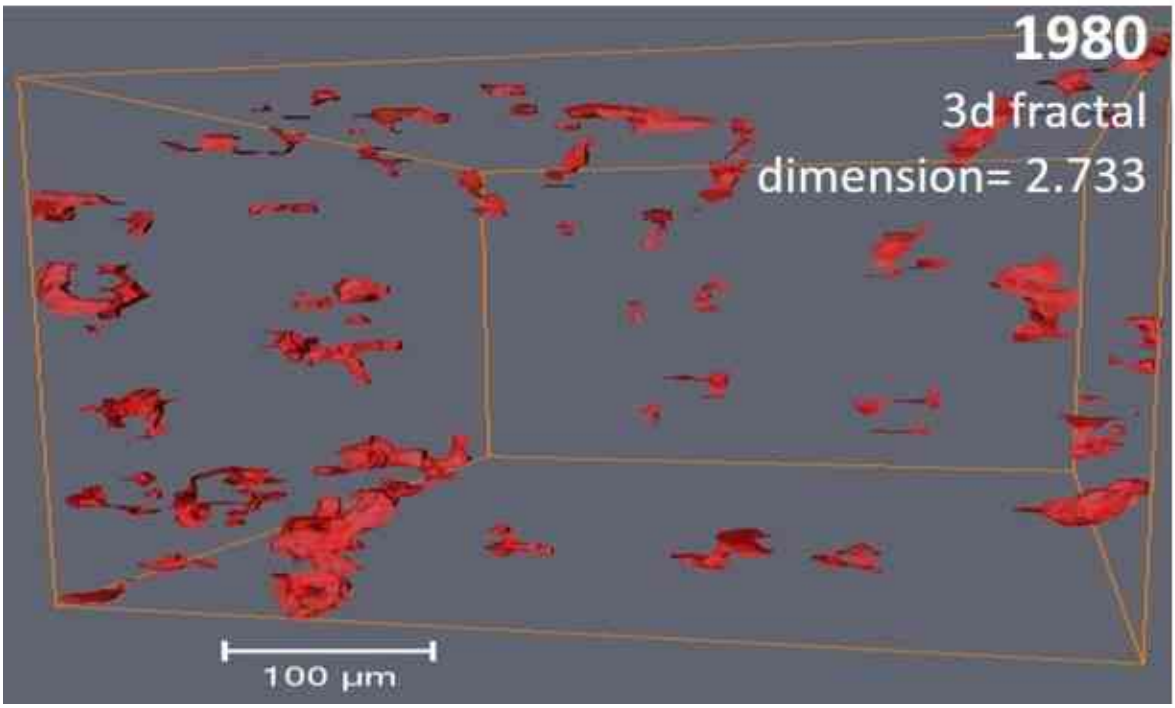

Figure 51 *Pore volume / 2D fractal dimension distribution (up), and 3D pore view showing the pore shapes in a macro scale and 3D fractal dimension (down) (edited by H.A.).*

8.3 Flow properties (permeability simulation)

In order to study the reservoir properties and understand the fluid flow patterns, I have selected a region of interest within the sample as illustrated in Figure 27 for simulation experiments. The sample was encapsulated on four faces, creating a controlled experimental setup. To guide the flow along a specific direction, experimental setups were added to two opposite faces of the sample. This setup allows to investigate the flow behavior in three directions: X, Y, and Z. By repeating this process, I analyzed and evaluated the flow patterns and characteristics in each direction

8.3.1 Productive interval

8.3.1.1 Pore-Scale Flow Pathway Variations

-Sample 1966: The flow streamlines in the X, Y, and Z direction are depicted, highlighting the flow behavior within the sample. The streamlines in X direction is shown in Figure 52a. The streamlines represented in red, indicating a mid-range velocity with relatively little change over the sample. However, distinctive regions with disconnected pores can be seen, where the flow magnitude is very low. These regions represent potential barriers or obstructions within the sample that hinder the flow. Further details about the flow properties are shown by a 2D slice through the flow streamlines Figure 52b. Certain areas of the pores show high flow magnitude, indicating favorable fluid pathways some connected pores exhibit a low velocity magnitude, suggesting possible constriction or flow resistance within these specific regions.

In the Y direction, the flow velocities exhibit higher magnitudes, as depicted by the streamlines in Figure 53a. This suggests that the fluid flow in the Y direction experiences greater flow velocity. This indicates favorable flow conditions within the pore network in Y direction Figure 53b.

In the Z direction, the flow streamlines are depicted with lower magnitudes compared to the X and Y directions Figure 54a. The streamlines appear to be fewer and represented with lower velocities. This observation suggests that the fluid flow in the Z direction experiences less momentum and lower flow rates compared to the other directions. Examining the 2D slice through the flow in the Z direction reveals interesting characteristics in Figure 54b. Some regions within the sample exhibit high velocity magnitudes, indicating preferential pathways or

conduits through which the fluid flows with greater speed. On the other hand, there are regions with little or no flow, where the velocity magnitudes remain low. This disparity in flow behavior within the Z direction suggests the presence of heterogeneity or variations in the permeability or connectivity of pores in different regions.

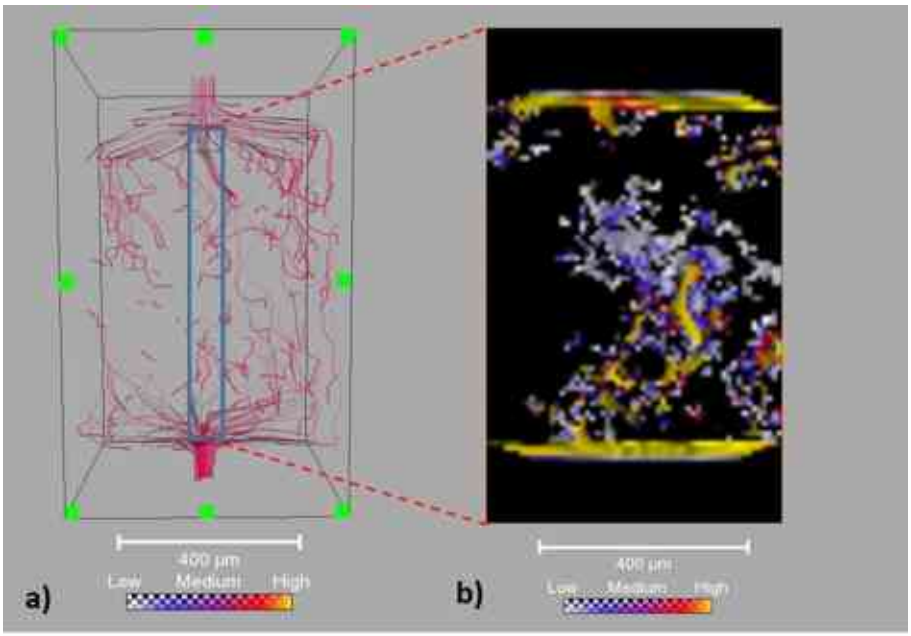

Figure 52 *Sample 1966; a) Flow streamlines in the X direction are depicted in red, representing a mid-range velocity with relatively little change over the sample. b) A 2D slice through the flow streamlines reveals varying flow magnitudes within the pores. Some connected pores have high flow magnitude, whilst others display low velocity magnitude, indicating probable flow limits or constriction (edited by H.A.).*

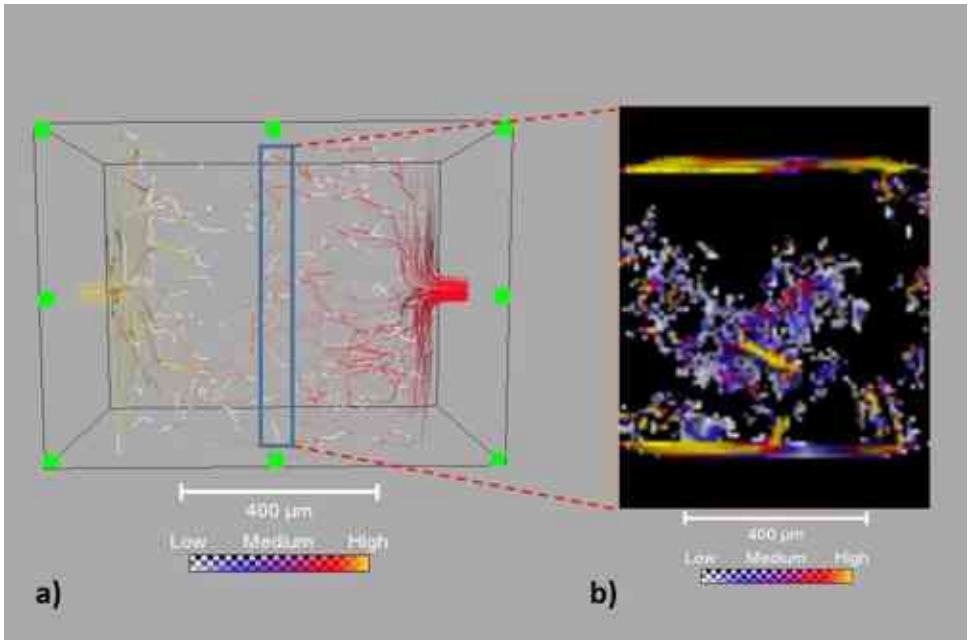

Figure 53 *Sample 1966; a) Flow streamlines in the Y direction are depicted in yellow and red, representing a mid-range to high over the sample. b) A 2D slice through the flow streamlines reveals varying flow magnitudes within the pores. Some connected pores have high flow magnitude, whilst others display low velocity magnitude, indicating the presence of heterogeneity or variations in the permeability or connectivity of pores in different regions (edited by H.A.).*

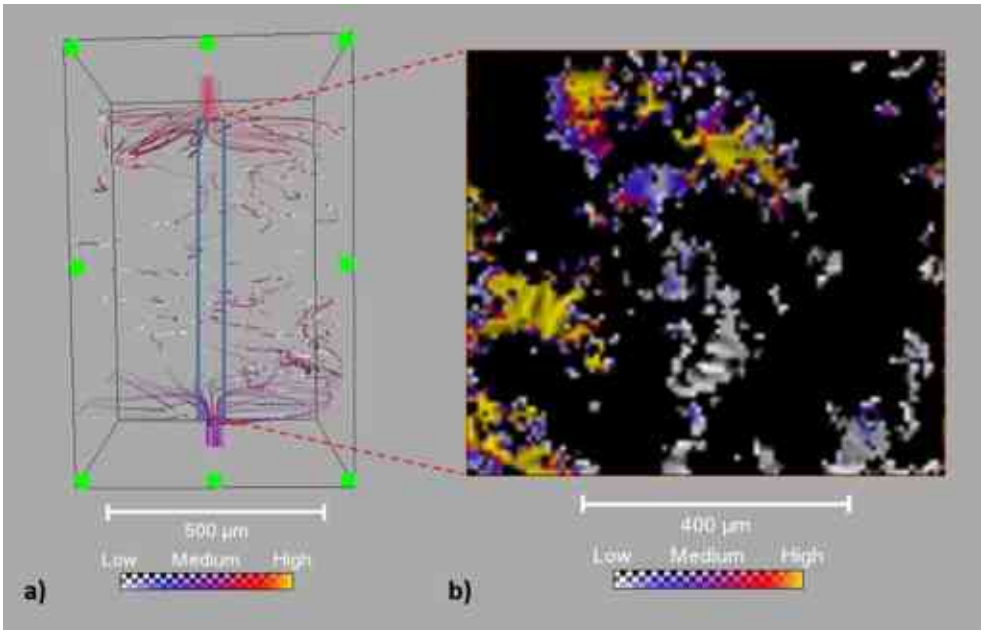

Figure 54 *Sample 1966; a) Flow streamlines in the Z direction are depicted in purple, representing a low-range velocity with relatively little change over the sample. b) A 2D slice through the flow streamlines reveals varying flow magnitudes within the pores. Some connected pores have high flow magnitude, whilst others display low velocity magnitude, indicating probable flow limits or constriction (edited by H.A.).*

Interesting flow behavior can be seen in the 2D depiction of the average Y component velocity against the X component in Figure 55. The tendency may be seen on the plot, where the flow initially starts with higher values in the positive direction. As we move along the X axis, suggesting a change in the flow's direction or its orientation in the Y direction. The average velocity of the Y component achieves its highest value in the positive direction near the plot's center, where a prominent peak can be seen. This peak, which denotes a concentrated area of higher flow magnitude, can be related to certain reservoir structural elements or flow dynamics. Lower values of the flow's fluctuations between positive and negative directions are still present. The flow progressively increases once more at the end of the X axis, possibly denoting a change or transition in the flow behavior or the presence of certain flow routes or pathways.

The average Z component velocity against the X component is shown in Figure 56. The flow initially starts with high velocity. The velocity varies between positive and negative values as we go along the X axis, indicating changes in the flow direction or variations in the velocity of the Z component. Then the flow stabilizes with no significant variation in the Z component's

velocity. Towards the end of the X axis, the plot shows another peaks, these peaks point to areas where the Z component velocity achieves its maximum amplitude, possibly pointing to the presence of certain flow patterns or structural elements that contribute to the observed velocity changes.

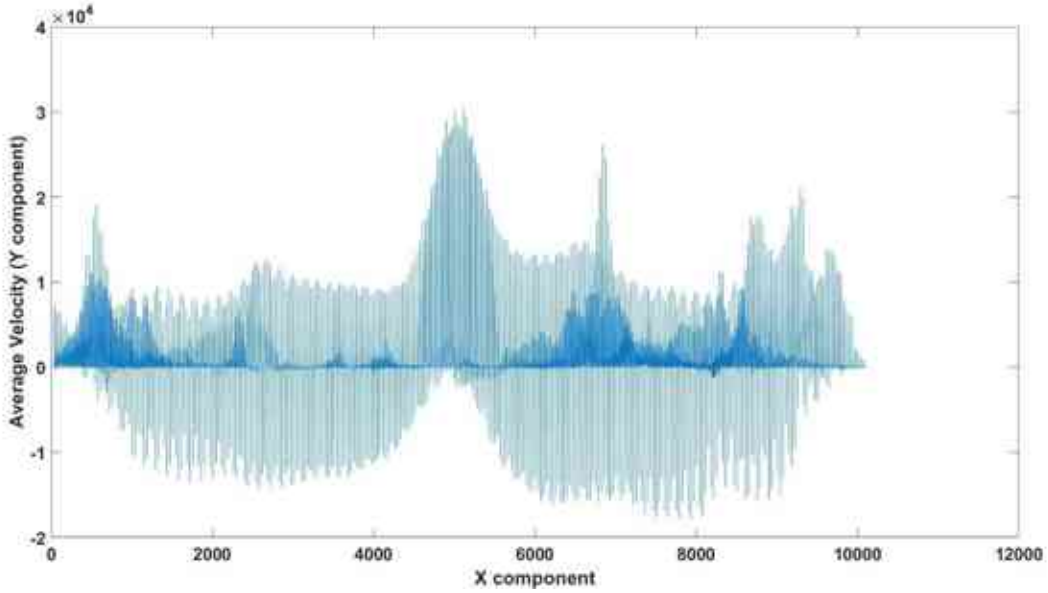

Figure 55 *Sample 1966; the variation of the average flow velocity along the layers of the 1966 carbonate sample comparing the average velocity in the Y component as a function of X component. The peak of the flow velocity depicts a high flow zone, and the variation of the flow velocity denotes a change in the flow orientation (edited by H.A.).*

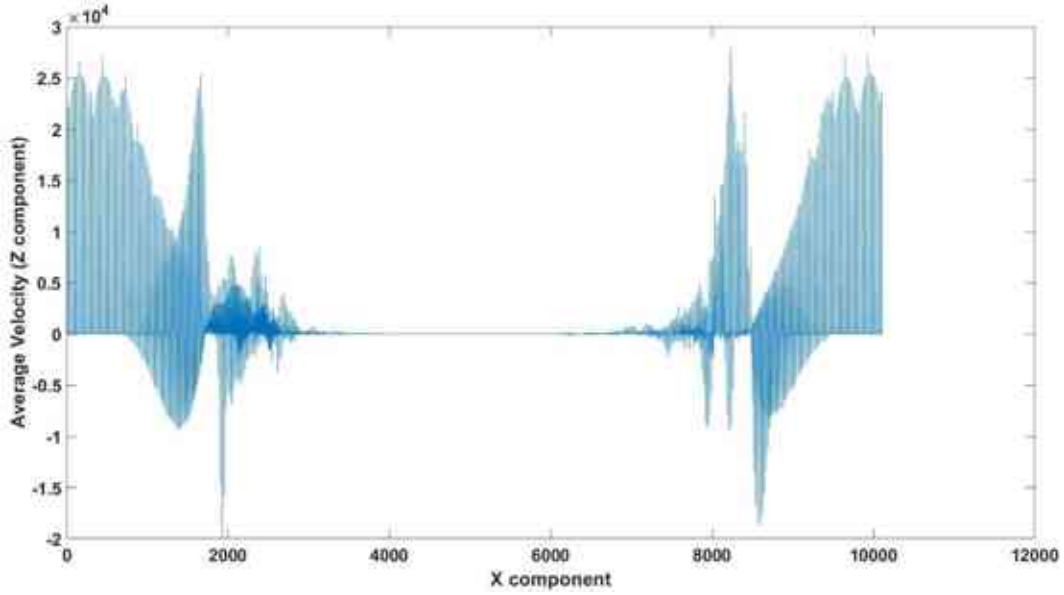

Figure 56 *Sample 1966; the variation of the average flow velocity along the layers of the 1966 carbonate sample comparing the average velocity in the Z component as a function of X component. A high flow zone is depicted by the flow velocity peak, followed by a stable flow velocity, and then a high velocity with a change in direction (edited by H.A.).*

Sample 1967

The flow streamlines in sample 1967 in the X, Y, and Z direction are depicted, highlighting the flow behavior within the sample. The streamlines in X direction is shown in Figure 57a. The streamlines represented in red, indicating a mid to high-range velocity with relatively little change over the sample. Further details about the flow properties are shown by a 2D slice through the flow streamlines Figure 57b. Certain areas of the pores show high flow magnitude, indicating favorable fluid pathways some connected pores exhibit a low velocity magnitude, suggesting possible constriction or flow resistance within these specific regions.

In the Y direction, similarly the flow velocities exhibit high magnitudes, as depicted by the streamlines in Figure 58a. The 2D slice through the flow, shows that the flow magnitude in the pores is high. This indicates favorable flow conditions within the pore network in Y and X direction Figure 58b.

In the Z direction, the flow streamlines are depicted with lower magnitudes compared to the X and Y directions Figure 59a. The streamlines appear to be fewer and represented with lower

velocities. This observation suggests that the fluid flow in the Z direction experiences less momentum and lower flow rates compared to the other directions.

Examining the 2D slice through the flow in the Z direction. Figure 59a reveals that few regions within the sample exhibit high velocity magnitudes, indicating preferential pathways through which the fluid flows with greater speed. However, a significant portion of the pores exhibit weak flow, with low velocity magnitudes. This disparity in flow behavior within the Z direction suggests the presence of heterogeneity or variations in the permeability or connectivity of pores in different regions.

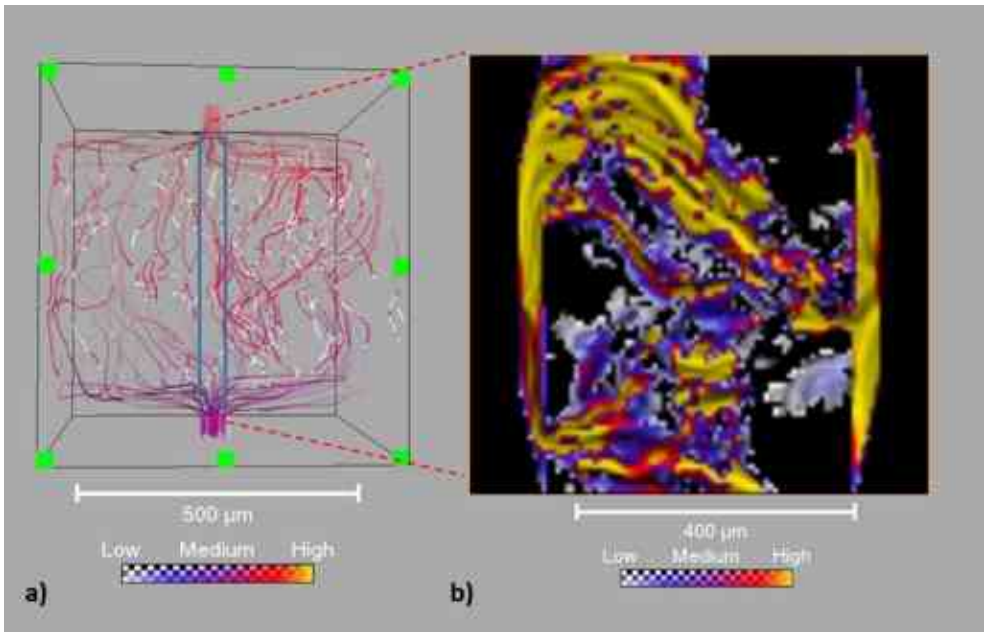

Figure 57 *Sample 1967; a) Flow streamlines in the X direction are depicted in red, representing a mid to high-range velocity with relatively little change over the sample. b) A 2D slice through the flow streamlines reveals varying flow magnitudes within the pores. Some connected pores have high flow magnitude, whilst others display low velocity magnitude, indicating probable flow limits or constriction (edited by H.A.).*

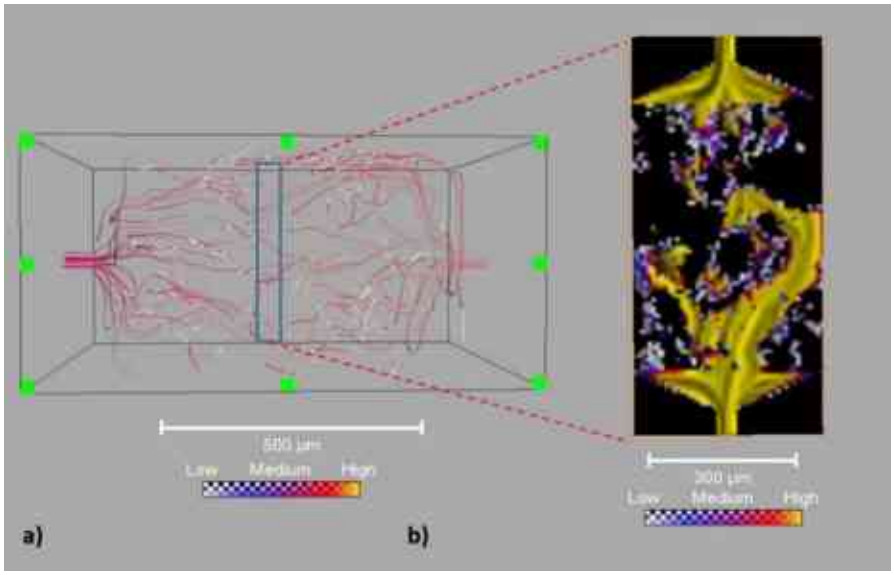

Figure 58 *Sample 1967; a) Flow streamlines in the Y direction are depicted in red, representing a mid-range to high over the sample. b) A 2D slice through the flow streamlines reveals high and uniform flow magnitudes within the pores. Some connected pores have high flow magnitude, whilst others display low velocity magnitude, indicating the presence of heterogeneity or variations in the permeability or connectivity of pores in different regions (edited by H.A.).*

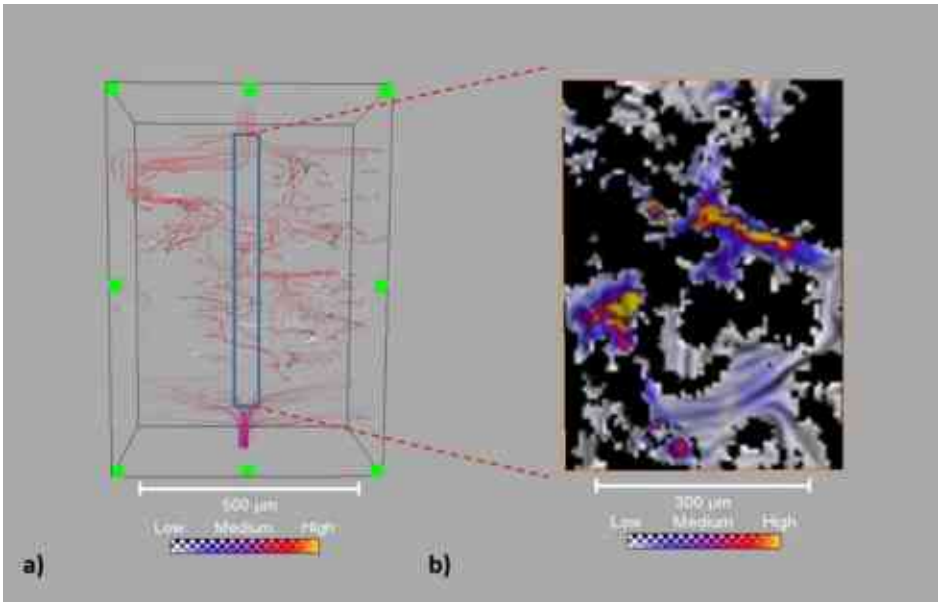

Figure 59 *Sample 1967; a) Flow streamlines in the Z direction are depicted in purple, representing a low-range velocity with relatively little change over the sample. b) A 2D slice through the flow streamlines reveals varying flow magnitudes within the pores. Some connected pores have high flow magnitude, whilst others display low velocity magnitude, indicating probable flow limits or constriction (edited by H.A.).*

Figure 60 depicts the velocity variation of the Y component in relation to the X component. The plot displays the correlation between the velocity of the Y component and the X component, highlighting various patterns and trends. The velocity of the Y component begins at lower values at first and subsequently rises in both positive and negative directions. However, there is a strong concentration of the velocity in the positive direction, indicating a dominant flow pattern. Several small peaks can be observed, representing localized regions of relatively higher velocity within the sample. In the middle of the plot, a peak is observed, indicating a significant increase in the Y component velocity. Following the peak, the velocity gradually decreases again, suggesting a transition or change in flow behavior within that specific region.

Figure 61 depicts the velocity variation of the Z component in relation to the X component, highlighting various patterns and trends. Initially, the Z component velocity starts at high values, indicating a relatively strong flow. The plot shows two peaks that are overlapped, suggesting regions of enhanced velocity in the positive direction. Following this, the velocity changes direction, leading to a peak in the negative direction. Subsequently, the plot displays a straight line, indicating a relatively stable flow with no significant variation in the Z component velocity. Towards the end of the plot, the velocity increases, and a peak is observed, highlighting a localized region of enhanced flow or altered flow behavior.

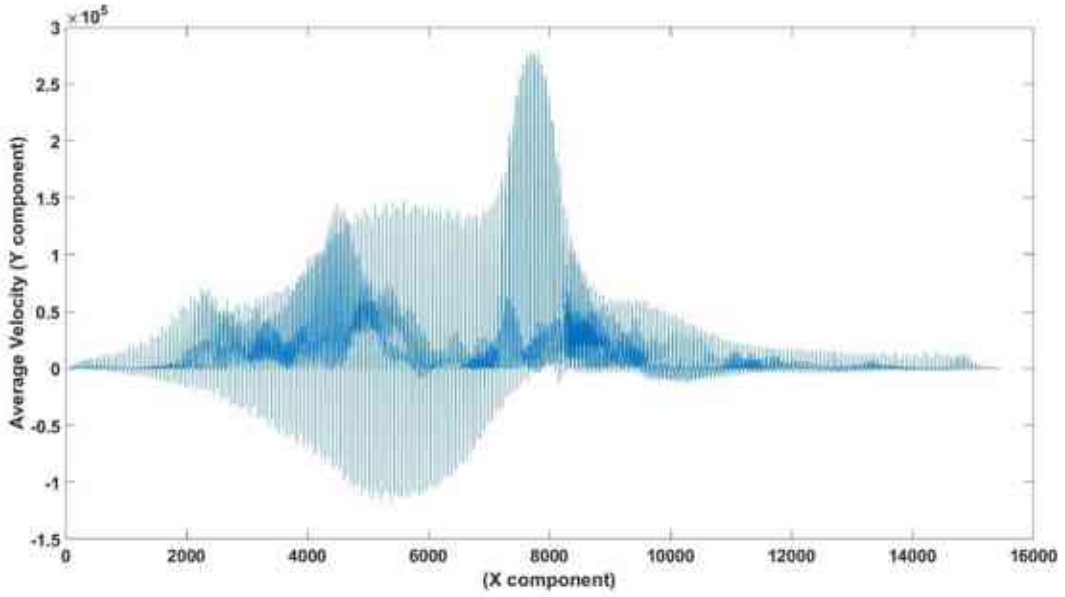

Figure 60 *Sample 1967; Relationship between Y component velocity and the X component, the 2D plot illustrates the variations in Y component velocity as a function of the X component (edited by H.A.).*

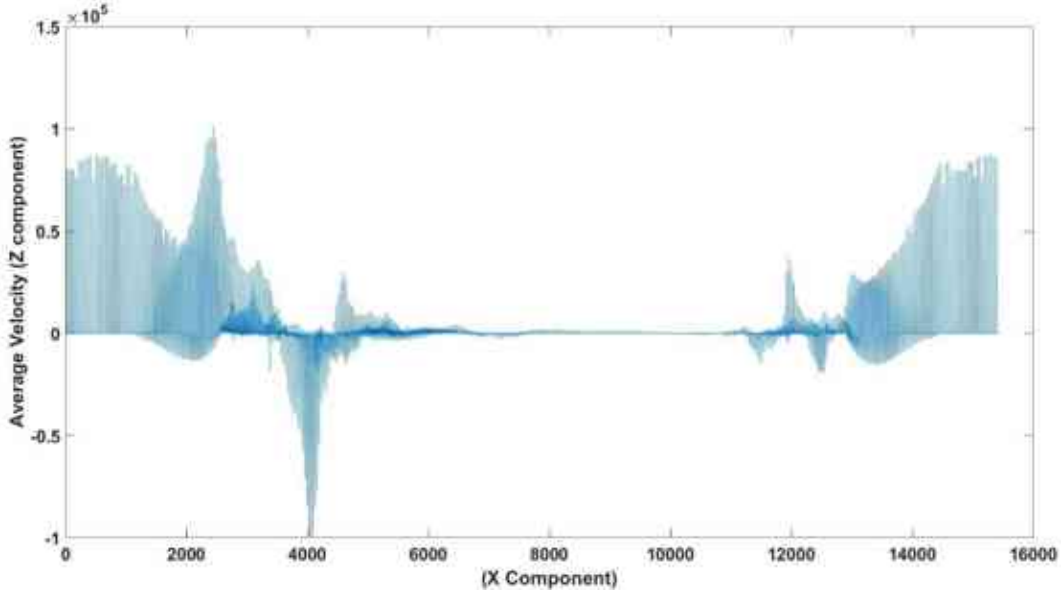

Figure 61 *Sample 1967; Relationship between Z component velocity and the X component, the 2D plot illustrates the variations in Z component velocity as a function of the X component (edited by H.A.).*

8.3.1.2 Understanding Reservoir Potential through Formation Factor Analysis

Sample 1966:

The effective electrical conductivity tensor gives global information about the electrical conduction capabilities of the material. To compute the dimensionless electrical conductivity tensor the following equation is solved as

$$\varepsilon \frac{\vec{\sigma}}{\sigma_{solution}} = \varepsilon(\underset{I}{\rightarrow} + \frac{1}{V_f} \int_{Sf_x} \underset{nf_s}{\longrightarrow} \underset{b}{\rightarrow} d_s, \quad (18)$$

where ε is the porosity $\sigma_{solution}$ is the solution electrical conductivity V_f is the volume of the fluid, S_{fs} is the area of fluid solid interface nf_s, is the normal to the fluid-solid interface directed from the fluid to the solid phase. The inverse of the conductivity tensor is the formation factor tensor and the formation factor scalar is the average value of the eigenvalues of this last tensor. All this is computed by the Effective Formation Factor Calculation module in Avizo. The formation factor helps in evaluating the flow behavior and assessing the overall fluid flow potential within the porous medium. The reservoir potential is shown in Figure 62 based on the calculation of the formation factor as mentioned earlier. The observed velocity tensors and the 3D rendering of the reservoir potential are in agreement. The reservoir potential appears to be relatively homogeneous in the X and Y directions, suggesting a rather uniform distribution of

the formation factors. This shows that the formation factor is generally consistent in these directions, resulting in less variety in the behavior of fluid flow. On the other hand, an apparent feature in the reservoir potential can be seen while in the z direction. In the midst of the reservoir, there occurs a cutoff or a change in the formation factor. This cutoff denotes a change or break in the connectivity or pore structure in the Z direction Figure 62.

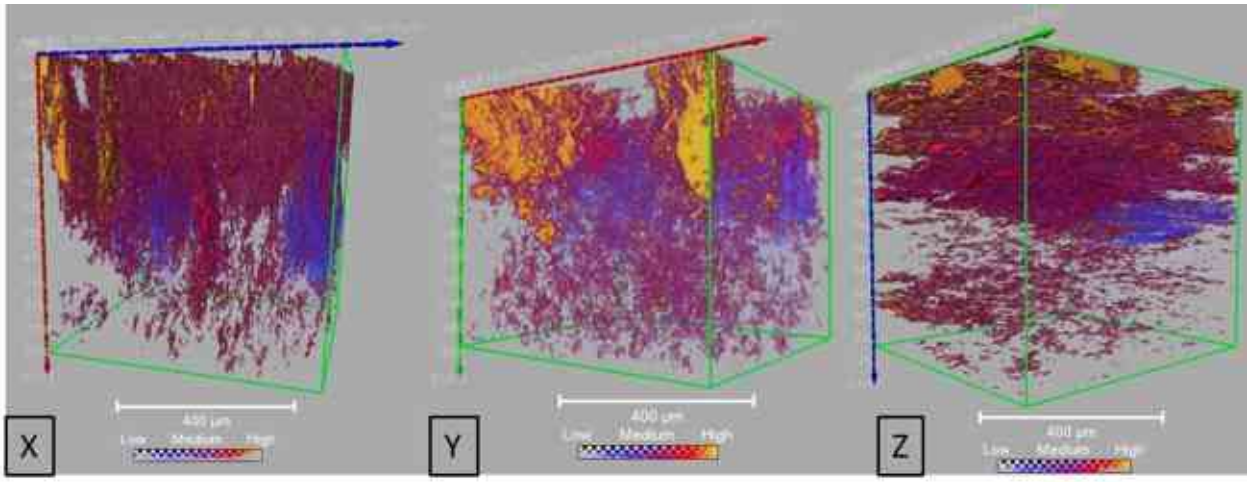

Figure 62 *Sample 1966; the spatial distribution of the formation factor. The reservoir potential exhibits homogeneity in the X and Y directions, indicating a relatively uniform formation factor distribution. In contrast, the Z direction reveals a cutoff in the middle with a higher formation factor beyond it, suggesting a localized region of reduced fluid flow or lower permeability* (edited by H.A.).

Sample 1967:

A 3d rendering of the reservoir potential in X, Y, and Z direction is illustrated in Figure 63. In the X direction, the reservoir potential exhibits high values throughout the sample, indicating a relatively consistent potential distribution. There is a small decrease observed in the lower part, suggesting a slight variation in the potential within that region. In the Y direction, the reservoir potential shows a range from medium to high values. There are some localized areas where a slight decrease in the potential can be observed. However, these variations are relatively small, indicating a relatively homogeneous potential distribution along the Y direction. Similarly, in the Z direction, the reservoir potential displays a mid to high range. There is a small decrease in the lower part of the sample, indicating a slight variation in the potential within that region.

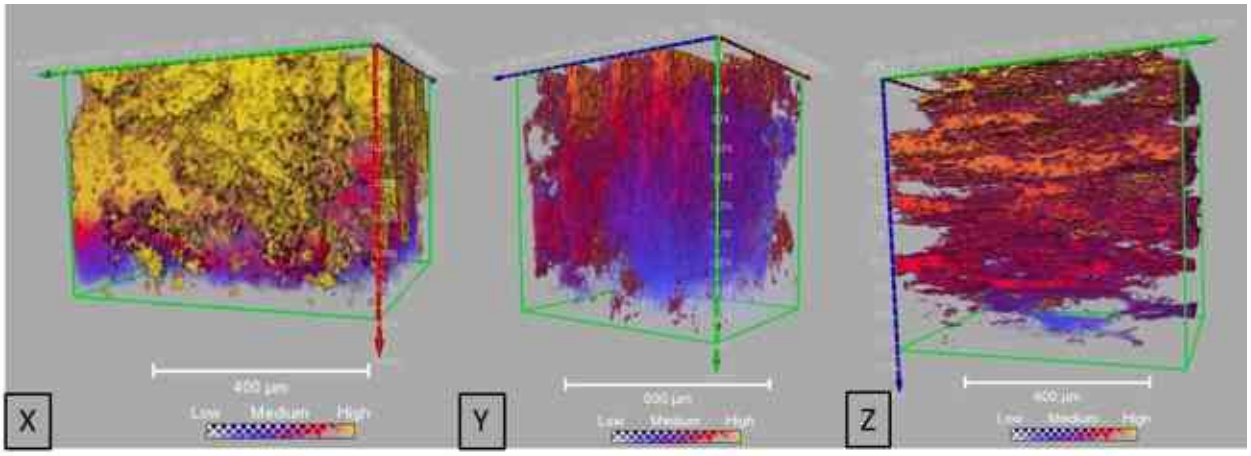

Figure 63 *Sample 1967; the spatial distribution of the formation factor. The reservoir potential exhibits low formation factor in X direction while higher formation factor observed in Y, and Z directions (edited by H.A.).*

8.3.1.3 Flow rate in the mirror of pore radius and channel length

Sample 1966

Flow rate in relation to throat radius is depicted in Figure 64. The figure illustrates how the flow rate varies with changes in throat radius. Initially, as the throat radius increases, the flow rate also increases, reaching a peak within the range of 12.5 to 18 microns. However, beyond this point, the flow rate begins to decrease as the throat radius continues to increase. The initial increase in flow rate with an increasing throat radius can be attributed to reduced flow resistance. As the throat radius widens, there is more space for the fluid to flow through, resulting in higher flow rates. However, this relationship is the subsequent decline in flow rate beyond a certain throat radius, which occurs within the range of 12.5 to 18 microns in this case. This behavior can be explained by the balance between the pressure drop across the throat and the velocity of the fluid. When the throat radius becomes too large, the fluid velocity decreases significantly due to the expansion of the flow path, causing a drop in flow rate.

Flow rate is influenced by channel length, as observed in figure 65. The relationship between flow rate and channel length shows that as the channel length increases, the flow rate initially increases, reaching its maximum within the range of 50 to 100 microns. However, beyond this range, the flow rate starts to decrease as the channel length continues to increase. The initial

increase in flow rate with an extended channel length is primarily driven by reduced flow resistance. Longer channels offer more space for the fluid to flow through, resulting in higher flow rates. This behavior can be advantageous when designing systems that require higher fluid throughput.

However, the decline in flow rate beyond the 50 to 100 micron range can be attributed to a combination of factors, including increased frictional losses and the development of laminar flow patterns at longer channel lengths. As the channel length becomes excessive, the flow rate becomes limited by these factors, causing a reduction in flow rate.

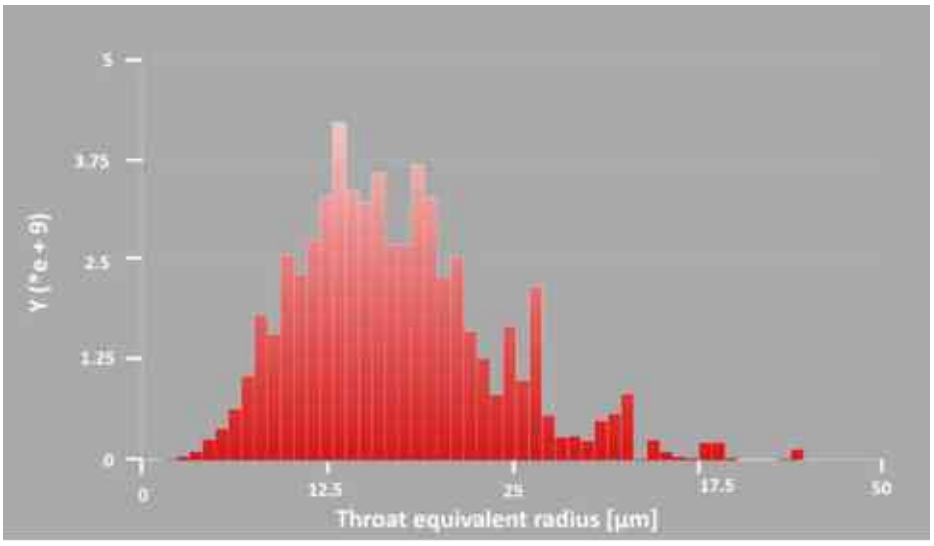

Figure 64 *Sample 1966: flow rate in the mirror of the equivalent throat radius (edited by H.A.).*

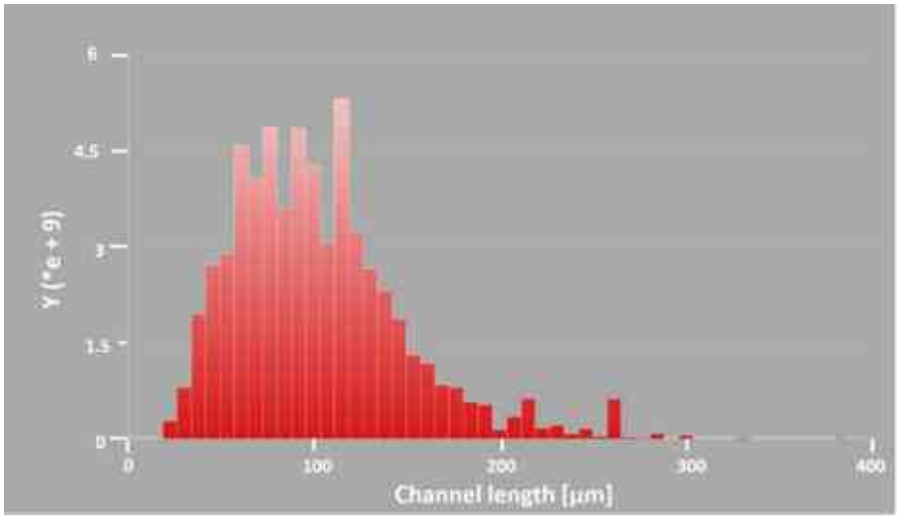

Figure 65 *Sample 1966: flow rate in the mirror of channel length (edited by H.A.).*

Sample 1967:

Flow rate in relation to throat radius is depicted in Figure 66. The figure illustrates how the flow rate varies with changes in throat radius. Initially, as the throat radius increases, the flow rate also increases, reaching a peak within the range of 10 to 20 microns. However, beyond this point, the flow rate begins to decrease as the throat radius continues to increase. The initial increase in flow rate with an increasing throat radius can be attributed to reduced flow resistance. As the throat radius widens, there is more space for the fluid to flow through, resulting in higher flow rates. However, this relationship is the subsequent decline in flow rate beyond a certain throat radius, which occurs within the range of 10 to 20 microns in this case. This behavior can be explained by the balance between the pressure drop across the throat and the velocity of the fluid. When the throat radius becomes too large, the fluid velocity decreases significantly due to the expansion of the flow path, causing a drop in flow rate.

Flow rate is influenced by channel length, as observed in figure 67. The relationship between flow rate and channel length shows that as the channel length increases, the flow rate initially increases, reaching its maximum within the range of 30 to 60 microns. However, beyond this range, the flow rate starts to decrease as the channel length continues to increase. The initial increase in flow rate with an extended channel length is primarily driven by reduced flow resistance. Longer channels offer more space for the fluid to flow through, resulting in higher flow rates. This behavior can be advantageous when designing systems that require higher fluid throughput.

However, the decline in flow rate beyond the 50 to 100 micron range can be attributed to a combination of factors, including increased frictional losses and the development of laminar flow patterns at longer channel lengths. As the channel length becomes excessive, the flow rate becomes limited by these factors, causing a reduction in flow rate.

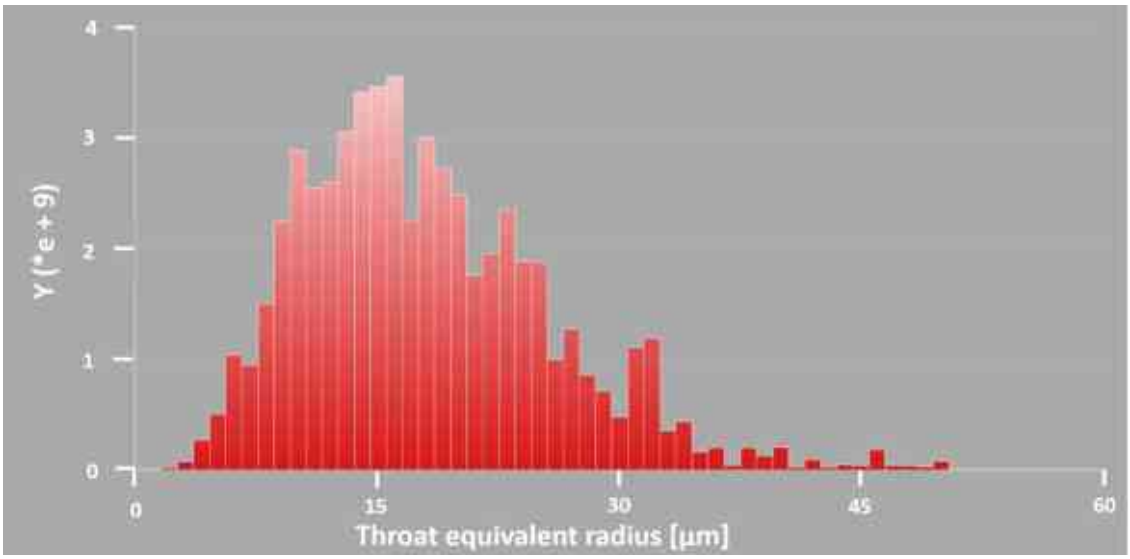

Figure 66 *Sample 1966: flow rate in the mirror of throat radius (edited by H.A.).*

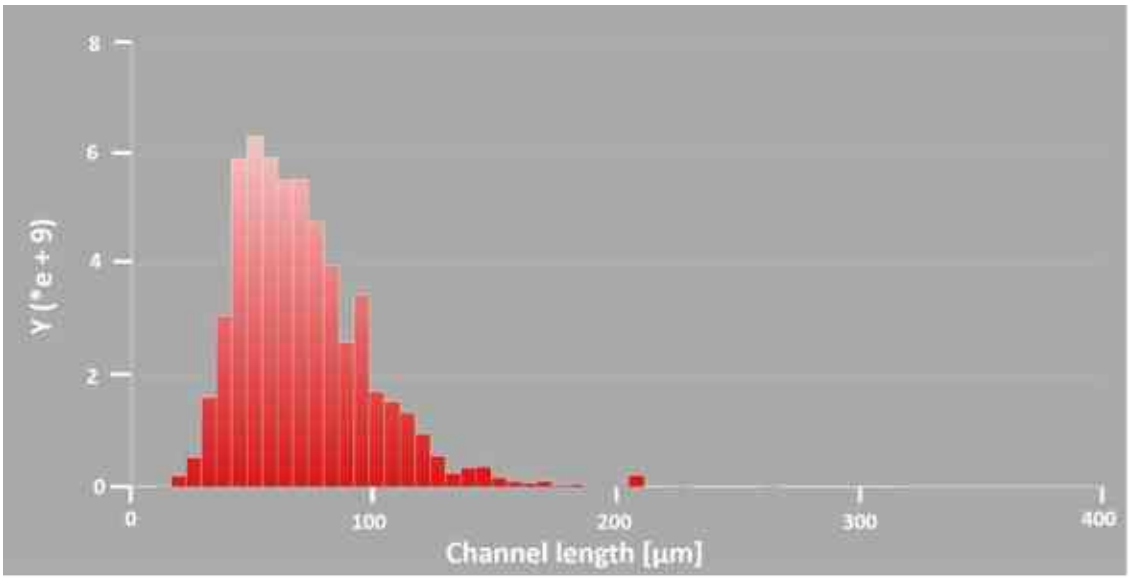

Figure 67 *Sample 1967: flow rate in the mirror of the channel length (edited by H.A.).*

9. Discussion

The accurate determination of porosity in image-based measurement systems is a critical step in the characterization of porous media. Various models and methods must be considered to evaluate uncertainty propagation in each step of the system. For instance, De Santo Ballester (2015) emphasized the importance of evaluating uncertainty propagation in image-based measurement systems. In micro CT image analysis of porous carbonates, Rezaei et al. (2019) highlighted the crucial evaluation of various thresholding algorithms to avoid distorted outcomes. Additionally, Xiong (2016) noted that the finite resolution of imaging techniques is the main source of uncertainty in pore space characterization. To overcome these problems, Keller (2013) suggested to combine different techniques, such as Focused Ion Beam (FIB) / Scanning Electron Microscope (SEM), nitrogen adsorption, and FIB.

Moreover, recent studies have demonstrated the potential of machine learning algorithms for automated analysis of complex geological structures. For example, Dos Anjos et al. (2021) demonstrated the effectiveness of deep learning for lithological classification of carbonate rock micro-CT images. This study highlights the potential of machine learning algorithms in gaining a deeper understanding of the petrophysical properties of rock samples.

Furthermore, the study by Zhang (2021) provided valuable insights into the pore-scale characterization and pore network model simulations of multiphase flow in carbonate rocks. By utilizing advanced imaging techniques and computational simulations, the study shed light on the complex fluid behavior within the pore network, highlighting the importance of considering heterogeneity and connectivity in modeling fluid flow in porous media.

In my study the porosity was determined by using different ML techniques. The K- means and FRFCM clustering tend to over-segment the pore volume by 7% to 12% compared to other segmentation algorithms, where pore volume varies between 25% and 30% (Figure 30). In general, this variability in pore volume can be attributed to the presence of microcrystalline cement formed during diagenetic processes at the microstructural scale and deposited within the void space and on the pore edges, which cannot be resolved by the micro-XCT. This situation leads to images having variable pixel intensities including

the pore edges. These pixels of varying intensities would not have been segmented into the same class by different ML algorithms. This microcrystalline cement has been observed by microscopic examination of the thin sections taken from the same samples. Figure. 30a and Figure. 30b show that the detected pores count of the K-means clustering and MINCE methods is higher than that of the other methods. In the case of T2FE, the small pores are more frequent than the large ones. In the case of the FRFCM algorithm, the large pores are more dominant. Additionally, three groups can be defined; 1- T2FE, 2- MINCE and k-Means, 3- Fuzzy c-means, Ground Trouth, and Naive Bayes (Figure 30).

Overall, Type 2 Fuzzy entropy classifier performed the best overall, achieving the highest AUC value of 0.984 and the highest CA, F1-score, precision, and recall values among all classifiers. The Minimum cross entropy classifier also performed well, with an AUC value of 0.974 and a CA of 0.946. The K-means and Fuzzy C-means classifiers achieved slightly lower performance, with CA values of 0.877 and 0.888, respectively. Both classifiers also had a higher number of misclassified pixels than the other two classifiers, with Fuzzy C-means having the highest number of misclassified pixels at 403,100. The reported gray intensity range of the misclassified pixels was similar for all classifiers, ranging from 85 to 112. However, the Naive Bayes show relatively reasonable pore size distribution, and the resulting binarized image was more realistic in comparison to the original image and reference images.

The porosity distribution of the two samples from the productive interval 1966 and 1967 appears heterogeneous, which is common among carbonate rocks. Generally speaking, this heterogeneity can be attributed to the lithologic variation and diagenetic processes. Microscopic examination of thin sections taken from the samples revealed different kinds of pore systems developed either during deposition (as primary porosity) or later on during diagenetic processes (as secondary intra- particle porosity i.e. moldic and vugs). The pores greatly varies in size, from a micrometer to millimeter scale. By comparing micro-XCT tomograms with microscopic images, similar attributes can be found in terms of pore shapes and pore distribution. I also compared the measured pore volume acquired in the laboratory and those obtained from micro-XCT images, where similar values were detected by applying both techniques. After reconstructing 3D digital core samples, a subsample was extracted in the middle part of 2 mm samples (see Figure 25). The porosities

were determined from the stack of micro-XCT slices with a low voxel size at 2 µm and 4 µm. After segmenting the images, the porosity is measured by counting the number of voxels in the void space from the whole images. It is noteworthy that in reservoir characterization, total porosity is used for overall hydrocarbon storage assessment, while effective porosity is used for hydrocarbon production assessment. It is therefore important to gain insights into both types of porosity (Goral et al. 2019). The porosity distribution of the two samples from the dry interval 1979 and 1980 appears heterogeneous. Microscopic examination of the thin sections taken from the same samples exhibits rapid dissolution and cementation. This can be attributed to the diagenesis processes that take place in a marine environment. The microscopic analysis in Figure 14 showed that the fossils and fossil fragments were dissolved and later filled with mosaic calcite. Inter and intra-granular pores can be seen. The majority of inter-granular pores were filled by calcite and the intra-granular pores remained mainly empty.

The analysis of the velocity data revealed interesting patterns and trends in both samples 1966 and 1967. In the 2D plots comparing the Y component velocity against the X component, I observed a fluctuating behavior with multiple small peaks, followed by a prominent peak in the middle (Figures 55 and Figure 60). This indicates regions of varying flow velocities within the samples, with some localized areas exhibiting higher velocity magnitudes. These variations in velocity can be attributed to variations in pore connectivity and fluid pathways within the samples.

Similarly, in the 2D plots comparing the Z component velocity against the X component (Figure 56 and Figure 61), a distinct pattern was observed with initial high values, followed by fluctuations and a peak in the negative direction. This suggests the presence of localized regions of higher and lower flow velocities within the samples. The presence of peaks at both ends of the plots indicates changes in flow behavior towards the boundaries of the samples.

Regarding the potential analysis, the 3D rendering of the reservoir potential (formation factor) provided valuable insights into the distribution of reservoir properties. In both samples, the X direction showed a homogeneous potential distribution with a slightly high formation factor in the lower part. This indicates relatively uniform permeability in the X direction, with some

variations in the lower region. The Y direction exhibited a low range of formation factor, suggesting a relatively homogeneous potential distribution with minor localized variations. The Z direction showed a mid to high formation factor indicating a localized region of reduced flow or lower permeability. The variations in velocity and potential distributions highlight the heterogeneity and complexity of the fluid flow behavior within the samples. The presence of disconnected pores and variations in pore connectivity can significantly influence the flow patterns and magnitudes observed.

Nevertheless, despite the heterogeneity observed in the samples, there are some common attributes in terms of flow behavior. Where, both samples exhibit higher flow velocities in the X and Y directions compared to the Z direction.

In the X direction, the flow velocities are consistently high throughout the samples, indicating a relatively uniform flow behavior in this direction. This suggests that there are relatively well-connected pore networks or pathways that facilitate fluid flow along the X direction.

Similarly, in the Y direction, the flow velocities are also relatively high, with some localized variations. This indicates the presence of connected pathways or regions with higher permeability that enable fluid to flow more easily in the Y direction.

In contrast, the Z direction shows lower flow velocities compared to the X and Y directions. This may indicate the presence of barriers or regions with lower permeability that impede the flow in the Z direction. The observed fluctuations and peaks in the Z component velocity plot may be attributed to localized regions of enhanced or restricted flow within the samples.

10. Scientific results

My research focused on characterizing the origin and types of pores in the Sarmatian limestone, considering the distinct geological environments of the upper and lower intervals in the studied area. My research has successfully described the origin and types of pores present. I have identified various pore types within these intervals and examined the effects of dissolution during diagenesis on their formation and evolution.

1- My investigation has revealed that two diagenetic environments, meteorite phreatic and marine diagenesis have played significant roles in the evolution of the pore system. During phreatic meteorice diagenesis I observed the advancement and development of porosity in the carbonates. This diagenetic environment is characterized by the presence of aggressive fluids in shallow marine environment that rapidly dissolve the deposited carbonate minerals, thereby creating secondary porosity.

In contrast, in a marine environment, cementation is the predominant and most active diagenetic process, exerting a profound influence on porosity modification. In this environment most of the channels and the pore voids were filled with mosaic calcite and calcite mud. My findings indicate the occurrence of three types of cementations within the studied samples: dogtooth cement, blocky cement, and bladed cement. My findings highlight the complex interplay between dissolution and cementation during both meteoric phreatic and marine diagenesis. These diagenetic processes have a profound impact on the pore system within the Sarmatian limestone. Comparison of the productive and dry samples demonstrated well that the diagenetic environment has a profound influence on porosity increase and decease. In our case the limestone in both of the productive and the dry intervals were deposited in marine environment but diagenesis of the productive rocks happened in the meteoritic phreatic, until the diagenesis of the dry rocks started in meteoric vadose environment and finished in marine environment. We can conclude that during diagenesis of the productive part the relative sea level decreased considerably. This is in accordance with the results of Palotás (2014), who, based on sedimentological investigation of Sarmatian carbonates in the Buda Hills, revealed a drop of 5-7 m in sea level during the late Sarmatian. Due to this the water become so shallow that fresh water had a considerable

influence during diagenesis of the upper part of the investigated succession.

By elucidating the specific origins, types, and effects of pore formation, my research contributes to a more comprehensive understanding of reservoir characterization.

2. I developed an image analyzing method to analyze images and characterize the pore space by employing unsupervised machine learning. Where different ML techniques was tested including clustering and entropy techniques for classifying the pore gray scale values of the image pixels. Subsequently, the supervised machine learning method, Naïve Bayes, was employed to enhance the classification process. The Naïve Bayes is a probabilistic algorithm that calculates the likelihood of a data point belonging to a particular class based on the observed features. By considering the probability distribution of gray values, the model can estimate the likelihood of each pore being classified into different categories. K-fold cross-validation is a technique that helps assess the generalization capability of the model. The accuracy of the model was the highest using type-2 fuzzy entropy. In addition, I assess the accuracy of the classification results through two approaches: visual inspection and a comparison of the pore size distribution generated by each method. Furthermore, I compared the results obtained from my methods with a ground truth image, which was created through manual annotation and labeling. This comprehensive evaluation process allows to validate the effectiveness and reliability of my classification techniques in accurately characterizing the pore space.

3. By evaluating the 3D pore network parameters for the examined samples I reached the following results:
- Sample 1966 showed 24% porosity from image analysis and 25% from the He method in the lab. The average pore size was 0.0609 mm, with some as large as 0.132 mm. The average coordination number was 10, indicating high connectivity, reaching 35 in some cases. Pores and pore throats showed a correlation, especially for throat radii smaller than 65 microns. Larger pore throat radii were associated with higher coordination numbers.

Similarly, sample 1967 had 27% porosity from image analysis and 25% from the He method. The average pore size was 0.0535 mm, with some as large as 0.163 mm. The average

coordination number was 5, with a maximum of 45, indicating significant connectivity. Pores and pore throats showed a correlation, particularly for throat radii smaller than 65 microns. Larger pore throat radii were associated with higher coordination numbers, confirming the relationship between pore size, pore throat size, and connectivity.

4. Sample 1979 exhibited an average porosity of 11.9% based on XCT images and 8.28 % measured at the Lab. A 3D analysis of the pore space revealed that isolated pores were the predominant form in the sample. No pore connection was observed, with only individual macro and micro pores were present. The majority of the channels were filled with carbonate cement, as confirmed during the thin section investigation. However, a few random pore connections were detected. The pore radius ranged from 4 μm to 15 μm, with the most common pore size being 9 μm.

Similarly, sample 1980 had an average porosity of 14% as determined from XCT images and 11.4% measured at the Lab. The 3D analysis indicated that isolated pores were the dominant form in this sample as well. Like sample 1979, no pore connection was present, only solitary macro and micro pores appeared. The majority of channels were filled with carbonate cement, which was further confirmed through thin section investigation. A few scattered pore connections were observed randomly. Microscopic analysis revealed similar characteristics to sample 1979, with fossils, fossil fragments, and the matrix being dissolved and subsequently filled with mosaic calcite. The pore radius ranged from 4 μm to 40 μm, and the most prevalent pore size was 13 μm.

5. Comparing the 2D pore volume fraction to the calculated 2D fractal dimension in the samples originated from the upper productive interval (1966 and 1967), an interesting trend was observed. direct relationship appeared between the porosity and the fractal dimension. Additionally, the 2D fractal dimension exhibited high values ranging between 1.65 and 1.67, indicating the presence of irregular pore shapes and rough pore surfaces. The pore structure displayed complex and irregular shapes. However, for the samples originated from the lower dry interval (1979 and 1980), no correlation was found between the pore volume and the fractal dimension. The pores in these samples exhibited irregular and complicated shapes, regardless of their sizes. This irregularity persisted throughout all four studied samples.

6. In order to study the reservoir properties and understand the fluid flow patterns, I have selected a region of interest within the sample for fluid flow simulation experiments. The sample was encapsulated on four faces, creating a controlled experimental setup. To guide the flow along a specific direction, experimental setups were added to two opposite faces of the sample. This setup allows to investigate the flow behavior in three directions: X, Y, and Z. By repeating this process, I analyzed and evaluated the flow patterns and characteristics in each direction.

The laboratory measurements recorded permeability values of 33.1 mD for sample 1966 and 54.32 mD for sample 1967. In contrast, the permeability derived from the images was higher, with values of 190 mD for sample 1966 and 880 mD for sample 1967. This difference in permeability can be attributed to the selection of a highly porous region of interest for numerical simulation, specifically focusing on understanding the fluid flow behavior within the pore space. Furthermore, it is important to acknowledge the presence of inherent uncertainty in the permeability estimation due to various factors, including the limitations of the imaging technique and the methods employed for image processing. These factors can introduce potential errors and biases that may impact the accuracy of the derived permeability values. Therefore, while the derived permeability values from the images may provide valuable insights into the fluid flow behavior within the pore space, it is essential to consider and account for the inherent uncertainties associated with the imaging process and subsequent analysis.

7. In Sample 1966, the flow behavior was analyzed in three directions: X, Y, and Z. In the X direction, disconnected pores and low velocities were observed, indicating potential flow barriers and resistance. The Y direction showed higher velocities and favorable fluid pathways within the pore network. The Z direction had lower velocities and fewer streamlines, suggesting less momentum and lower flow rates compared to the other directions. In Sample 1967, a similar analysis revealed a consistent and relatively high velocity in the X direction, with both favorable and constricted flow regions. The Y direction exhibited high velocities and favorable flow conditions, while the Z direction showed lower velocities and fewer streamlines, indicating reduced momentum and flow rates compared to the X and Y directions.

8. In Sample 1966 and 1967, the flow behavior was analyzed using the average Y and Z component velocities plotted against the X component. The plot showed changes in flow direction and velocity along the X axis. A prominent peak in the center indicated a concentrated

area of higher flow magnitude, while fluctuations between positive and negative directions were observed. Towards the end of the X axis, there were additional peaks suggesting specific flow patterns or structural elements influencing velocity changes. The average Z component velocity initially varied between positive and negative values but eventually stabilized with no significant variation.

9. In both Sample 1966 and Sample 1967, the analysis of flow rate with respect to throat radius reveals a consistent pattern. Initially, as the throat radius increases, the flow rate rises, reaching its peak at specific values - 12.5 to 18 microns in Sample 1966 and 10 to 20 microns in Sample 1967. Beyond these optimal ranges, the flow rate diminishes as the throat radius continues to expand. This behavior is attributed to the interplay between pressure drop and fluid velocity, highlighting the critical role of throat radius in determining flow rate.

The influence of channel length on flow rate follows a similar trend in both samples. As channel length increases, the flow rate initially increases, peaking at specific values - 50 to 100 microns in Sample 1966 and 30 to 60 microns in Sample 1967. However, exceeding these optimal ranges results in a decline in flow rate. The initial increase is primarily driven by reduced flow resistance in longer channels, offering more space for fluid to flow through. The subsequent decline is due to factors like increased frictional losses and the development of laminar flow patterns, which limit the flow rate.

10. The effective formation factor was calculated through the effective formation factor Calculation module in Avizo. The formation factor helps in evaluating the flow behavior and assessing the overall fluid flow potential within the porous medium. The reservoir potential appears to be relatively homogeneous in the X and Y directions in both samples 1966 and 1967, suggesting a rather uniform distribution of the formation factors. This shows that the formation factor is generally consistent in these directions, resulting in less variety in the behavior of fluid flow. On the other hand, an apparent feature in the reservoir potential can be seen while in the z direction. In the midst of the reservoir, there occurs a cutoff or a change in the formation factor. This cutoff denotes a change or break in the connectivity or pore structure in the Z direction.

11. The 3D pore analysis of samples 1979 and 1980 revealed the presence of isolated pores distributed randomly throughout the samples, indicating a lack of connectivity. This

characteristic makes the samples impermeable. Lab measurements confirmed the low permeability of these samples, with recorded values of 0.0721 mD for sample 1979 and 0.0037 mD for sample 1980. These low permeability values can be attributed to the presence of sub-micron pores that are below the resolution of the imaging technique, specifically at the 4-micron range, making them undetectable in the images.

11. Applicability of the results

The results obtained from the analysis of Sarmatian carbonates have several practical implications and applications. Firstly, the findings provide valuable information on the microstructural features and development history of the pore space and the history of the formation of the pores. Furthermore, the analysis of these carbonate samples has implications for the evaluation and prediction of reservoir properties. The examination of pore structures and connectivity can help in predicting the fluid flow behavior and reservoir quality of similar carbonate rocks. This information is crucial for the exploration and production of hydrocarbon resources in carbonate reservoirs.

Additionally, the results of the flow behavior analysis provide insights into the fluid flow patterns within the pore network of the studied samples. Understanding the flow behavior and connectivity of pores is essential for predicting reservoir performance and optimizing production strategies.

Furthermore, the observations of irregular pore shapes, rough pore surfaces, and the lack of pore connectivity in some samples contribute to our understanding of the heterogeneity and complexity of carbonate reservoir systems. This knowledge can help in refining reservoir models and improving reservoir characterization and simulation techniques.

12. References

Adler, P.M., Jacquin, C.G., & Thovert, J.F. (1992). The formation factor of reconstructed porous media. Water Resources Research, 28, 1571-1576. https://doi.org/10.1029/92WR00059

Al-Ansi, N., Gharbi, O., Raeini, A. Q., Yang, J., Iglauer, S., Blunt, M. (2013). Influence of micro-computed tomography image resolution on the predictions of petrophysical properties. In IPTC 2013: International Petroleum Technology Conference (pp. 1291-1298). https://doi.org/10.3997/2214-4609-pdb.350.iptc16600.

Al-Attas, R., & El-Zaart, A. (2006). Thresholding of Medical Images Using Minimum Cross Entropy. Kuala Lumpur International Conference on Biomedical Engineering, Kuala Lumpur, Malaysia, pp. DOI: 10.1007/978-3-540-68017-8_76

Al-Kharusi, A. S., & Blunt, M. J. (2007). Network extraction from sandstone and carbonate pore space images. Journal of Petroleum Science and Engineering, 56, 219-231. https://doi.org/10.1016/j.petrol.2006.09.003

Andrä, H., Combaret, N., Dvorkin, J., Glatt, E., Han, J., Kabel, M., Keehm, Y., Krzikalla, F., Lee, M., Madonna, C., et al. (2013). Digital rock physics benchmarks—Part I: Imaging and segmentation. Computers & Geosciences, 50, 25-32. https://doi.org/10.1016/j.cageo.2012.09.005.

Arns, C. H., Knackstedt, M. A., Pinczewski, M. V., & Lindquist, W. B. (2001). Accurate estimation of transport properties from microtomographic images. Geophysical research letters, 28(17), 3361-3364. https://doi.org/10.1029/2001GL012987

Arns, C. H., Robins, V., Sheppard, A. P., Sok, R. M., Pinczewski, W. V., & Knackstedt, M. A. (2004). Effect of network topology on relative permeability. Transport in Porous Media, 55(1), 21-46. https://doi.org/10.1023/B:TIPM.0000007252.68488.43

Babaguchi, N., Yamada, K., Kise, K., Tezuka, T. (1990). Connectionist model binarization. Proc. 10th ICPR, pp. 51-56.

Badics, B., & Vető, I. (2012). Source rocks and petroleum systems in the Hungarian part of the Pannonian Basin: The potential for shale gas and shale oil plays. Marine and Petroleum Geology, Volume 31, Issue 1, pp. 53-69. https://doi.org/10.1016/j.marpetgeo.2011.08.015

Bakke, S., & Øren, P. E. (1997). 3-D pore-scale modelling of sandstones and flow simulations in the pore networks. SPE Journal, 2, 136-149. https://doi.org/10.2118/35479-PA

Baldwin, C. A., Sederman, A. J., Mantle, M. D., Alexander, P., & Gladden, L. F. (1996). Determination and characterization of the structure of a pore space from 3D volume images. Journal of Colloid and Interface Science, 181(1), 79–92. https://doi.org/10.1006/jcis.1996.0358

Baruchel, J., Buffiere, J.-Y., Cloetens, P., Di Michiel, M., Ferrie, E., Ludwig, W., Maire, E. and Salvo, L., 2006. Advances in synchrotron radiation microtomography. Scripta Materialia, 55: 41-46. https://doi.org/10.1016/j.scriptamat.2006.02.012

Bernsen, J. (1986). Dynamic thresholding of gray-level images. In Proc. Eighth Int'l Conf. Pattern Recognition (pp. 1,251-1,255).

Biswal, B., & Hilfer, R. (1999). Microstructure analysis of reconstructed porous media. Physica A, 266, 307-311. https://doi.org/10.1016/S0378-4371(98)00607-4

Blake, A. (1989). Comparison of the efficiency of deterministic and stochastic algorithms for visual reconstruction. IEEE Transactions on Pattern Analysis and Machine Intelligence, 11, 2-12. DOI: 10.1109/34.23109

Blanz, W. E., Gish, S. L. (1990). A connectionist classifier architecture applied to image segmentation. In Proceedings of the 10th ICPR, pp. 272-277. DOI: 10.1109/ICPR.1990.119369

Bonner, B. P., Roberts, J. J., & Schneberk, D. J. (1994). Determining water content and distribution in reservoir graywacke from the northeast Geysers with X-ray computed tomography (No. UCRL-JC-117542; CONF-941043-4). Lawrence Livermore National Lab.(LLNL), Livermore, CA (United States).

Bouxsein, M. L., Boyd, S. K., Christiansen, B. A., Guldberg, R. E., Jepsen, K. J., & Müller, R. (2010). Guidelines for assessment of bone microstructure in rodents using micro-computed

tomography. Journal of Bone and Mineral Research, 25(7), 1468-1486. doi:10.1002/jbmr.141. https://doi.org/10.1002/jbmr.141

Brink, D. (1992). Thresholding of digital images using two-dimensional entropies. Pattern Recognition, vol. 25 (8), pp. 803–808.

Brunke, O., Neuber, D., Lehmann, D. (2007). NanoCT: visualizing of internal 3D-structures with submicrometer resolution. MRS Online Proceedings Library (OPL) 990. doi:10.1557/PROC-0990-B05-09

Brunke, O., Santillan, J., Suppes, A. (2010). Precise 3D dimensional metrology using high resolution X-ray computed tomography (μCT). In Developments in X-Ray Tomography VII, vol. 7804, pp. 203-215. https://www.ndt.net/?id=9215

Bryant, S. L., Cade, C. A., & Mellor, D. W. (1993). Permeability prediction from geological models. AAPG Bulletin, 77, 1338-1350. https://doi.org/10.1306/BDFF8E84-1718-11D7-8645000102C1865D

Budai, T., & Maros, G. (2018). Geology of Hungary. An Introduction to Geology of Hungary in Kovács Zoltan (Ed.), Hydrocarbons in Hungary, Budapest, pp. 22-32.

Cade, C. A., Evans, I. J., & Bryant, S. L. (1994). Analysis of permeability controls: A new approach. Clay Minerals, 29, 491-501. https://doi.org/10.1180/claymin.1994.029.4.08

Canette, A., & Briandet, R. (2014). Microscopy | Confocal Laser Scanning Microscopy. In Encyclopedia of Food Microbiology (Second Edition) (pp. 676-683). Academic Press. https://doi.org/10.1016/B978-0-12-384730-0.00214-7.

Chang, Y., & Luo, B. (2019). Bidirectional convolutional LSTM neural network for remote sensing image super-resolution. Remote Sensing, 11, 1–18. doi:10.3390/rs11202333.

Chauhan, S., Rühaak, W., Anbergen, H., Kabdenov, A., Freise, M., Wille, T., & Sass, I. (2016). Phase segmentation of X-ray computer tomography rock images using machine learning

techniques: An accuracy and performance study. Solid Earth, 7(4), pp. 1125–1139. doi:10.5194/se-7-1125-2016.

Chauhan, S., Rühaak, W., Khan, F., Enzmann, F., Mielke, P., Kersten, M., & Sass, I. (2016). Processing of rock core microtomography images: Using seven different machine learning algorithms. Computers & Geosciences, 86, 120–128. doi:10.1016/j.cageo.2015.10.013.

Chawla, N., Sidhu, R. S., & Ganesh, V. V. (2006). Three-dimensional visualization and microstructure-based modeling of deformation in particle-reinforced composites. Acta Materialia, 54(6), 1541-1548. https://doi.org/10.1016/j.actamat.2005.11.027

Chen, W., He, X., Liu, M., Mitri, H., & Wang, Q. (2016). Meso-and macro-behaviour of coal rock: observations and constitutive model development. *International Journal of Mining, Reclamation and Environment*, *30*(1), 13-24. 10.1080/17480930.2013.878561

Cnudde, V., 2005. Exploring the potential of X-ray tomography as a new non-destructive research tool in conservation studies of natural building stones. Ghent University. Faculty of Sciences. http://hdl.handle.net/1854/LU-471111

Cnudde, V., Boone, M.N., "High-resolution X-ray computed tomography in geosciences: a review of the current technology and applications", EarthScience Reviews (2013), doi: http://dx.doi.org/10.1016/j.earscirev.2013.04.003

Coehlo, D., Thovert, J. F., & Adler, P. M. (1997). Geometrical and transport properties of random packings of spheres and aspherical particles. Physical Review E, 55, 1959-1978. https://doi.org/10.1103/PhysRevE.55.1959

Coker DA, Torquato S, Dunsmuir JH. Morphology and physical properties of Fontainebleau sandstone via a tomographic analysis. J Geophys Res Solid Earth 1996; 101:17497–506. https://doi.org/10.1029/96JB00811

Coles, M. E., Muegge, E. L., & Sprunt, E. S. (1991). Applications of CAT scanning for oil and gas production research. IEEE Transactions on Nuclear Science, 38(2), 510-515.

Coles, M.E., Hazlett, R.D., Spanne, P., Soll, W.E., Muegge, E.L. and Jones, K.W., 1998. Pore level imaging of fluid transport using synchrotron X-ray microtomography. Journal of Petroleum Science and Engineering, - 19(- 1-2): 55- 63. https://doi.org/10.1016/S0920-4105(97)00035-1

Cornée, J. J., Moissette, P., Saint Martin, J. P., Kazmer, M., Tóth, E., Görog, Á., … & Müller, P. (2009). Marine carbonate systems in the Sarmatian (Middle Miocene) of the Central Paratethys: the Zsámbék Basin of Hungary. Sedimentology, 56, 1728-1750. https://doi.org/10.1111/j.1365-3091.2009.01055.x

Cortina-Januchs, M., Quintanilla-Dominguez, J., Vega-Corona, A., Tarquis, M., & Andina, D. (2011). Detection of pore space in CT soil images using artificial neural networks. Biogeosciences, 8, 279–288. doi:10.5194/bg-8-279-2011.

De Santo, M., Lowe, M., & Williams, G. (2004). Standard uncertainty evaluation in image-based measurements. Measurement, 36(3-4), 347-358. https://doi.org/10.1016/j.measurement.2004.09.011

Dietterich, T. (1998). Approximate statistical tests for comparing supervised classification learning algorithms. Neural Computation, Volume 10, Issue 7, pp. 1895–1923. https://doi.org/10.1162/089976698300017197

Dong, H., Blunt, M. J. (2007). Micro-CT imaging and pore network extraction. Earth Science and Engineering, 217. https://doi.org/10.1103/PhysRevE.80.036307

Dong-Chul, P. (2016). Image Classification Using Naive Bayes Classifier. International Journal of Computer Science and Electronics Engineering (IJCSEE), 4(3), pp. 2320–4028.

dos Anjos, C., Avila, M., Vasconcelos, A., Pereira Neta, A., Medeiros, L., Evsukoff, A., Surmas, R., & Landau, L. (2021). Deep learning for lithological classification of carbonate rock micro-CT images. Computers & Geosciences, 25, 971-983. https://doi.org/10.1007/s10596-021-10033-6

Dullien, F. A. L. (1992). Porous media: Fluid transport and pore structure. Academic Press.

Dunsmuir, J., Ferguson, S., D'Amico, K., & Stokes, J. (1991). X-ray microtomography: A new tool for the characterization of porous media. Proceedings of the 1991 SPE Annual Technical Conference and Exhibition, Dallas. https://doi.org/10.2118/22860-MS

Dunsmuir, J.H., Ferguson, S.R., D'Amico, K.L., & Stokes, J.P. (1991). X-ray microtomography: a new tool for the characterization of porous media. Paper SPE 22860, Proceedings of 66th Annual Technical Conference and Exhibition of the Society of Petroleum Engineers, Dallas, TX. https://doi.org/10.2118/22860-MS

Elliott, J.C., & Dover, S.D. (1982). X-ray micro-tomography. Journal of Microscopy, 126, 211-213. https://doi.org/10.1111/j.1365-2818.1982.tb00376.x

Finney, J. (1968). Random packings and the structure of the liquid state. Ph.D. thesis, University of London, London, England. https://ethos.bl.uk/OrderDetails.do?uin=uk.bl.ethos.481541

Flannery, B.P., Deckman, H.W., Roberge, W.G., & D'Amico, K.L. (1987). Three-Dimensional X-Ray Microtomography. Science, 237(4821), 1439-1444. DOI: 10.1126/science.237.4821.1439

Fu, K. S., Mui, J. K. (1981). A survey on image segmentation. Pattern Recognition, 13, 3-16. https://doi.org/10.1016/0031-3203(81)90028-5

Fukushima, K. (1980). A self-organizing neural network model for a mechanism of pattern recognition unaffected by shift in position. Biological Cybernetics, 36, 193–202. doi:10.1007/BF00344251.

Geman, S., Geman, D. (1984). Stochastic relaxation, Gibbs distributions and the Bayesian restoration of images. IEEE Transactions on Pattern Analysis and Machine Intelligence, 6, 721-741. DOI: 10.1109/TPAMI.1984.4767596

Gong, L., Nie, L., Xu, Y. (2020). Geometrical and topological analysis of pore space in sandstones based on x-ray computed tomography. Energies, 13(15). https://doi.org/10.3390/en13153774

Gonzalez, C., & Woods, E. (2008). CV book. In Digital Image Processing (3rd ed.).

Goral, J., Walton, I., Andrew, M., & Deo, M. (2019). Pore system characterization of organic-rich shales using nanoscale-resolution 3D imaging. Fuel, 258, 116049. https://doi.org/10.1016/j.fuel.2019.116049

Haas, J., Budai, T., Csontos, L., Fodor, L., & Konrád, Gy. (2010). Pre-Cenozoic geological map of Hungary, 1:500 000. Geological Institute of Hungary, Budapest.

Haralick, R. M., Shapiro, L. G. (1985). Survey, image segmentation techniques. Computer Vision, Graphics, and Image Processing, 29, 100-132. https://doi.org/10.1016/S0734-189X(85)90153-7

Haralick, R., & Shanmugam, K., & Dinstein, I. (1992). Computer and Robot Vision, Volume I. Addison-Wesley.

Hazlett, R. (1995). Simulation of Capillary-Dominated Displacements in Microtomographic Images of Reservoir Rocks. Transport in Porous Media, 20(1-2), 21-35. https://doi.org/10.1007/BF00616924

Hazlett, R.D. (1995). Simulation of capillary-dominated displacements in microtomographic images of reservoir rocks. Transport in Porous Media, 20, 21-35.

Held, K., Kops, E. R., Krause, B. J., Wells, W. M., Kikinis, R., & Muller-Gartner, H. W. (1997). Markov random field segmentation of brain MR images. IEEE Transactions on Medical Imaging, 16(6), 878–886. DOI: 10.1109/42.650883

Hidajat, I., Rastogi, A., Singh, M., & Mohanty, K. K. (2002). Transport properties of porous media reconstructed from thin-sections. SPE Journal, 7, 40-48. https://doi.org/10.2118/77270-PA

Horváth, F. (1993). Towards a mechanical model for the formation of the Pannonian Basin. Tectonophysics, Volume 226, Issues 1–4, pp. 333-357. https://doi.org/10.1016/0040-1951(93)90126-5.

Iassonov, P., Gebrenegus, T., & Tuller, M. (2009). Segmentation of X-ray computed tomography images of porous materials: A crucial step for characterization and quantitative analysis of pore structures. Water Resources Research, 45, 1-12. doi:10.1029/2009WR008087.

Jain, A. (2010). Data clustering: 50 years beyond K-means. Pattern Recognition Letters, Volume 31, Issue 8, pp. 651–666. https://doi.org/10.1016/j.patrec.2009.09.011

Jámbor, Á. (1977). A Mányi-medence neogén képződményei felépítésének vázlata — Földt. Kut. XX/4., 25–27.

Jang, M., & Park, D. (2016). Stochastic Classifier Integration Model. International Journal of Applied Engineering Research, Vol. 11, No. 2, pp. 809-814.

Jerauld, G.R. and S.J. Salter, Effect of pore-structure on hysteresis in relative permeability and capillary pressure: Pore-level modeling. Transport in Porous Media, 1990. 5: p. 103-151. https://doi.org/10.1007/BF00144600

Kainourgiakis, M. E., Kikkinides, E. S., Steriotis, T. A., Stubos, A. K., Tzevelekos, K. P., & Kanellopoulos, N. K. (2000). Structural and transport properties of alumina porous membranes from process-based and statistical reconstruction techniques. Journal of Colloid and Interface Science, 231, 158-167. https://doi.org/10.1006/jcis.2000.7115

Kak, A.C. and Slaney, M., 2001. Principles of computerized tomographic imaging. SIAM, New York. https://doi.org/10.1137/1.9780898719277

Kang, W.-X., Yang, Q.-Q., Liang, R.-P. (2009). The comparative research on image segmentation algorithms. In Proceedings of the 1st International Workshop on Education Technology and Computer Science, IEEE, pp. 703-707. DOI: 10.1109/ETCS.2009.417

Kato, Z., Zerubia, J., Berthod, M. (1996). A hierarchical Markov random field model and multitemperature annealing for parallel classification. Graphical Models and Image Processing, 58(1), 18-37.

Kaur, D., Kaur, Y. (2014). Various image segmentation techniques: A review. International Journal of Computer Science and Mobile Computing, vol. 3, no. 5, 2014, pp. 809-814.

Keller, M., Schuetz, P., Erni, R., Rossell, M., Lucas, F., Gasser, P., & Holzer, L. (2013). Characterization of multi-scale microstructural features in Opalinus Clay. Microporous and Mesoporous Materials, 170, 83-94. https://doi.org/10.1016/j.micromeso.2012.11.029

Ketcham, R. a. & Carlson, W.D., 2001. Acquisition, optimization and interpretation of X-ray computed tomographic imagery: applications to the geosciences. Computers & Geosciences, 27(4), pp.381–400. Available at: http://linkinghub.elsevier.com/retrieve/pii/S0098300400001163.

Khan, F., Enzmann, F., & Kersten, M. (2016). Multi-phase classification by a least-squares support vector machine approach in tomography images of geological samples. Solid Earth, 7, 481–492. doi:10.5194/se-7-481-2016.

Khokher, M. R., Ghafoor, A., Siddiqui, A. M. (2012). Image segmentation using multilevel graph cuts and graph development using fuzzy rule-based system. IET Image Processing.

Kirti, R., Bhatnagar, A. (2017). Image segmentation using Canny edge detection technique. International Journal of Techno-Management Research, vol. 04, no. 04, 2017, pp. 8-14.

Klinkenberg, L. J. (1941). The Permeability of Porous Media to Liquids and Gases: Drilling and Production Practices. American Petroleum Institute.

Kohavi, A. (1995). A study of cross-validation and bootstrap for accuracy estimation and model selection. The International Joint Conference on Artificial Intelligence (IJCAI), pp. 1137–1145.

Kókay, J. (1989). A mány–zsámbéki terület bádeni és szarmata képződményei — Kézirat, 25p.

Koplik, J., Lin, C., & Vermette, M. (1984). Conductivity and permeability from microgeometry. Journal of Applied Physics, 56, 3127-3131. https://doi.org/10.1063/1.333872

Larson, C. (1931). The shrinkage of the coefficient of multiple correlation. Journal of Educational Psychology, Vol. 22, pp. 45–55. doi:10.1037/h0072400.

LeCun, Y., Bengio, Y., & Hinton, G. (2015). Deep learning. Nature, 521, 436–444. doi:10.1038/nature14539.

Lei, T., Jia, X., Zhang, Y., He, L., Meng, H., & Nandi, K. (2018). Significantly Fast and Robust Fuzzy C-Means Clustering Algorithm Based on Morphological Reconstruction and Membership Filtering. IEEE Transactions on Fuzzy Systems, 26(5), pp. 3027–3041. doi:10.1109/TFUZZ.2018.2796074. DOI: 10.1109/TFUZZ.2018.2796074

Leu, L., Berg, S., Enzmann, F., Armstrong, R. T., Kersten, M. (2014). Fast X-ray micro-tomography of multiphase flow in Berea sandstone: A sensitivity study on image processing. Transport in Porous Media, 105(2), 451-469. https://doi.org/10.1007/s11242-014-0378-4.

Levitz, P. (1998). Off-lattice reconstruction of porous media: critical evaluation, geometrical confinement, and molecular transport. Advances in Colloid and Interface Science, 77, 71-106. https://doi.org/10.1016/S0001-8686(98)00042-6

Lindquist, W., & Venkatarangan, A. (1999). Investigating 3D geometry of porous media from high-resolution images. Physics and Chemistry of the Earth, Part A: Solid Earth and Geodesy, 24(7), 593–599. https://doi.org/10.1016/S1464-1895(99)00085-X

Lindquist, W.B., Lee, S.-M., Coker, D.A., Jones, K.W., Spanne, P. (1996). Medial axis analysis of void structure in three-dimensional tomographic images of porous media. Journal of Geophysical Research: Solid Earth, 101(B4), 8297–8310. https://doi.org/10.1029/95JB03039

Lymberopoulos, D. P., Payatakes, A. (1992). Derivation of topological, geometrical, and correlational properties of porous media from pore-chart analysis of serial section data. Journal of Colloid and Interface Science, 150(1), 61-80. https://doi.org/10.1016/0021-9797(92)90268-Q.

Mahmoudi, L., & El Zaart, A. (2012). A survey of entropy image thresholding techniques. 2012 2nd International Conference on Advances in Computational Tools for Engineering Applications, ACTEA, pp. 204–209. doi:10.1109/ICTEA.2012.6462867.

Mouze, D. (1996). X-ray microradiography. Handbook of microscopy I, 130-147.

Niblack, W. (1985). An introduction to digital image processing. Strandberg Publishing Company.

Orsi, T. H., Edwards, C. M., & Anderson, A. L. (1994). X-ray computed tomography: A nondestructive method for quantitative analysis of sediment cores. Journal of Sedimentary Research Section A: Sedimentary Petrology and Processes, 64(3), 690-693.

Øren, P. E., & Bakke, S. (2002). Process-based reconstruction of sandstones and prediction of transport properties. Transport in Porous Media, 46, 311-343. https://doi.org/10.1023/A:1015031122338

Otsu, N. (1979). A threshold selection method from gray-level histograms. IEEE Transactions on Systems, Man, and Cybernetics, 9, 62-66. DOI: 10.1109/TSMC.1979.4310076

Pal, N. R., & Pal, S. K. (1993). A review on image segmentation techniques. Pattern Recognition, 26, 1277–1294. doi:10.1016/0031-3203(93)90135-J.

Palotás K. 2014: A szarmata üledékképződés vizsgálata a Budai-hegységben és környékén. (Sedimentary investigation of the Sarmatian deposits around the Buda Hills). PhD Thesis, University of Pécs.

Pham, C., Tor-Díez, C., Meunier, H., Bednarek, N., Fablet, R., Passat, N., & Rousseau, F. (2019). Multiscale brain MRI super-resolution using deep 3D convolutional networks. Computerized Medical Imaging and Graphics, 77, 1–15. doi:10.1016/j.compmedimag.2019.101647.

Pilotti, M. (2000). Reconstruction of clastic porous media. Transport in Porous Media, 41, 359-364. https://doi.org/10.1023/A:1006696301805

Pyrak-Nolte, L. J., Montemagno, C. D., & Nolte, D. D. (1997). Volumetric imaging of aperture distributions in connected fracture networks. Geophysical Research Letters, 24(18), 2343-2346.

Pudney, C. (1996). Distance-based skeletonization of 3D images. Proceedings of Digital Processing Applications (TENCON'96), vol. 1, pp. 209–214.

Pudney, C. (1998). Distance-ordered homotopic thinning: a skeletonization algorithm for 3D digital images. Computer Vision and Image Understanding, 72(3), 404–413.

Pun, T. (1980). A new method for gray-level picture thresholding using the entropy of the histogram. Signal Processing, 2, 223-237. https://doi.org/10.1016/0165-1684(80)90020-1

Purcell, C., Harbert, W., Soong, Y., McLendon, T.R., Haljasmaa, I.V., McIntyre, D. and JiKich, J., 2009. Velocity measurements in reservoir rock samples from the SACROC unit using various pore fluids, and integration into a seismic survey taken before and after a CO2 sequestration flood. In: J. Gale, H. Herzog and J. Braitsch (Editors), Greenhouse Gas Control Technologies 9. Energy Procedia. Elsevier Science Bv, Amsterdam, pp. 2323-2331. https://doi.org/10.1016/j.egypro.2009.01.302

Quiblier, J.A. (1984). A new three-dimensional modeling technique for studying porous media. Journal of Colloid and Interface Science, 98, 84-102. https://doi.org/10.1016/0021-9797(84)90481-8

Reynolds, O. (1883). XXIX. An experimental investigation of the circumstances which determine whether the motion of water shall be direct or sinuous, and of the law of resistance in parallel channels. Philosophical Transactions of the Royal Society of London, (174), 935-982.

Rezaei, F., Izadi, H., Memarian, H., Baniassadi, M. (2019). The effectiveness of different thresholding techniques in segmenting micro CT images of porous carbonates to estimate porosity. Journal of Petroleum Science and Engineering, 177, 518-527. https://doi.org/10.1016/j.petrol.2018.12.063

Roberts, A. P., & Torquato, S. (1999). Chord-distribution functions of three-dimensional random media: approximate first-passage times of Gaussian processes. Physical Review E, 59, 4953-4963. https://doi.org/10.1103/PhysRevE.59.4953

Roberts, A.P. (1997). Statistical reconstruction of three-dimensional porous media from two-dimensional images. Physical Review E, 56, 3203-3212. https://doi.org/10.1103/PhysRevE.56.3203

Rögl, F., & Steininger, F. (1984). Neogene Paratethys, Mediterranean and Indo-pacific seaways. Geological journal. Special issue, 171-200.

Scholle, P. A., & Ulmer-Scholle, D. A. (2003). A Color Guide to the Petrography of Carbonate Rocks: Grains, Textures, Porosity, Diagenesis. AAPG Memoir 77. Tulsa, Oklahoma.

Schwartz, L. M., Auzerais, F., Dunsmuir, J., Martys, N., Bentz, D. P., & Torquato, S. (1994). Transport and diffusion in three-dimensional composite media. Physica A, 207, 28-36. https://doi.org/10.1016/0378-4371(94)90351-4

Sengur, A., Turkoglu, I., & Ince, M. (2006). A Comparative Study On Entropic Thresholding Methods. Journal of Electrical & Electronics Engineering, Volume 6, No. 2, pp. 183-188.

Sezgin, M., & Sankur, B. (2004). Survey over image thresholding techniques and quantitative performance evaluation. Journal of Electronic Imaging, 13, 146–165. doi:10.1117/1.1631315.

Sharon, E., Brandt, A., Basri, R. (2000). Fast multiscale image segmentation. Proc. IEEE Conference on Computer Vision, vol. 1, pp. 70–77.

Sheppard, A.P., Sok, R.M., & Averdunk, H. (2005). Improved pore network extraction methods. Proceedings of the International Symposium of the Society of Core Analysts, Toronto, Canada.

Silin, D., & Patzek, T. (2006). Pore space morphology analysis using maximal inscribed spheres. Physica A, 371, 336-360. https://doi.org/10.1016/j.physa.2006.04.048

Silin, D.B., Jin, G., & Patzek, T.W. (2003). Robust determination of pore space morphology in sedimentary rocks. Journal of Petroleum Technology, 56, 69-70. https://doi.org/10.2118/84296-MS

Skowron, A., Orlowska, E., Słowiński, R., Mi, V., Polkowski, L., & Ziarko, W. (2007). Transactions on Rough Sets. 2nd edition. Germany: Springer.

Spowart, J. E., Mullens, H. E., & Puchala, B. T. (2003). Collecting and analyzing microstructures in three dimensions: A fully automated approach. JOM, 55, 35-37. https://doi.org/10.1007/s11837-003-0173-0

Sultana, F., Sufian, A., & Dutta, P. (2020). Evolution of image segmentation using deep convolutional neural network: A survey. Knowledge-Based Systems, 106062. https://doi.org/10.1016/j.knosys.2020.106062

Sztanó, O., Szafián, P., Magyar, I., Horányi, A., Bada, G., Hughes, D. W., ... & Wallis, R. J. (2013). Aggradation and progradation controlled clinothems and deep-water sand delivery model in the Neogene Lake Pannon, Makó Trough, Pannonian Basin, SE Hungary. Global and Planetary Change, 103, 149-167. https://doi.org/10.1016/j.gloplacha.2012.05.026

Talukdar, M. S., Torsaeter, O., & Ioannidis, M. A. (2002). Stochastic reconstruction of particulate media from two-dimensional images. Journal of Colloid and Interface Science, 248, 419-428. https://doi.org/10.1006/jcis.2001.8064

Tomutsa, L., & Radmilovic, V. (2003). Focused ion beam-assisted three-dimensional rock imaging at submicron scale. Proceedings of the International Symposium of the Society of Core Analysts, Pau, France.

Tomutsa, L., & Silin, D. (2004). Nanoscale pore imaging and pore scale fluid flow modeling in chalk. Lawrence Berkeley National Laboratory: Paper LBNL-56266. Retrieved from http://repositories.cdlib.org/lbnl/LBNL-56266

Tomutsa, L., Silin, D., & Radmilovic, V. (2007). Analysis of chalk petrophysical properties by means of submicron-scale pore imaging and modeling. SPE Reservoir Evaluation & Engineering, 10, 285-293. https://doi.org/10.2118/99558-PA

Toz, G., Yücedağ, İ., & Erdoğmuş, P. (2019). A fuzzy image clustering method based on an improved backtracking search optimization algorithm with an inertia weight parameter. Journal of King Saud University - Computer and Information Sciences, Vol. 31(3), pp. 295-303. https://doi.org/10.1016/j.jksuci.2018.02.011

Vinegar, H. J., & Wellington, S. L. (1987). Tomographic imaging of three-phase flow experiments. Review of Scientific Instruments, 58(1), 96-107. https://doi.org/10.1063/1.1139522

Wei, Y., Liang, X., Chen, Y., Jie, Z., Xiao, Y., Zhao, Y., & Yan, S. (2016). Learning to segment with image-level annotations. Pattern Recognition, 59, 234-244. https://doi.org/10.1016/j.patcog.2016.01.015

Wellington, S.L., Vinegar, H.J. 1987. X-ray computerized tomography. Journal of Petroleum Technology, 39 (8), 885–898. https://doi.org/10.2118/16983-PA

Wennberg, O. P., Rennan, L., & Basquet, R. (2009). Computed tomography scan imaging of natural open fractures in a porous rock: Geometry and fluid flow. Geophysical Prospecting, 57(2), 239-249. https://doi.org/10.1111/j.1365-2478.2009.00784.x

Wildenschild, D., Sheppard, A. (2013). X-ray imaging and analysis techniques for quantifying pore-scale structure and processes in subsurface porous medium systems. Advances in Water Resources, 51, 217-246. https://doi.org/10.1016/j.advwatres.2012.07.018

Xiong, Q., Baychev, T. G., & Jivkov, A. P. (2016). Review of pore network modelling of porous media: Experimental characterizations, network constructions, and applications to reactive transport. Journal of Contaminant Hydrology, 192, 101–117. doi:10.1016/j.jconhyd.2016.07.002.

You, C., Li, G., Zhang, Y., Zhang, X., Shan, H., Li, M., Ju, S., Zhao, Z., Zhang, Z., Cong, W., et al. (2019). CT Super-resolution GAN Constrained by the Identical, Residual, and Cycle Learning Ensemble (GAN-CIRCLE). IEEE Transactions on Medical Imaging, 39, 188–203. doi:10.1109/TMI.2019.2922960.

Youssef, S., Rosenberg, E., Gland, N., Bekri, S., Vizika, O. (2007). Quantitative 3D characterization of the pore space of real rocks: improved μ-CT resolution and pore extraction methodology. International Symposium of the Society of Core Analysts.

Zack, G., Rogers, W., & Latt, S. (1977). Automatic measurement of sister chromatid exchange frequency. Journal of Histochemistry and Cytochemistry, 25, 741–753. doi:10.1177/25.7.70454.

Zadeh, A. (1965). Fuzzy sets. Information and Control, Volume 8, Issue 3, pp. 338-353. https://doi.org/10.1016/S0019-9958(65)90241-X

Zerubia, J., Chellappa, R. (1993). Mean field approximation using Compound Gauss-Markov Random Field for edge detection and image estimation. IEEE Transactions on Neural Networks, 8, 703-709. DOI: 10.1109/72.238324

Zhang, H., Abderrahmane, H., Al Kobaisi, M., & Sassi, M. (2021). Pore-scale characterization and PNM simulations of multiphase flow in carbonate rocks. Energies, 14(21), 6897. https://doi.org/10.3390/en14216897

Zhang, S., Klimentidis, R. E., & Barthelemy, P. (2012). Micron to millimeter upscaling of shale rock properties based on 3D imaging and modeling. In Society of Core Analysis 2012 Symposium, Aberdeen, Scotland, UK, August 27-30.

Zhang, S., Klimentidis, R. E., & Barthelemy, P. (2011). Porosity and permeability analysis on nanoscale FIB-SEM tomography of shale rock. In Society of Core Analysis 2011 Symposium, Paper A080, Austin, Texas, September 18th-21st

13. List of related publications

1- Hasan Al Atrash and Felicitász Velledits (2020) CT based analyses of pore network of reservoir rocks. Geosciences and Engineering, Vol. 8., No 13 pp. 167-184.

2- Hasan Al Atrash, Felicitasz Velledits; Pore-network extraction from micro-computed tomography images. Educational material, Miskolc University website: https://geology.uni- miskolc.hu/files/14596/Hasan_Alatrash_Study_material_of_micro_CT_application.pdf

3- Hasan Al Atrash, Felicitász Velledits (2022) Phase segmentation optimization of micro x-ray computed tomography reservoir rock images using machine learning. Geosciences and Engineering, Vol. 10, No. 15 pp. 63 79. https://doi.org/10.33030/geosciences.2022.15.063Geosciences and Engineering.

4- Hasan Al Atrash, Felicitász Velledits (accepted in press) Comparing Petrophysical Properties and Pore Network Characteristics of Carbonate Reservoir Rocks Using Micro X-ray Tomography Imaging and Microfacies Analyses. GEM - International Journal on Geomathematics.

5- Hasan Al Atrash, Felicitász Velledits (2022) Image segmentation and optimization of X-ray computed tomography images of porous materials;quantitative 3D characterization of the pore space. Abstract. 22. International Congress on Geomathematics in Earth- and Environmental Sciences. Pécs, Hungary 2022.05.19. - 2022.05.21. 33025660. p 69.

6- Hasan Al Atrash, Felicitász Velledits (2021) Image segmentation of X-ray computed tomography data of porous material: a review of global and locally adaptive algorithm. PhD Student Fórum University of Miskolc. 2021. november 18. (Conference presentation)

7- Hasan Al Atrash, Felicitász Velledits (2022) Image segmentation and optimization of X-ray computed tomography images of porous materials;quantitative 3D characterization of the pore space. 22. International Congress on Geomathematics in Earth- and Environmental Sciences.Pécs, Hungary 2022.05.19. - 2022.05.21. (Conference presentation)

8- Hasan Al Atrash, Felicitász Velledits (2023) Pore network characterization and permeability estimation: application of XCT in pore network analysis and flow analysis in porous medium. Abstract. Meeting of young geoscientists Nagyborzsöny Hungary, 2023.31.03 – 2023.01.04. Pp55-56